Université de Montréal

# Dosimetric and fluence measurements at hadron facilities for LHC radiation damage studies

par

Elena León Florián

Département de physique

Faculté des arts et des sciences

Thèse présentée à la Faculté des études supérieures
en vue de l'obtention du grade de
Philosophiæ Doctor (Ph.D.)
en physique

Août, 2000

Université de Montréal
Faculté des études supérieures

Cette thèse intitulée:

# Dosimetric and fluence measurements at hadron facilities for LHC radiation damage studies

présentée par:

Elena Leòn Florián

a été évaluée par un jury composé des personnes suivantes:

| | |
|---|---|
| Prof. Viktor Zacek, | président-rapporteur |
| Prof. Claude Leroy, | directeur de recherche |
| Prof. Louis Lessard, | membre du jury |
| Prof. Doug Stairs, | examinateur externe |

Thèse acceptée le: ......................................

## Abstract

Dosimetry plays an essential role in experiments assessing radiation damage and hardness for the components of detectors to be operated at the future Large Hadron Collider (LHC), CERN (European Laboratory for Particle Physics), Geneva, Switzerland. Dosimetry is used both for calibration of the radiation fields and estimate of fluences and doses during the irradiation tests. The LHC environment will result in a complex radiation field composed of hadrons (mainly neutrons, pions and protons) and photons, each having an energy spectrum ranging from a few keV to several hundreds of MeV or several GeV, even. In this thesis, are exposed the results of measurements of particle fluences and doses at different hadron irradiation facilities: SARA, $\pi$E1-PSI and ZT7-PS used for testing the radiation hardness of materials and equipment to be used in the future experiments at LHC. These measurements are applied to the evaluation of radiation damage inflicted to various semiconductors (such as silicon) and electronics to be installed in the inner detector and calorimeters of the ATLAS detector. These measurements are also applied to the study of the liquid argon purity to be used as active medium in several ATLAS calorimeters.

## Key words

LHC, ATLAS, hadrons, dosimetry, radiation damage

## Sommaire

La dosimétrie joue un rôle essentiel dans les expériences qui évaluent les dommages par radiation et la résistance à ces dommages pour les composants des détecteurs qui seront en opération au futur grand collisionneur hadronique (LHC) devant être construit au CERN (Laboratoire Européen pour la Physique des Particules), Genève, Suisse. La dosimétrie est utilisée tant pour la calibration des champs d'irradiation que pour l'estimation des fluences et doses pendant les tests d'irradiation. L'environnement du LHC produira des champs complexes de radiation composés de hadrons (principalement des neutrons, des pions et des protons) et de photons, chacune des composantes ayant un spectre d'énergie allant de quelques keV jusqu'à plusieurs centaines de MeV et même plusieurs GeV. Cette thèse expose les résultats des mesures de fluences de particules et de doses obtenus à diverses installations d'irradiation par hadrons: SARA, $\pi$E1-PSI and ZT7-PS. Ces résultats sont utilisés pour l'évaluation de la résistance aux radiations de semiconducteurs (tel que le silicium) et de l'électronique devant être installés dans le détecteur interne et dans les calorimétres du détecteur ATLAS. Ces résultats sont aussi utilisés pour létude de la pureté de l'argon liquide qui sera utilisé comme milieu actif de plusieurs calorimètres ATLAS.

## Mots–clefs

LHC, ATLAS, hadrons, dosimétrie, dommages par radiation

# Personal Contributions

In the articles co-authored by the author of the present work, and shown in the appendices, her contribution has been instrumental in several places, and these contributions are now explained.

At SARA neutron facility, the design and construction of the set-up used to measure the absorbed dose distribution using alanine dosimeters has been done by the author. The author performed the measurements of the alanine dosimeters using the ESR technique, and calculated the angular distribution of the total absorbed doses. The results from these measurements are published in [30] (appendix C). These results were also published in various conferences [46, 47].
In addition, the author participated to the data taking of the TOF measurements of the neutron spectrum. The author also ran several iterations of the FLUKA Monte–Carlo program to evaluate the neutron energy spectrum inside the liquid argon cryostat. While some of the most significant results from this simulation are found in [30], the details of the simulation are presented in this thesis. In this framework, the author has contributed to the installation of the FLUKA program on the Montreal VAX cluster.

Results obtained at SARA are published in [48] (appendix D). They mainly report the neutron and photon components of the mixed field. To separate the components of the radiation field, the author used a combination of TLD dosimeters fitted inside a polyethylene sphere as a way to obtain a more accurate reading of the radiation field components. The author performed the fundamental TL dosimeter calibrations at the CERN–radioprotection facilities using gamma ($^{60}$Co) and neutron (Pu-Be) radioactive sources, and carried out the thermal annealing processes before and after each irradiation (neutron/gamma calibrations and SARA experiment). The thermoluminescent reading for both calibration and experiment runs, for both TLD-600 and TLD-700 were performed by the author.

At the PSI facility, the author has participated in the radiation hardness data taking runs. The activity measurements of aluminium, carbon, and indium foils were shared between the author and one of our colleagues. The author did all the dosimetric measurements with alanine and TL dosimeters, including TL calibration, and both TL and ESR readout for the experiment runs. The author crafted the graphics and participated actively in the writing of the article reporting the results [31] (appendix E).

At the same pion facility, the author designed and constructed the set–up used to measure the photon and hadron contamination around the pion beam. The author prepared all the activation foils and dosimeters to be mounted in the set–up. The author performed the numerical processing of all the results coming from the activation and dosimetric measurements. These results are published in [60] (appendix F), and in [61].

At the PS facility, as it was the case at PSI, the author took part in the radiation hardness data taking runs, designed and built the set–up used to measure the hadron contamination around the proton beam, and prepared and measured the activation foils and dosimeters used. The results of this study of the proton beam contamination can be found in [60] (appendix F).

While taking part in the data taking runs at PSI and PS, the author recorded, with one second precision, the relevant irradiation parameters: beam up time, beam down time, time interval between end of irradiation and beginning of readout. The accurate knowledge of those times was necessary to determine the saturation activities for the activation foils at PSI and PS facilities.

Among the key parameters of the irradiation set–ups at SARA, PSI and PS facilities were: the radial distance where to install the activation foils and/or dosimeters, the choice of the activation foil material and thickness, the geometry of the set–ups. Regarding the overall design of the irradiation set–ups used to perform the measurement out–of–beam at PSI and PS facilities, the author has insured the complete absence of materials capable of activation and production of short-lived radioisotopes. The presence of such materials, even as contaminants, could invalidate the measurements, or worse, could pose a health hazard.

The author has contributed to the group's understanding of the software tools for radiation field characterization, both on the simulation (FLUKA) and experimental data retrieval (INTERGAMMA) sides.

The author acted as contact person with the Technical Inspection Safety (TIS) Division at CERN and arranged for the users including the author the availability of powerful calibration sources, accredited radiation metrology, high level dosimeters, and professional experience.

# Contents

# List of Tables

# List of Figures

# List of abbreviations

**ATLAS** A Toroidal Lhc ApparatuS

**Al** Aluminium

**A** Atomic mass

**Z** Atomic number

$N_a$ Avogadro's number

**C** Carbon

**Cs** Cesium

**CPE** Charged–particle equilibrium

**Co** Cobalt

**CMS** Compact Muon Solenoid

**CF** Conversion factor fluence-to-dose

$DK(E)$ Displacement damage cross–section or displacement kerma factor

**ESR** Electron Spin Resonance

**CERN** European Laboratory for Particle Physics

**FCAL** Forward calorimeter

**GaAs** Gallium Arsenide

**Ge** Germanium

**HEC** Hadronic end–cap.

**In** Indium

**PKA** Knock–on atom

**LEP** Large Electron–Positron

**LHC** Large Hadron Collider

**liq. argon** Liquid argon

**Mn** Manganese

**MOS** Metal Oxide Semiconductor

**mip** Minimum ionizing particle

$\mathbf{E}_n$ Neutron energy

**Ni** Nickel

**NIEL** Non-Ionizing Energy Loss

**PSI** Paul Scherrer Institute

$\mathbf{E}_\gamma$ Photon energy

$\pi\mathbf{E1}$ Pion beam at PSI

**Pu-Be** Plutonium-Beryllium

**PAD** Polymer-alanine dosimeter

**ZT7** Proton beam at PS

**PS** Proton Synchrotron

**Si** Silicon.

**Na** Sodium

**SARA** Systéme Accélérateur Rhône–Alpes

**TIS** Technical Inspection Safety

**TLD** Thermoluminescent dosimeters

**TOF** Time-of-flight

**TLD-600** TL dosimeter from the LiF family, isotopic composition $^6$Li

**TLD-700** TL dosimeter from the LiF family, isotopic composition $^7$Li

**V** Vanadium

# Acknowledgements

I wish to first express a very profound gratitude to Pr. Claude Leroy. He has given me the opportunity to pursue Ph.D. thesis work, recognizing the value of my professional experience as applicable to LHC detector development. His guidance and collaboration, during the experiments and through the thesis redaction, have been most effective.

A special acknowledgement must be given to CERN TIS-Division for lending the dosimeters and activation foils used in the present work, as well as giving me access to their laboratories to do the measurements after my experiments. Access was granted any time whenever it was necessary, during the day or during the night!. Many hours of my night shifts were spent at their $\gamma$-spectrometry lab.

I would like to express my gratitude to Dr H. Schönbacher, the CFM-group leader at that time, for giving me the opportunity to work at his group, and to make the first dosimetric measurements at the PSAIF facility. Special thanks also go to M. Tavlet, F. Connickx and J-J. Farey (High Level Dosimetry Laboratory) for their warm welcome to the group where I had worked my first years at CERN. I have enjoyed many fruitful discussions

with M. Tavlet and F. Connickx, they shared with me their experience in dosimetry.
I am grateful to G. Roubaud, he was always very kind and ready to help, with his broad experience in gamma spectrometry and thermoluminescence.
I offer many thanks to J. Tuyn, with whom I had interesting discussions, and because he let me free access to his private library.
I am grateful to R. Raffnsoe who was at the Calibration laboratory, we have been working together during the TLD calibrations (to be used at PSAIF), with X-rays and various $\gamma$ sources. Thanks go also to J. Bourges from the same laboratory, who helped me performing TLD calibrations with $\gamma$ and neutron sources.

I would like to express my gratitude to A. Fassò, who gave me good advice when I was working with FLUKA. I wish to thank G.R. Stevenson too, he answered many of my questions about nuclear activation when I just started to work on this topic.

Outside CERN laboratories, many thanks to J. Collot, from the Institut des Sciences Nucléaires of Grenoble, with whom I have been working during the dosimetric measurements at SARA. Thanks also to P. de Saintignon and his colleagues, I enjoyed very much working with them at Grenoble.
I would like to thank K. Gabathuler and his colleagues from the PSI (Villigen), for their support during our irradiations at the $\pi$E1 beam.

In the last years of my experimental work, I worked with F. Lemeilleur and his collaborators. I am indebted to him for letting me participate in their experiments at the PSI and at the PS. I am grateful to C. Furetta, with whom I shared many hours of interesting discussions. Thanks also to M. Glaser and S. Bates from the same group.

I would like to thank my Latin-American friends: F. Rivera, J.C. Pinto, J. Galvez, Y. Zamora, E. Cerron and J. Lamas; with them I enjoyed many "cafes" talking about our own jobs and everything else.

Finally, I would like to give many thanks to my family, especially to my mother for her infinite love and encouragement during these years and as ever, gracias mamá!. I can not finish these lines without saying: Merci François et Brigitte pour votre amour et compréhension.

*A mi adorada madre Olinda*

*et*

*à ma petite fille Brigitte.*

# Chapter 1

# Introduction

The future Large Hadron Collider (LHC) [1] is under construction at CERN (European Laboratory for Particle Physics), Geneva, Switzerland. This collider will be installed in the same tunnel (27-km circumference) as the existing LEP (Large Electron–Positron) machine. Every 25 ns, the LHC will bring proton bunches into head–on collisions at a centre–of–mass energy of $\sqrt{s}$=14 TeV, with a peak luminosity of $1.0 \times 10^{34}$ cm $^{-2}$ s$^{-1}$. With a proton–proton collision inelastic cross-section of 100 mb, about $10^9$ $pp$ collision per second will occur on average.

The high-energy frontier at LHC will be explored by detectors located at two collision points: ATLAS [2, 3] at octant 1 and CMS [4, 5] at octant 5, as shown in Fig. 1. By identifying events where large 4-momenta are exchanged between partons, these detectors will probe the force governing Nature in an energy regime never probed before, possibly yielding clues to the fundamental question of the origin of mass, if phenomena related to the Higgs particle are witnessed. In addition, two other experiments will be performed at LHC. The ALICE [6] detector (octant 2) will take data from heavy ions collisions of lead nuclei at the frontier of high energy densities and temperatures (quark–gluon plasma). The LHC-B [7] detector (octant 8) will study the beauty (b) quark physics.

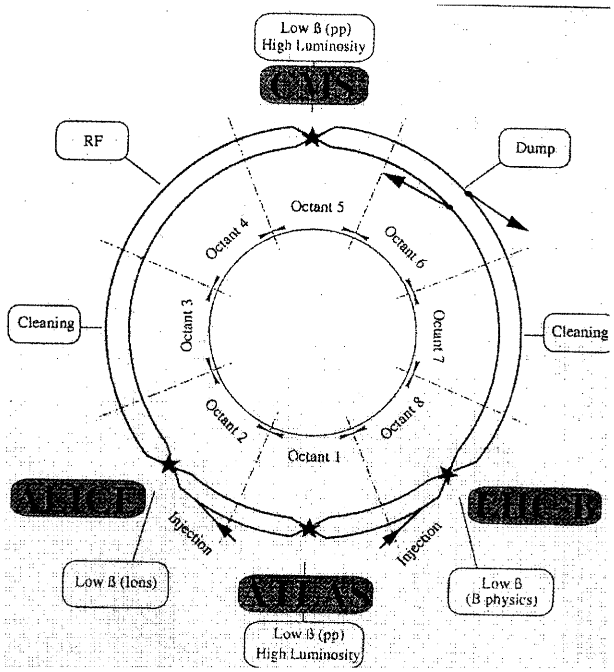

Figure 1: LHC ring layout, serving four main experiments: ATLAS (octant 1), CMS (octant 5), ALICE (octant 2), LHC-B (octant 8).

The LHC will start running in the year 2005. It will investigate the Standard Model further than ever before, and will presumably carry Particle Physics theory beyond the current Standard Model. The Standard Model (SM), a model summarizing our present understanding of the matter constituents and their interactions, has an ad-hoc explanation of the origin of mass, through an idea called the "Higgs mechanism". According to this idea, particles interacting with the Higgs field acquire their masses because the net Higgs field is non-zero. The existence of a spinless Higgs boson particle predicted by the SM, has not yet been observed experimentally. While the SM cannot predict the mass of this particle, it puts the upper limit of its mass at around 1 TeV.

The events that signal the Higgs particle are exceedingly rare. To get an idea of the order of magnitude, one may state that there may be as little as one such event per $10^{13}$ or even $10^{14}$ collisions (considering a few $fb$ Higgs signal [2]). This very fact implies that in order to search for the Higgs particle, the detectors must survive exposure to a gigantic number of particles. These particle fluences will be composed mostly of neutral and charged hadrons coming from the interaction point or backscattered from the calorimeters or reflected by the experiment cavern walls.

Therefore, during the LHC operation high radiation levels are expected around the collision point, particularly at high pseudorapidity [1]. They will be high enough to produce damage in the surrounding detectors and their readout electronics, especially inner detectors and calorimeters.

Detectors based on semiconductors are particularly sensitive to radiation damage, their performance degrading with accumulated dose, and ultimately, their operation ceasing completely. Preamplifiers, and other local trigger and readout electronic instrumentation are also based on semiconductors and are similarly affected, albeit less severely. The survival of the detector

---

[1] The pseudorapidity is defined as $\eta = -\ln(\tan(\theta/2))$, where $\theta$ is the polar angle measured from the $z$ axis (cylinder–axis) and the azimuthal angle $\phi$ from the $x$ axis about the $z$ axis.

components and readout electronics in this high radiation field is not at all assured, and this represents an important challenge to their designers. Moreover, the replacement of damaged components will not only affect the physics program and its cost, but also will lead to significant exposure of personnel during access at the time of accelerator shutdowns, since areas of high radiation levels during running time are usually also areas of high induced radioactivity [8].
For all these reasons, a study of the behavior of detector components and/or equipment in high radiation environments has to be performed, to prove good performance and adequate safety conditions at the predicted fluences and doses generated in the detectors by LHC operation.

The liquid argon technique will be used for the ATLAS (Fig. 2) hadron calorimeters up to pseudorapidities $\eta \leq 5$ (the forward hadron calorimeter and the hadronic end–cap) and for all the ATLAS electromagnetic calorimeters, the electromagnetic barrel and the end–caps. Therefore, in the case of ATLAS, the study of radiation hardness of the components and equipments must take into account the impact of a cryogenic environment. The study has to be done both at room (298°K) and at cryogenic (87°K) temperatures.

Thus, the ATLAS radiation hardness studies are performed in facilities providing exposures of detector components and equipment to neutrons and charged hadrons at both room and cryogenic temperatures. These facilities allow the controlled irradiation of material in radiation fields and beam conditions similar to those encountered at LHC. The damage inflicted to the exposed materials at these facilities is therefore close to what is expected at LHC. The possibility to control the produced particle fluence at these irradiation facilities permits to study the extent of the damage and its evolution as function of the particle fluence and/or as function of the absorbed doses. This requires accurate dosimetric measurements to correlate the observed damage with particle fluence or absorbed dose.

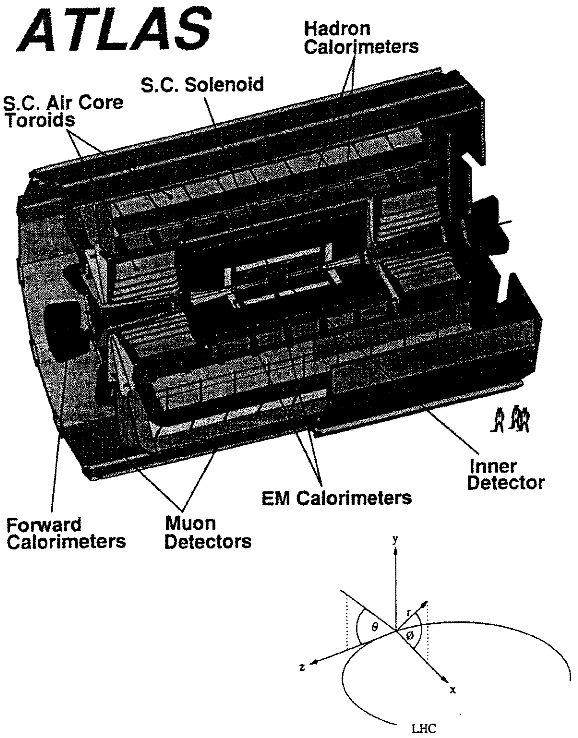

Figure 2: Three–dimensional view of the ATLAS (**A** **T**oroidal **L**hc **A**pparatu**S**) detector to be installed in the LHC [3]. The $z$ axis lies along the beam direction,the $x$ axis points towards the centre of the LHC ring and the $y$ axis is vertical. In polar coordinates, the polar angle $\theta$ is measured from the $z$ axis and the azimuthal angle $\phi$ from the $x$ axis about the $z$ axis.

This thesis is done within the framework of the Canadian contribution to the ATLAS experiment. The Canadian group contribution involves the building of the forward calorimeter (FCAL) and the hadronic end–cap (HEC) calorimeter. The electronic readout systems of these calorimeters include semiconductor materials (silicon, GaAs). The central goal of this thesis is the dosimetric characterization of hadron (n, $\pi$, p) facilities which are used to study the radiation hardness of materials and equipment, and of electronics used in FCAL and HEC. Irradiation studies have been performed in a cryogenic environment. In particular, this thesis will report work done simulating neutron fluxes inside a liquid argon cryostat. The ATLAS Montreal group having a research program on silicon, the present work also establishes irradiation facility characterization from the point of view of performing silicon radiation damage studies.

The neutron irradiation facility SARA (Systéme Accélérateur Rhône–Alpes) was used to perform various neutron irradiation studies. It is installed at a cyclotron located in Grenoble, and permits the exposure of detector scale models, electronic circuits, opto–electronic components such as optical fibers, as well as mechanical parts, at the cryogenic temperature of $87°K$ needed for the operation of liquid argon calorimeters. The neutron beam delivered by this facility is unavoidably contaminated with photons, creating a mixed field situation that must be evaluated.

In fact, mixed field or complex radiations fields will be naturally present in LHC detectors. The irradiation field will contain not only neutrons and photons, but also a large number of pions and protons which can have a particular effect on the exposed components and equipment.

A pion beam ($\pi$E1) at the Paul Scherrer Institute (PSI) was used to study radiation damage in silicon, specially in the $\Delta$ resonance region where the damage from pions is expected to be stronger. The kinetic energy associated with the pions in this region is around 200 MeV. For this purpose, an experiment was performed at 350 MeV/c pion momentum (the corresponding kinetic energy is 237.2 MeV). The effect of proton irradiations was investigated at the ZT7 proton beam of the Proton Synchroton (PS at CERN). The correlation between damage observed in silicon detectors and proton irradiation doses was studied at that facility.

The dosimetric characterization of the irradiation facilities (SARA, $\pi$E1-PSI, ZT7-PS) presented in this thesis (chapter 2) was done measuring hadron fluences and hadron doses, and performing measurements to discriminate particles present in the mixed fields produced at these facilities. This thesis also reports the results of a study of the contamination by other types of particles around the main beam at each facility, during radiation hardness tests of silicon detectors.

The first chapter presents a brief introduction to the radiation environment expected at LHC and to the radiation effects in Si detectors and in liquid argon. Are also described the dosimetry and nuclear activation techniques used to measure doses and particle fluxes and their correlation with the extent of the radiation damage. The experimental dosimetric characterization of the various facilities is the main part of this thesis, presented in chapter 2. Chapter 3 presents the **N**on-**I**onizing **E**nergy **L**oss (NIEL) scaling hypothesis, and its application to the calculation of the "equivalent 1 MeV neutron fluence" and the hardness factor ($\kappa$) for all the irradiation facilities described in this thesis.

## 1.1 The LHC radiation environment

LHC is the first collider where radiation from the beam-beam inelastic collisions will dominate over radiation from beam-gas collisions. Neutrons and photons will be copiously produced as a result of high rate proton–proton collisions at small impact parameter and subsequent hadron interactions in the surrounding material. High–energy particles from the interaction point begin to cascade when entering the detector. The cascade development will continue until most of the charged particles have been absorbed. The remnants are mostly neutrons and associated gamma rays. While electromagnetic cascade are rapidly absorbed, neutrons will travel long distances, losing their energy gradually. Nuclear capture of thermal neutrons frequently results in the production of gamma rays. Gamma rays also result from excited–state decay spallation products and from fast neutron interactions with atomic nuclei.

Silicon detectors will be the material most affected by the radiation in the ATLAS central inner detector (pseudorapidity coverage $\eta=\pm2.5$), where high particle fluences ($\sim 10^{12}$–$10^{13}$ n/cm$^2$/yr [3]) can be expected due to its location close to the collision point. The performance of the associated electronic instrumentation will also be degraded. However, the presence of shielding material installed in the forward region could help absorb neutrons and photons in the central cavity, thus reducing the inflicted damage [9]. The dominant radiation in the internal layers of the inner detector will be charged hadrons, and their presence decreases as a function of 1/r$^2$ (r is the distance from the beam axis).

In the case of the ATLAS calorimeters (see Fig. 2), which use liquid argon as active medium, the highest radiation levels can be expected in the forward ($\eta$ coverage range of 3.1-4.9) and end–cap electromagnetic ($\eta$ coverage range of 1.4-3.2) calorimeters. The component most sensitive to the radiation is the electronics placed in the electromagnetic and the HEC calorimeters. These are warm front-end electronics situated in the gap between the barrel and the end–cap calorimeters, and cold preamplifiers placed in the periphery of hadronic end-cap wheels, receiving about $10^{12}$ n/cm$^2$/yr [10].

The simulation results presented in the following figures correspond to a one year LHC run at high luminosity ($10^{41}$ cm$^{-2}$ yr$^{-1}$) [10]. The "equivalent 1 MeV neutron fluence" for neutrons with energies above 100 keV in the ATLAS calorimeters is shown in Fig. 3.
The integrated dose for photons with energies above 30 keV is shown in Fig. 4.

The pollution of liquid argon due to the outgassing under irradiation of materials immersed in the cryostats is another problem to be considered. A severe signal loss could be observed due to abundant recombinations between charge carriers induced by ionizing particles traversing the calorimeter gap and the impurities released in liquid argon by the outgassing. Many studies of purity evolution during neutron irradiation of different materials have been done at the SARA irradiation facility [10, 11, 12].

There are other sources contributing to the LHC radiation environment:

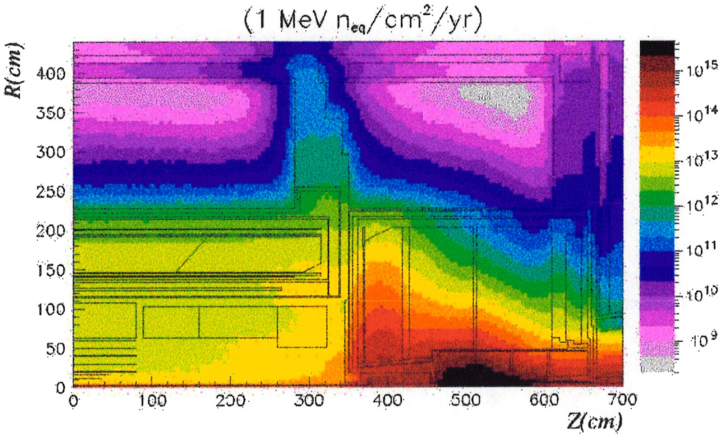

Figure 3: "Equivalent 1 MeV neutron fluence" in the ATLAS detector for neutrons with energy above 100 keV [10].

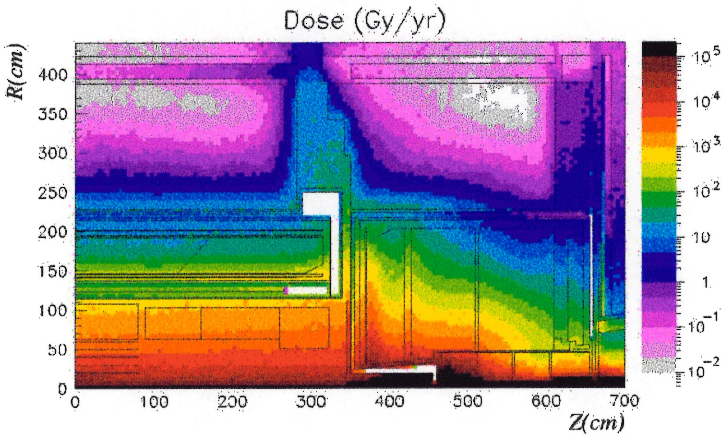

Figure 4: The integrated dose for photons with energies above 30 keV in the ATLAS detector [10].

### Beam losses

The total energy stored in one of the circulating proton beams will be more than 300 MJ [13]. The consequences of the full beam loss at this energy would be dramatic (the beam might bore a hole of several meters depth in any solid object). However, the probability of a full beam loss is very small, *i.e.*, $6\times 10^{-6}$ times per year in any particular sector (5m long) of the LHC circumference ring–tunnel [14]. The total beam loss around the ring should not exceed $10^7$ protons $s^{-1}$, and is relatively small compared with the *pp* collision rate of $\sim 10^9$ $s^{-1}$ per collision point [3].

### Beam–gas interactions

Beam–gas interactions of the circulating proton beam will induce cascades in the superconducting magnets, the concrete and rocks surrounding the ring tunnel. Details of the estimates of total and specific activities due to beam–gas interactions in the main ring magnets, rocks, air, water supply, and ground water, can be found in [15]. Beam–gas interactions are estimated to be $\sim 10^2$ $m^{-1}$ $s^{-1}$ in the interaction area [3].

### Induced radioactivity

High radioactivity will be concentrated in three distinct areas of beam losses: the interaction points of the experiments, the dumps and the collimators [8]. Due to the induced radioactivity levels in the ATLAS and CMS detectors, strictly controlled access and special handling procedures will be necessary to work on equipment in very forward regions close to the beam–pipe.

The dumps (see Fig. 1) will be heavily shielded with iron. The induced radioactivity in these areas will be of the order of several tens of $\mu$Sv/h.

Scraper collimators are needed at LHC. They are installed in the cleaning sections (octants 3 and 7 in Fig. 1). Their purpose is to limit the beam size by scraping off the halo particles and prevent them from depositing energy in the coils of the superconducting magnets [8].

## 1.2 Radiation effects in semiconductors

Degradation produced by radiation in Si are separated into two categories [16, 17, 18], bulk effects and surface damage.

### 1.2.1 Bulk damage

Bulk damage or displacement damage is due to the Non–Ionizing Energy Loss (NIEL) of the incoming particle interacting with the atoms of the silicon lattice by collision, producing atom displacements or nuclear reactions. A lattice atom dislodged by an incoming particle is known as a primary knock–on atom (PKA), the average energy to produce a PKA in Si is about 25 eV [19]. The dislodged atom leaves its site (thus creating a vacancy) and collides with other atoms in the lattice, creating at the end of its range multiple displacements in a microscopic disordered region called "cluster" [20, 21, 22].

A cluster will affect the electrical properties of the semiconductor introducing changes in the band gap. The effect of unwanted energy levels in the band gap is an increase of leakage current in depleted detectors. A second consequence is the creation of trapping centres, which could lead to slow charge collection. Another important phenomenon is the presence of many defect centres created by displacement damage which are acting to compensate the material and thus change the resistivity, or doping, of the bulk silicon.

Light particles like electrons create localized point defects (the least severe kind of defects). In the case of energetic protons, neutrons and heavy particles, the knock–on atoms produce additional knock–on atoms and vacancy–interstitial pairs. A vacancy–interstitial pair is called a Frenkel defect. Frenkel defects are unstable at room temperature and may migrate through the lattice, but they can produce stable complex defects, by combining with each other or with impurity atoms or by being trapped at the surface.

### 1.2.2 Surface damage

Surface damage is produced when the ionizing radiation interacts with the silicon–silicon dioxide interface on silicon devices, creating electron–hole pairs in the interface [21, 26, 20]. These pairs are created at a rate proportional to the ionization energy deposition, for example in $SiO_2$ approximately 18 eV of ionization energy is consumed per electron–hole pair created.

Many of the electron–hole pairs find themselves close together to recombine before they are swept apart by diffusion or drift in an applied electric field. The electrons that do not recombine are quickly swept through and out of the oxide, leaving the less mobile holes behind moving slowly in the opposite direction. In some cases, this direction can be toward the oxide–silicon interface and holes are trapped there, enhancing the fixed charge or the interface states (surface mid–gap energy levels).

The net effect of the charges introduced into the oxide and at the interface is to change the electric field imposed upon the active semiconductor region from the surface. The additional charge causes a shift of the flat band voltage of MOS (Metal Oxide Semiconductor) structures. Silicon radiation detectors with oxide passivated edges, such as silicon microstrip detectors, can show an increase of surface leakage current due to trapped interface charges.

We now consider the problem of accurate determination of absorbed doses and particle fluxes.

## 1.3 Dosimetry and nuclear activation technique

### 1.3.1 Dosimetry

The ideal dosimeter for the measurement of the absorbed dose during radiation hardness tests of materials should present the following features:

- A chemical composition as close as possible to the tested material.
- Easy calibration and coverage of a wide dose range.
- A response independent of dose-rate.
- A response independent of the energy (as much as possible).
- A reproducible response (uncertainties less than ±5%).
- Small size and easy handling.
- Re-usability.
- Rapid, simple and unambiguous readout.
- Commercial availability and low cost.

The atomic composition of the dosimeter should be as similar as possible to the medium in which the absorbed dose has to be measured, in order to reduce the perturbations from the particle fluence. The ideal situation is achieved when the dosimeter material is matched to the medium, otherwise corrections must be applied in order to determine the absorbed dose in the corresponding medium. The size of the dosimeter must be small enough to minimize local perturbations of the incoming particle fluence, but large enough to be subjected to a large number of interactions and thus to yield a signal that can be read with precision. In the case of mixed fields, it is useful to have a family of dosimeters, with a small variation in their composition, presenting different sensitivities to each type of radiation.

The dosimeters are generally calibrated with gamma radiation from $^{60}$Co ($E_\gamma$ = 1170 and 1330 keV) or $^{137}$Cs ($E_\gamma$ = 662 keV) sources in approximate charged particle equilibrium (CPE) or electron equilibrium [2]. In the case of gamma radiation from $^{60}$Co source, the approximate electron equilibrium in a small irradiated dosimeter can be achieved with about 0.5 g cm$^{-2}$ of material (usually plexiglass) surrounding it. This corresponds to the approximate range of the highest energy secondary electrons produced by 1250 keV photons (mean value of the two photon energies: 1170 and 1330 keV). For gamma radiation from a $^{137}$Cs source, the mass per unit area for approximate electron equilibrium is about 0.25 g cm$^{-2}$. For neutron calibration, one can calibrate the dosimeters using a Pu-Be neutron source.

A dosimeter placed in a radiation field will interact with the radiation. This interaction will produce a physical or chemical change in the dosimeter struc-

---

[2] **Charged–particle equilibrium (CPE):** Condition in which the kinetic energy of electrons (or charged particles) entering an infinitesimal volume is equal to the kinetic energy of electrons emerging from it.

ture. Adequate read–out systems then measure the physical or chemical changes that are functions of the absorbed dose.

In the present work, the measurements of the absorbed doses at the irradiation facilities were done with alanine and thermoluminescent dosimeters. A brief description of these dosimetry methods is presented in Appendix A.

### 1.3.2 The Nuclear activation technique

The nuclear activation technique gives the possibility of measuring the flux density of various types of particles produced at irradiation facilities [27, 28, 29, 30, 31, 32, 33]. These measurements are based on the production of radioactive nuclei through nuclear reactions induced by particles in selected target elements (activation foils). The radioactivity decay of the created radio-nuclei can be measured by spectrometry ($\gamma$ or $\beta$). For this purpose, the targets are thin activation foils (typically $<$ 1mm thick), usually cut away from commercially available 15 $\times$ 10 $cm^2$ sheets. Activation is driven by nuclear reactions [34, 35, 36, 37] and is detected through radioactive decays [38, 39].

#### Activation formula

The number, N, of radioactive nuclei produced by irradiation per gram of target material (or foil) per unit of time is a function of : a) the particle flux density $\varphi$ (particles/$cm^2$/s), b) the number $N_0$ of atoms per gram of target material (or foil) and c) the cross-section $\sigma$(E) of the particular nuclear reaction. N can be expressed as:

$$N = \varphi \, N_0 \, \sigma \tag{1.1}$$

where $N_0$ (atoms per gram) is the Avogadro's number $N_a = 6.02 \times 10^{23}$ (atoms per mole) divided by the atomic weight (or mass number) A, *i.e.* $N_a/A$.

In order to take into account the weight W(gr) of the target material of atomic mass A, the isotopic abundance (purity) P of the target material, one can define a quantity $N_0'$ as follows:

$$N_0' = N_0 \times P \times W \tag{1.2}$$

Equation 1.2 can be rewritten as:

$$N_0' = N_0 \times P \times x \times S \times \rho \tag{1.3}$$

where:

$x$ = Thickness of the foil ($cm$).
$S$ = Surface of the foil ($cm^2$).
$\rho$ = Density of the foil ($g/cm^3$).

The number, N, of radioactive nuclei produced by irradiation decays according to the exponential law:

$$N(t) = N(0)e^{-t/\tau} \tag{1.4}$$

where $\tau$ is the mean lifetime of the produced nuclei (time during which the amount of nuclei initially present is reduced from 1 to $1/e$). $\tau$ is linked to the decay constant $\lambda$ and to the half-life time $T_{1/2}$ of the nuclei, as follows:

$$\tau = \frac{T_{1/2}}{\ln 2} = 1/\lambda \tag{1.5}$$

If the target material is irradiated uniformly during a length of time t$_i$ (irradiation time), the number of radioactive nuclei N(t$_i$) existing at the instant the irradiation stops is given by:

$$N(t_i) \;=\; \varphi\, N_0\, \sigma \int_0^{t_i} e^{-t/\tau}\, dt \tag{1.6}$$

$$N(t_i) \;=\; \varphi\, N_0\, \sigma\; \tau \left(1 - e^{-t_i/\tau}\right) \tag{1.7}$$

A "cooling" time, t$_e$, can be defined. It is the time elapsed between the end of the irradiation and the beginning of the sample activation measurements. So, N(t$_i$) (the number of radioactive nuclei existing at the instant the irradiation stops) will decrease to the value

$$N(t_i, t_e) \;=\; \varphi\, N_0\, \sigma\; \tau \left(\; 1 - e^{-t_i/\tau} \;\right) e^{-t_e/\tau} \tag{1.8}$$

The activity, *Act*, of an irradiated material is defined as the number of radioactive nuclei disintegrations per unit of time:

$$Act = -\frac{dN}{dt} \tag{1.9}$$

Therefore, the activity, *Act*, is obtained by differentiating the quantity N(t$_i$, t$_e$) (number of radioactive nuclei existing at the time to start the activity measurements) with respect to t$_e$.

$$Act = -\frac{dN}{dt_e} = \varphi\, N_0\, \sigma \left(\; 1 - e^{-t_i/\tau} \;\right) e^{-t_e/\tau} \tag{1.10}$$

Equation 1.10 is the *activation formula* [37]. It gives the value of the activity or the number of disintegrations per second of a particular nuclei which has been produced during the irradiation time $t_i$ and left to decay during a time $t_e$. Equation 1.10 is represented in Fig. 5.

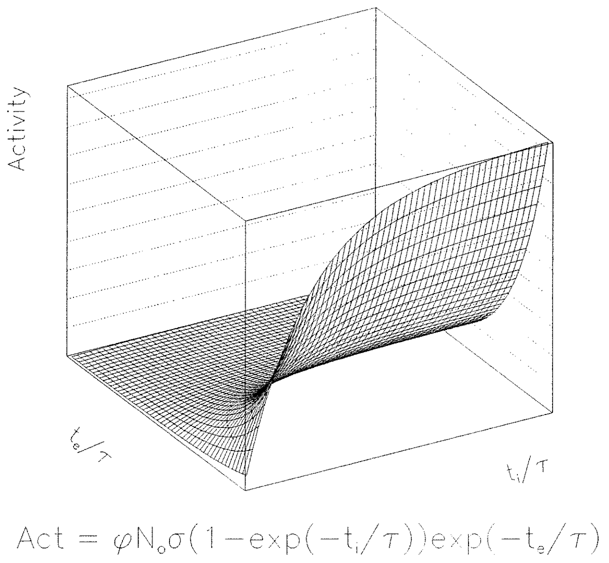

Figure 5: Activity (Act) of a nucleus produced during irradiation along a time $t_i$ and left to decay during a time $t_e$ (elapsed time).

From equation 1.10, one can see that if the irradiation time $t_i$ is large compared with the decay time $\tau$ of a particular isotope, the activity at $t_e = 0$ has a limit called saturation activity

$$Act_{sat} = \varphi\, N_0\, \sigma \tag{1.11}$$

This is due to the fact that the nuclei produced during irradiation have time to decay before the end of irradiation. At saturation, the rate of formation is equal to the rate of disintegration of the radionuclei. This saturation value is a natural limit of the specific activity (disintegrations per second per gram) obtained with a given particle flux density.

Equation 1.11 shows that the saturation does not depend on the decay constant but only on the cross-section value and the irradiating flux density. A graphical representation of equation 1.11, for $t_e$=0, is given in Fig. 6. The activity value at saturation, noted $A_\infty$, is also shown in the same figure. This value is obtained theoretically for a very long irradiation time ($t_i \rightarrow \infty$). Practically, it is obtained for irradiation time about 5-7 times the half-life, within 1%.

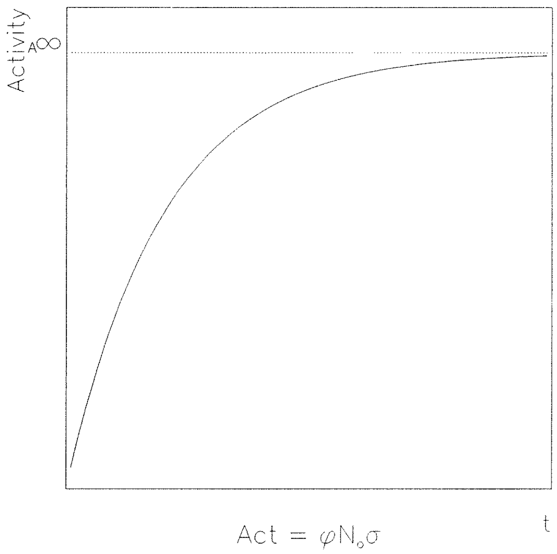

Figure 6: Saturation activity, $Act_{sat}$, obtained at $t_e = 0$ and $t_i \rightarrow \infty$. $t_e$ is the elapsed time and $t_i$ is the irradiation time.

In the usual experimental conditions, one more correction has to be applied to equation 1.10. It depends on the period of time during which the sample activity is measured. During this counting time, $t_c$, there is a decay of the original activity [3]. The situation is depicted in Fig. 7.

---

[3] When the Intergamma code [40] is used to measure activity, the $t_c$-dependent correc-

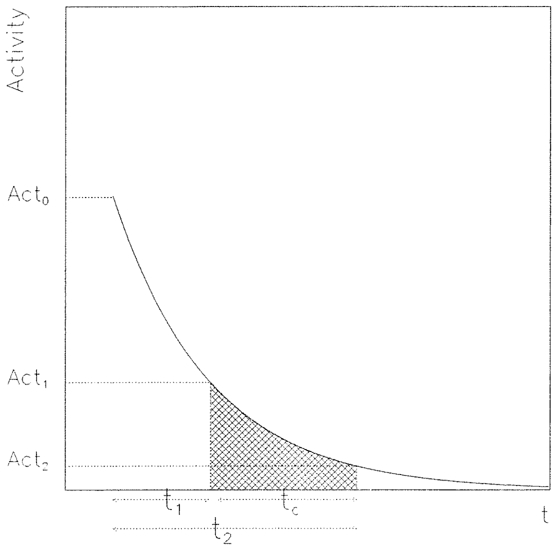

Figure 7: Decay of the activity during counting time $t_c$. $Act_0$ is the activity at the end of the irradiation. $Act_1$ and $Act_2$ are the activity at the beginning and at the end of the measuring time. $t_1$ is the time of the beginning of the activity measurement and $t_2$ is the time at the end of it.

The following equations have to be considered to calculate the decay during the counting time:

$$Act_1 = Act_0\, e^{-\lambda t_1}, \quad Act_2 = Act_0\, e^{-\lambda t_2} \tag{1.12}$$

where $Act_1$ and $Act_2$ are the activity at the beginning and at the end of the measuring time, respectively. $Act_0$ is the activity at the end of the irradiation, $t_1$ is the time at the beginning of the measuring time and $t_2$ is the time at the end of it.

---

tion factor must not be applied because it is already applied by this code.

The average value of activity, $\overline{Act}$, during the counting time is then given by:

$$\overline{Act} = \frac{Act_0}{t_c} \int_{t_1}^{t_2} e^{-\lambda t}\, dt \qquad (1.13)$$

$\overline{Act}$ is the value of the activity given by the measuring instrument (spectrometer) and $t_c = t_2 - t_1$. Equation 1.13 gives after integration:

$$\overline{Act} = \frac{-Act_0}{\lambda\, t_c}(e^{-\lambda t_2} - e^{-\lambda t_1}) = \frac{-1}{\lambda t_c}(Act_2 - Act_1) \qquad (1.14)$$

Since $Act_2$ can be expressed as a function of $Act_1$ and $t_c$, one has:

$$\overline{Act} = \frac{-1}{\lambda\, t_c}(Act_1\, e^{-\lambda t_c} - Act_1)$$

$$\overline{Act} = \frac{Act_1}{\lambda\, t_c}(1 - e^{-\lambda t_c}) \qquad (1.15)$$

and then

$$Act_1 = \frac{\overline{Act}\lambda\, t_c}{(1 - e^{-\lambda t_c})} \qquad (1.16)$$

Using equation 1.10 with $Act_1 = Act$, and equation 1.11, the final expression is now obtained:

$$Act_{sat} = \frac{\overline{Act}\,\lambda\, t_c\, e^{\lambda\, t_e}}{(1 - e^{-\lambda\, t_c})(1 - e^{-\lambda\, t_i})} \qquad (1.17)$$

**Particle flux density formula**

The particle flux density expression becomes:

$$\varphi = \frac{\overline{Act}\,\lambda\, e^{\lambda\, t_e}\, A\, t_c}{N_a\, P\, W\, \sigma\, (1 - e^{-\lambda\, t_c})(1 - e^{-\lambda\, t_i})} \quad (particles/cm^2\,/s) \qquad (1.18)$$

In the case $t_i \ll \tau = 1/\lambda$, equation 1.18 can be modified as follows (because $e^{-\lambda\, t_i} \cong 1 - \lambda\, t_i$),

$$\varphi = \frac{\overline{Act}\, e^{\lambda\, t_e}\, A\, t_c}{N_a\, P\, W\, \sigma\, (1 - e^{-\lambda\, t_c})\, t_i} \tag{1.19}$$

Equation 1.18 can be further modified if $t_c \ll \tau$:

$$\varphi = \frac{\overline{Act}\, e^{\lambda\, t_e}\, A}{N_a\, P\, W\, \sigma\, (1 - e^{-\lambda\, t_i})} \tag{1.20}$$

If $t_e \ll \tau$, which means $\lambda\, t_e \ll 1$, equation 1.18 becomes:

$$\varphi = \frac{\overline{Act}\, \lambda\, t_c\, A}{N_a\, P\, W\, \sigma\, (1 - e^{-\lambda\, t_c})(1 - e^{-\lambda\, t_i})} \tag{1.21}$$

If the times $t_i$, $t_e$ and $t_c$ are all $\ll \tau$, equation 1.18 becomes a very simple expression:

$$\varphi = \frac{\overline{Act}}{N\, \sigma\, \lambda\, t_i} \tag{1.22}$$

Using the previous equations (equation 1.18 to equation 1.22), the particle fluence is then obtained as:

$$\Phi = \varphi \times t_i \quad (particles/cm^2) \tag{1.23}$$

where $t_i$ is the irradiation time.

The number of particles entering the target of area S($cm^2$) is then given by:

$$n = \Phi \times S \quad (number\ of\ particles) \tag{1.24}$$

## 1.4 Correlation of radiation damage with particle fluences and absorbed doses

The operation of semiconductor detectors in the ATLAS and CMS radiation environments is most challenging. As was explained in section 1.2, there are two different radiation damage effects on silicon: firstly, bulk damage or displacement damage, caused by the non–ionizing energy loss of penetrating particles, results in crystal defects. The consequences of the bulk damage are the change of the effective doping concentration (controling the value of the depletion voltage in detectors), the increase of the leakage current and the deterioration of the charge collection efficiency.

Secondly, surface damage which is produced by the ionizing particles in the passivation layers at the surface of the silicon detectors.

While bulk damage is function of the measured particle fluence, the surface damage effect is function of the ionizing absorbed dose.

### 1.4.1 The effective doping concentration

The effective doping concentration ($N_{eff}$) can be expressed as a function of the particle fluence ($\Phi$) by:

$$|N_{eff}| = |-N_d\, exp(-c\Phi) + b\Phi| \tag{1.25}$$

where $N_d$ is the initial donor concentration. This concentration decreases exponentially at a rate determined by the parameter $c$ (donor removal constant). The term $b$ is the acceptor creation rate.

Hadron irradiations beyond a fluence of $\approx 10^{12}$ - $10^{13}$ particles/cm$^2$ cause an inversion of the original n–type to p–type silicon, as shown in Fig. 8.

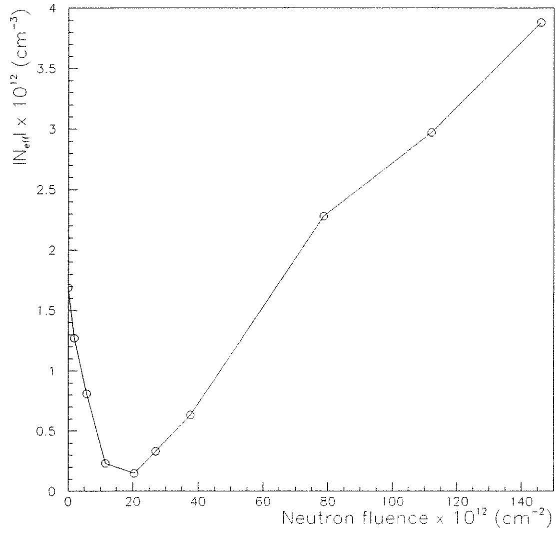

Figure 8: Effective doping concentration, $N_{eff}$, as a function of neutron fluence [41]. As can be seen the inversion fluence is $\approx 2 \times 10^{13}$ n/cm$^2$. The energy of the neutrons was in the typical 1–2 MeV of energy range.

### 1.4.2 Increase of leakage current

The increase of the leakage current as a result of bulk damage is due to the formation of defect levels in the forbidden gap, acting as generation/recombination centers for the charge carriers in silicon.

The linear increase of the detector current ΔI per sensitive volume $V$ is proportional to the particle fluence $\Phi$ (see Fig. 9):

$$\Delta I = \alpha \Phi V \tag{1.26}$$

The proportionality constant $\alpha$ is called the radiation–induced leakage current damage constant. This constant is strongly dependent on the detector temperature, therefore, for a comparison of different experimental results, the $\alpha$-values have to be normalized to the same temperature. Additionally, the detector could present self annealing, then a correction must be applied depending on the duration of the irradiation and the elapsed time between irradiation and measurement.

A compilation of the damage constant $\alpha$ has been done by Hall [21, 42]. He has estimated $\alpha = 6.9 \times 10^{-17}$ A cm$^{-1}$ for neutrons and $\alpha = 2.9 \times 10^{-17}$ A cm$^{-1}$ for charged particles.

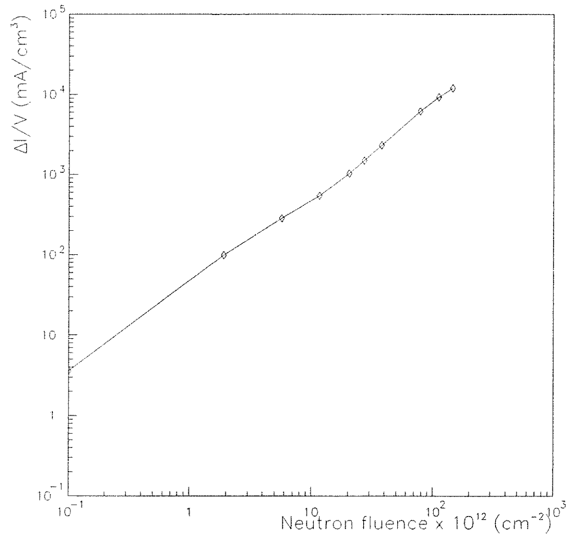

Figure 9: Leakage current versus neutron fluence for Si detector of 300 $\mu$m thickness [41].

### 1.4.3 Charge collection deficiency

Measurements of the charge collection deficiency due to electron and hole trapping can be obtained following the method described in [43], using monoenergetic alpha particles incident on the front and rear side of the detector. For a specific experiment, knowing the actual field distribution in the bulk of the detector, and knowing the electron and hole velocities as function of the electric field strength, one is able to extract the respective time constants $\tau_e$ and $\tau_h$ for electrons (front incident) and hole trapping (rear incident). The time constants ($\tau_e$ and $\tau_h$) are proportional to the inverse values of the trapping centers concentrations ($t_{c,e}$ and $t_{c,h}$).

The resulting charge loss for minimum ionizing particles (mip) can be calculated according to:

$$\frac{\Delta Q}{Q_0} = \frac{1}{6}\left[\frac{t_{c,e}}{\tau_e} + \frac{t_{c,h}}{\tau_h}\right] \tag{1.27}$$

This relation $\Delta Q/Q_0$ (charge collection deficiency) varies linearly with the neutron fluence $\Phi$, following the relation:

$$\frac{\Delta Q}{Q_0} = \gamma\,\Phi \tag{1.28}$$

where $\gamma$ is the damage rate, related to charge trapping. Charge collection deficiency plotted as function of 5 MeV neutron fluences in Fig.10.

### 1.4.4 Total dose effect

The total dose effect is the creation of hole–electron pairs in silicon–silicon dioxide interface on silicon devices. The trapping of the holes created at the interface between the Si and $SiO_2$ layers causes free electrons to be attracted

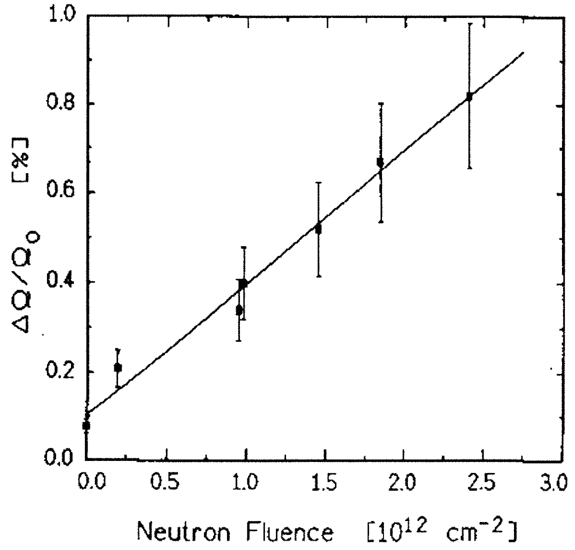

Figure 10: Estimated charge collection deficiency for **mip**'s as function of 5 MeV neutron fluence [44].

to the interface. The consequence of the hole trapping is an inversion of the doping in the silicon near the interface. Thus p–doped silicon can become n–type in the region adjacent to the interface. In addition to the hole trapping phenomena, energy states are formed within the silicon–silicon dioxide interface. The consequences of the energy states created are an increase in the gate voltage of n and p channel MOS (Metal Oxide Semiconductor) transistors and a reduction in carrier channel mobility.

# Chapter 2

# Hadron Facilities

The future Large Hadron Collider (LHC) at CERN will allow head–on collision of two high energy proton beams accelerated each at 7 TeV. In two detectors CMS and ATLAS, the LHC beam optics will produce the high luminosity of $10^{34}$ $\mathrm{cm}^{-2}$ $\mathrm{s}^{-1}$, achieving collision rates of $10^9$ collisions per second. At LHC, each inelastic collision will produce approximately one hundred particles (neutral and charged), with a wide energy spectrum from a few keV to several GeV.

The detectors and electronics will be exposed to high radiation levels, especially if they are located very close to the interaction point. These radiations will possibly inflict damage to the detectors components, materials and equipment, and in turn spoil the quality of the information expected from these detectors.

Furthermore, as underlined in chapter 1, electromagnetic and hadronic calorimeters with liquid argon as active medium will be used for the ATLAS detector, and this raises the question of the radiation damage of the detector components at cryogenic temperatures. Additionally, front-end electronics, charge preamplifiers directly mounted on the calorimeter and preamplifiers used at liquid argon temperature will also be exposed to radiations.

The absorbed doses and the neutron fluences predicted in various parts of the ATLAS detector are given in [2]. For example, a large neutron fluence ($2.7 \times 10^{13}$ neutrons/cm $^2$/year) and a large absorbed dose rate in Si ($1.5 \times 10^4$ Gy/year) are expected [2] in the inner layers of the SCT (semiconductor tracker) barrel of the ATLAS detector.

The achievement of the physics program at LHC, including the search for new fundamental particles, will be then compromised if the effect of radiation damage on the behaviour and response of the detectors is not correctly evaluated and tested. These evaluation and tests have to be performed at dedicated irradiation facilities where test benches are available. The correct assessment of these damages through an irradiation test bench depends on the choice of an irradiation facility where the particle composition and energy distribution present at LHC can be approached. Thus, ultimately, the fulfillment of an optimized irradiation study program is very important to achieve a successful LHC physics research program.

In this chapter are presented the results of the dosimetric measurements at the SARA neutron irradiation facility (section 2.1) and at two charged irradiation hadron facilities: a pion facility at the Paul Scherrer Institute (PSI) and a proton facility at the Proton Synchrotron (PS) at CERN (section 2.2).

## 2.1 Neutron facility: SARA

SARA (Systéme Accélérateur Rhône–Alpes) is a heavy ion accelerator dedicated to nuclear physics studies located at Grenoble, France [45]. Neutrons are produced by stopping a 20 MeV deuteron beam (5 $\mu$A beam) on a beryllium target (3 mm thick, 35 mm diameter) by stripping reactions: $^{9}$Be(d,n)$^{10}$B.

This facility reproduces the high neutron fluences (up to $\sim 10^{13}$–$10^{14}$ neutrons/cm$^2$/yr) and doses expected in the ATLAS detector, especially in the liquid argon calorimeters. The facility is equipped with a 10 liters cryostat. The large cryostat volume permits the study of radiation damage of large surfaces exposed to large fluxes of neutrons. Radiation damage studies can be performed at room and cryogenic temperatures.

At the SARA facility, it is possible to irradiate various types of detectors, readout electronics and mechanical parts to high fluences of neutrons. This facility makes also possible the study of the pollution of liquid argon by radiolysis under neutron radiation of the polymeric components of the ATLAS calorimeter [11, 12]. If, for example oxygen was released in the liquid argon with a concentration of 10 ppm, the calorimeter signal could be reduced by 10% because of the capture of electrons by oxygen or oxygen–type impurities in the argon gaps.

The description and details of the neutron facility can be found in [30], which is attached to this thesis (appendix C) and in [46, 47]. A time-of-flight (TOF) technique was used to measure the neutron energy spectrum [30, 46, 47].

The neutron energy spectrum inside the liquid argon cryostat must be estimated, since its direct measurement is difficult. The temperature by itself does not modify significantly this energy spectrum, but the presence of liquid argon does, because there is enough argon to scatter or absorb a significant fraction of the incoming neutrons. Thus, the liquid argon present in the cryostat may change a lot the spatial and momentum distribution of neutrons. The neutron energy spectrum at liquid argon temperature inside the cryostat is estimated using the FLUKA Monte–Carlo code. The details of this simulation have not been published before. The following simulation results are a part of my contribution to the SARA irradiation study program (subsection 2.1.1). Dosimetric measurements and dose–rate estimate are another part of my contribution to the SARA irradiation study program (subsection 2.1.2). Alanine dosimeters were used to measure the angular total absorbed dose in order to know how uniform is the dose in the radiation field of the facility [30] (appendix C) and in [46, 47].

In addition, the use of thermoluminescent dosimeters allowed the determination of the neutron and photon doses in the radiation field [48]. Results of the flux density measurements were applied to the estimate of the neutron dose–rates in Si and $SiO_2$ as part of the radiation hardness research program at SARA. These estimates have not been published before.

### 2.1.1 The neutron spectrum inside the liquid argon cryostat

The TOF (time-of-flight) method was chosen to measure the neutron spectrum at room temperature. It distinguishes photons, which move at the velocity of light, $c$, from fast neutrons, which are slower (about 10% of $c$).

The neutron spectrum at room temperature in the beam direction, was measured using alternatively two TOF detectors. One was a cylindrical scintillator (NE213) neutron detector operated with a neutron energy threshold of 1 MeV, to cover the high–energy part of the spectrum. It measured the

TOF of neutrons over a target–to–detector distance of 2.5 m.

The other detector, used for the low energy part of the spectrum (down to 100 keV) was a fission detector consisting of a $^{235}$U plate mounted a few mm in front of a silicon diode. The neutron flux density at 0° was found to be equivalent to $4.8 \times 10^7$ (± 15%) neutrons/nA/sr/s, it shows a mean energy of 6 MeV (Fig. 11). The TOF neutron spectrum at room temperature will be used as an input file to estimate the neutron energy spectrum inside the liquid argon cryostat. More details about the TOF measurements can be found in [30] (appendix C) and in [46, 47].

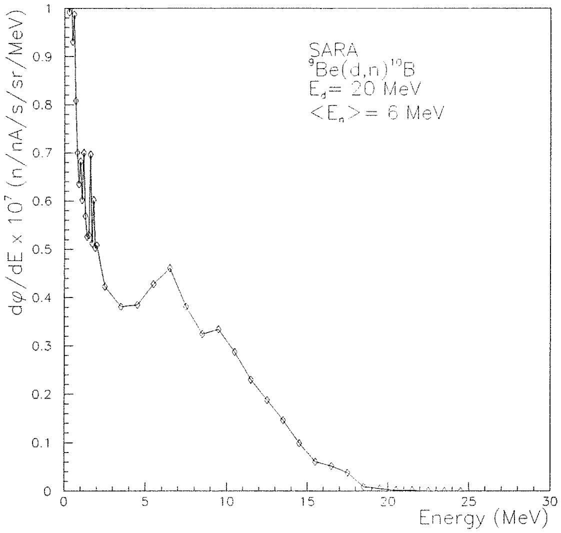

Figure 11: The neutron energy spectrum measured by TOF technique at 0° angle and at room temperature. The mean neutron energy is 6 MeV.

The neutron spectrum at liquid argon temperature inside the cryostat was estimated using the FLUKA Monte–Carlo simulation program. This estimate was done using the fluxes measured outside the cryostat (TOF neutron spectrum at room temperature) as an input file. FLUKA is written in FORTRAN and it is very well suited for this particular purpose of calculating the ratio of two fluxes dominated by hadrons. The version of FLUKA used in the present study is FLUKA92 [49, 50, 51, 52].

### Details of the simulation of the neutron spectrum at SARA at liquid argon temperature

*Geometrical modeling of the experimental arrangement:* the cryostat structure consists of two aluminium coaxial (Z–axis) cylinders of 0.5 cm thickness, with a 4 cm gap between the inner and outer cylinder. The upper part of the inner cylinder is filled with argon gas ( 60% of the total volume) and the lower part filled with liquid argon (40% of the total volume). A small silicon cubic sample is placed in the liquid argon at different distances from the neutron source along the X–axis (see Fig. 12). The target Be disk (3 mm thick, 35 mm diameter) is placed in front of the cryostat and it is centered on the X–axis. The various structures (neutron source, cryostat, and silicon sample) were modeled each having a distinct chemical composition [53, 54].

*The incident beam:* It is taken to be a pure neutron beam, with an energy spectrum equivalent to the one measured experimentally (at room temperature). To achieve this, one uses the capability of the FLUKA program to call a user–provided routine to attribute the initial energy of the individual beam particles. The name of this routine is SOURCE. Inside that routine, it was arranged the HRNDM1 function of the CERN HBOOK library [55] to

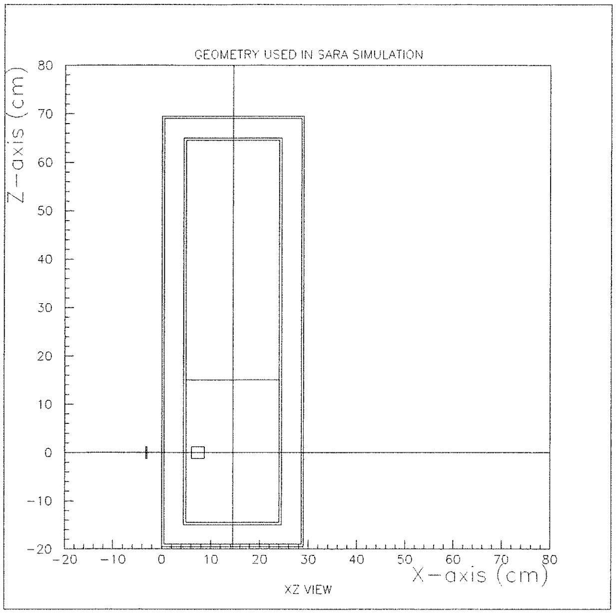

Figure 12: The FLUKA geometry used to obtain the neutron energy spectrum inside the liquid argon cryostat. The neutron source is situated at (-3.15,0) and the silicon sample is situated at (7.4,0).

generate particles according to the experimental distribution determined by the TOF data, which was entered as a histogram (see Fig. 11). The beam is thus polyenergetic, with a minimum energy of 100 keV, and a maximum energy of 25 MeV. Its projected distributions on the horizontal and vertical planes were assumed to be Gaussian. The standard deviations of the projected horizontal and vertical beam profile distributions were both 0.6 cm. The beam was incident on the center of the silicon sample placed inside the liquid argon cryostat (see Fig. 12).

*Simulation of the particle transport:* The FLUKA92 standard procedure was applied for particle transport calculations [50, 51]; charged particles (protons and pions) of kinetic energy less than 10 MeV were followed for their eventual contribution to the flux, but were not scattered. Neutrons were followed down to thermal energies.

*Description of the scoring procedures:* The evaluation of the flux was made by a logarithmic-binning track-length (USRTRACK) evaluation in the volume of the silicon sample placed inside the liquid argon cryostat (see Fig. 12).

To assess the quality of the simulation, the effect of various situations were studied, as described below:

Firstly, the neutron fluence measurements as a function of the sample area were investigated, fixing the distance between the neutron source and the sample. The sample material was silicon. The ratio between neutron fluence "inside" the liquid argon cryostat ($\Phi^{liq.argon}$) and neutron fluence "outside" the cryostat at room temperature ($\Phi^{TOF}$) as a function of the sample area is shown in Fig. 13. The number of neutrons observed in the sample per incident neutron is a function of the sample size; but beyond a certain area ($2.5 \times 2.5$ cm$^2$) the variation of this quantity is very small, *i.e.* almost independent of the area. This was to be expected, because the full width at half maximum ($(8 \ln 2)^{1/2} \times \sigma$) of the beam is approximately 1.4 cm. The reason is probably that with such a sample area the tails of the Gaussian distribution of direct neutrons can be covered.
However, the ratio $\Phi^{liq.argon}/\Phi^{TOF}$ never reaches 1, possibly indicating that part of the neutrons are scattered at large angles or absorbed by the liquid

argon.

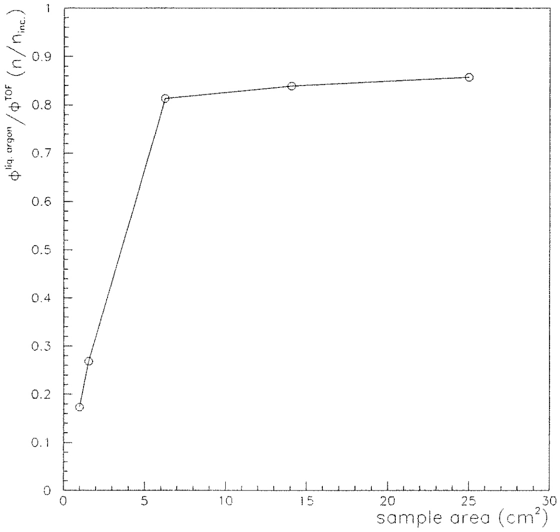

Figure 13: Ratio of "inside" to "outside" of the cryostat neutron fluences as a function of the sample area. $\Phi^{liq.argon}$ is the "inside" neutron fluence and $\Phi^{TOF}$ is the "outside" neutron fluence.

Secondly, fixing the sample size (2.5 × 2.5 $cm^2$), the variation of the neutron energy spectrum inside liquid argon as a function of the distance, $d$, between the neutron source and the sample was also analyzed. The distances considered were: $d=$ 9.3, 10.3, 11.3, 14.3, 16.3, 18.3 and 21.3 cm. The neutron energy spectrum inside liquid argon at 0° angle, plotted according a logarithmic scale, at different distances from the source is shown as a function of the neutron energy in Fig. 14. The neutron energy spectrum measured by TOF at room temperature is also shown as a comparison. It is seen that the overall yield is lower at larger distances; in addition, the shape of the distribution changes somewhat: this change is more noticeable at low neutron energy.

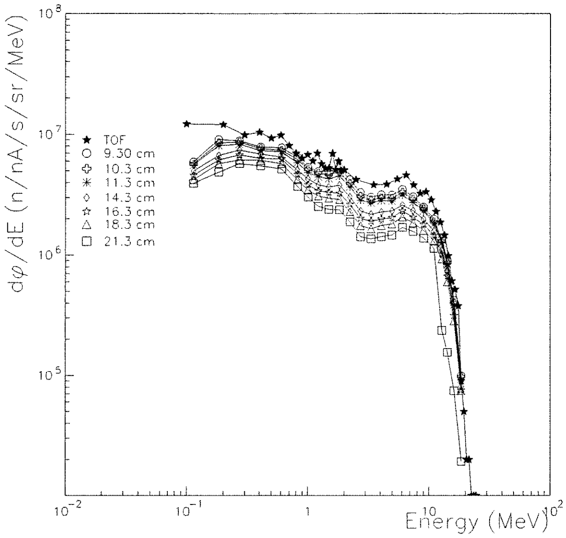

Figure 14: Neutron energy spectrum inside liquid argon cryostat at 0° angle as a function of the neutron energy and at different distances, $d$, from the source. The neutron spectrum measured by TOF ($\star$) is also shown.

From the same simulation data used above, one can also quantify the attenuation (relative to the external neutron fluence) of the neutron fluence inside the liquid argon cryostat, *i.e.* the ratio between the number of neutrons observed in the sample per incident neutron ($\Phi^{liq.argon}/\Phi^{TOF}$), as a function of the distance, $d$. These ratios are shown in Fig. 15. At the position $d = 10.3$ cm (2.15 cm in liquid argon), the total attenuation of the neutron fluence inside the liquid argon cryostat is equivalent to 22% of the neutron fluence at room temperature. At the position $d = 18.3$ cm (10.15 cm in liquid argon) the neutron fluence is reduced by 49%. The minimal irradiation distance is $d$ = 10 cm (liquid argon cryostat installed as close as possible to the Be target).

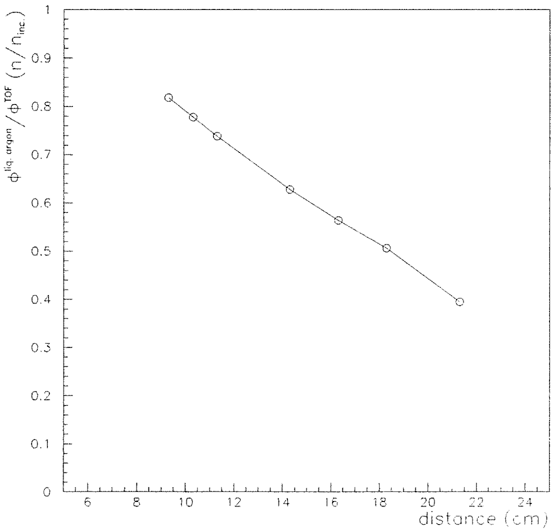

Figure 15: Attenuation of the neutron fluence inside the liquid argon cryostat ($\Phi^{liq.argon}$), relative to the external neutron fluence ($\Phi^{TOF}$), as a function of the distance, $d$, from the neutron source to the sample.

The contribution of low energy neutrons to the neutron fluence inside the liquid argon cryostat, was also analyzed at the distance $d$ = 9.3, 10.3, 11.3, 14.3, 16.3, 18.3 and 21.3 cm between the neutron source and the sample. The low energy flux density, *i.e.* the flux density of the neutrons with energies below 100 keV is shown in Fig. 16. It is noted that the low energy flux density (below 100 keV) decreases less with distance (40 % from the first to the last point in the curve) than the flux density above 100 keV (55.7 % from the first to the last point in the curve). Nonetheless, the low energy flux density is a hundred times smaller than the neutron flux density above 100 keV, and therefore is practically negligible.

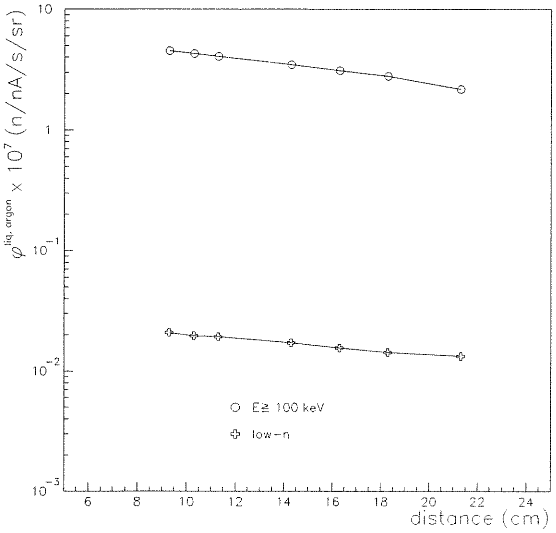

Figure 16: Flux densities of the neutrons inside liquid argon cryostat with energies below and above 100 keV at different distances, *d*, from the source.

The presence of liquid argon inside the cryostat modifies the neutron energy spectrum. This effect was explicitly studied in the simulation. For the lowest distance (9.3 cm between the neutron source and the sample), the ratio $(\mathrm{d}\varphi^{liq.argon}/\mathrm{dE})/(\mathrm{d}\varphi^{TOF}/\mathrm{dE})$ *i.e.* the energy spectrum inside the liquid argon cryostat over the energy spectrum measured by TOF is shown in Fig. 17 as a function of the neutron energy. The modification, a decrease, is most obvious in the low energy part of the spectrum.

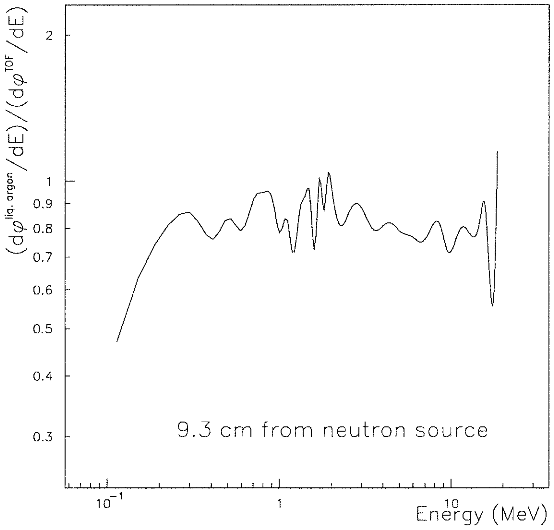

Figure 17: Variation of the ratio of neutron energy spectrum at $d = 9.3$ cm inside liquid argon cryostat over the neutron energy spectrum measured by TOF as a function of the neutron energy.

The scattered component of the neutron beam that could contribute to the main beam was also studied. The simulation was made at an angle of 10° and at different distances from the neutron source inside the liquid argon cryostat. The scattered neutron energy spectrum for a beam incident at 10° angle is shown in Fig. 18 for various distances, $d$. Its contribution is smaller than the contribution at 0° by a factor of about hundred (between 30 and 120 depending on the energy region and on the distance, $d$). The sum of the contribution of all angles weighted by their respective solid angles represent less than the direct contribution at 0°. The relative smallness of the contribution at 10° justifies the approximation made in the simulation of a beam strictly aligned along the X–axis (see geometrical modeling above).

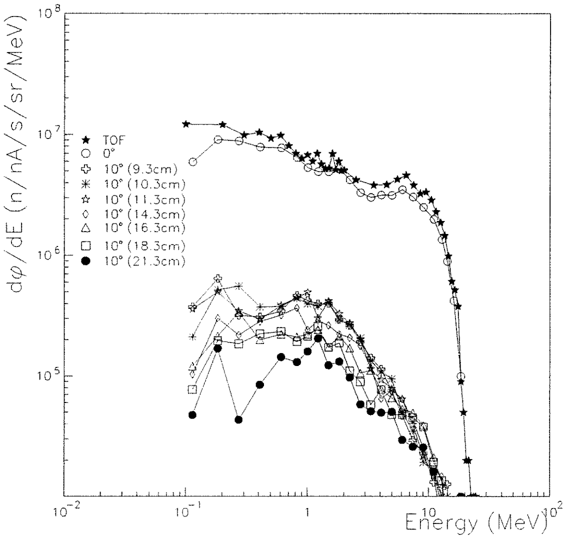

Figure 18: Scattered neutron energy spectrum for a beam incident at 10° angle inside liquid argon cryostat as a function of the neutron energy and at various distances from the neutron source. The neutron spectrum measured by TOF ($\star$) is also shown.

Finally, the effect on the neutron fluence measurement when a sample is inside the cryostat filled with air compared to filled with liquid argon was analyzed, fixing the distance, $d$, from the neutron source and the sample position. The sample size was identical in all these runs.

One defines the ratios $\Phi^{TOF}/\Phi^{in-air}$ and $\Phi^{TOF}/\Phi^{in-liq.argon}$ as the ratio of the fluence ($\Phi^{TOF}$) measured outside the cryostat over the fluence measured inside the cryostat filled with air ($\Phi^{in-air}$), and the fluence measured inside the cryostat filled with liquid argon ($\Phi^{in-liq.argon}$), respectively. One observes that:

$$\frac{\Phi^{TOF}}{\Phi^{in-liq.argon}} > \frac{\Phi^{TOF}}{\Phi^{in-air}}$$

and

$$\frac{\Phi^{TOF}}{\Phi^{in-air}} \sim 1$$

This could be expected, since in the case of air, there will be only the small effect of the cryostat's walls, and the even smaller effect from the air itself.

In summary, the simulation has permitted to establish distinctive features of the neutron field inside the liquid argon cryostat at SARA.

### 2.1.2 Dosimetric characterization of the SARA facility

The dosimetry at SARA neutron facility was performed in two steps: firstly the measurement of the angular total dose distribution using alanine dosimeters, and secondly the separation of neutron/photon doses in the radiation field using TL dosimeters.

#### The angular distribution of total absorbed dose in alanine

The measurement of the angular distribution of the total dose in the SARA field was crucial. This is because both small (for example opto–electronic devices up to 10 cm$^2$ area) and extended samples (for example printed circuits up to 100 cm$^2$ area) were irradiated in this field and it was needed to know how uniform the dose was in the irradiated material. The alanine dosimeters were the most appropriate choice due to their good reproducible responses (uncertainties less than ± 3% for high doses), and wide dose range (10 to 5 $\times 10^5$ Gy). Alanine dosimeters were calibrated with a $^{60}$Co source [33] (see appendix A).

For the measurement of the total dose angular distribution at SARA, two alanine dosimeters were fitted inside small tubes. The tubes were placed on a half-moon plexiglas support with a radius of 34.5 cm. This set-up was centered on the Be target, so that the dosimeters measured the angular distribution of the total absorbed dose in alanine from -45° to +45° (the dosimeters were covering only a quarter–of–moon).
They were irradiated during 42300 $s$ with a mean beam current of 1.02 $\mu$A on the target. After the irradiation, the absorbed doses in the alanine dosimeters were measured by means of a VARIAN-E3 ESR spectrometer (with the settings: field = 0.3295 Tesla, microwave frequency = 9.43 GHz, scanning time = 1 min, scanning range = $\pm 10^{-2}$ Tesla) at the High Level Dosimetry Laboratory at CERN.

The angular distribution of the absorbed dose–rate in alanine, is shown (circles) in Fig. 19. The distribution is smooth, and can be fitted (as shown by the continuous line) to the sum of a Gaussian (of half–width 14.5°) and a constant. The total absorbed–dose rate measured in alanine (Polymer Alanine Dosimeter) at 0° angle was 2.7±0.05 Gy/h/$\mu$A normalized at a distance of 50 cm from the Be target.

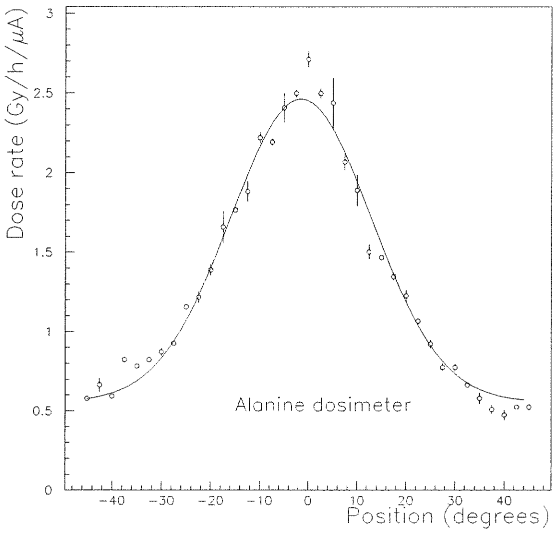

Figure 19: Angular distribution of the dose–rate in alanine normalized at a distance of 50 cm from the Be target. The line represents the result of a fit of the data (o) to a Gaussian plus a constant.

### 2.1.3 The neutron and photon doses in a mixed field

The SARA facility (as any fast neutron source) has some photon contamination. This situation of mixed field ($\gamma$ and n) is also expected inside the LHC detectors.

The total dose at SARA field includes a dose from neutrons and a dose from photons. Since photons cause much less bulk damage than neutrons, as shown by the Van Ginneken displacement damage curve [56], it is compulsory to know the fraction of the total dose due to neutrons to calculate the amount of damage per neutron dose.

Based on the author's experience with TL dosimeters, a standard method was used to identify the two components of the total dose on a mixed field. This method is based on the combined use of two types of LiF dosimeters: $^6$LiF or TLD-600 (high thermal neutron sensitivity) and $^7$LiF or TLD-700 (low neutron sensitivity and high photon sensitivity). This technique permits one to reveal the radiation field composition, in the present case, the ratio of neutron to photon dose, by a straight–forward comparison of TLD measurements [48] (appendix D). A short description of thermoluminescence dosimetry is presented in appendix A. The details of these calculations are given below.

The key factor to determine the neutron dose at SARA is to find the photon contamination. Once the photon dose was known by TLD-700 measurements, it was possible to determine the neutron dose by TLD-600 measurements.

The calibration procedure was tedious and long. Two calibration sources were used: a $^{60}$Co photon source and a Pu-Be neutron source. The dosimeters were exposed to three different calibration doses: 1, 10 and 100 mGy for photons and 0.1, 1, 10 mGy for neutrons (the neutron source was weaker). The calibration with the two sources was done using a moderator sphere (high-density polyethylene) of 12.7 cm radius. The dosimeters ($^6$LiF–$^7$LiF) were fitted in the center of the sphere.

Photons from the $^{60}$Co source were also used to perform an irradiation in free air. More details about the calibration procedure can be found in [48], which is attached to this thesis (appendix D).

After the calibration procedure, the photon sensitivities were calculated solving the equations:

$$S_\gamma^6 = \frac{R_\gamma^6}{D_\gamma^{^{60}Co}} \tag{2.1}$$

and

$$S_\gamma^7 = \frac{R_\gamma^7}{D_\gamma^{^{60}Co}} \tag{2.2}$$

where the superscripts 6 and 7 stand for the TLD-600 and TLD-700, respectively, and

$S_\gamma^6$, $S_\gamma^7$ = photon sensitivities of TLD-600 and TLD-700 embedded in moderator to $^{60}$Co gamma source (nC/mGy).
$R_\gamma^6$, $R_\gamma^7$ = dosimeter responses to $^{60}$Co gamma source (nC).
$D_\gamma^{^{60}Co}$ = photon calibration dose (mGy).

The neutron sensitivity of TLD-600 was calculated by solving the equation:

$$S_n^6 = \left(R_{\gamma'+n}^6 - S_{\gamma'}^6 D_{\gamma'}^{Pu-Be}\right)\left(D_n^{Pu-Be}\right)^{-1} \tag{2.3}$$

with the approximation:

$$S_\gamma^6 = S_{\gamma'}^6 \tag{2.4}$$

where $\gamma$ and $\gamma'$ denotes gamma rays from $^{60}$Co and Pu-Be sources, respectively, and

$S_n^6$ = neutron sensitivity of TLD-600 embedded in moderator (nC/mGy).
$R_{\gamma'+n}^6$ = TLD-600 dosimeter response to Pu-Be neutron source (nC).
$S_{\gamma'}^6$ = Pu-Be photon contamination sensitivity of TLD-600 (nC/mGy).
$D_n^{Pu-Be}$ = neutron calibration dose (mGy).
$D_{\gamma'}^{Pu-Be}$ = photon contamination calibration dose (mGy).

The solutions to the system of equations 2.1– 2.4 are shown in Table I. They are expressed as the mean value of the responses to the calibration doses (see above) of the four samples for each TLD type and each calibration dose. Only the contribution from the main dosimetric peak (peak 5, see Fig. 32) was considered in this table. The given uncertainty corresponds to a one standard deviation.

Table I: Neutron and photon sensitivities for TLD-600 and TLD-700. $S_\gamma^6$ and $S_\gamma^7$ are the photon sensitivities of TLD-600 and TLD-700, respectively. $S_n^6$ is the neutron sensitivity of TLD-600. The calibration doses were: 1, 10 and 100 mGy for photons and 0.1, 1, 10 mGy for neutrons.

| TLD | $S_\gamma^6$ (nC/mGy) | 0.9988±0.047 |
|---|---|---|
| | $S_\gamma^7$ (nC/mGy) | 0.9952± 0.007 |
| | $S_n^6$ (nC/mGy) | 23.750±0.5145 |

After the determination of sensitivities, the calibrated dosimeters could be placed in the mixed radiation field to measure its components.

### Experiment at SARA

At the irradiation facility, the center of the sphere moderator, containing the TLD pairs (4 samples of each type), was located at 50 cm from the Be target (the liquid argon cryostat was removed). The samples were irradiated during 22392 $s$, with a small deuteron beam current of 5.9 nA (to avoid saturation in the TL dosimeters).

The responses of the dosimeters located in the mixed radiation field obey the equations:

$$D_\gamma^{TLD} = \frac{R^7}{S_\gamma^7} \tag{2.5}$$

and

$$D_n^{TLD} = \left(R^6 - S_\gamma^6 D_\gamma^{TLD}\right)\left(S_n^6\right)^{-1} \tag{2.6}$$

where the superscripts 6 and 7 stand as before for TLD-600 and TLD-700, respectively. $D_\gamma^{TLD}$ and $D_n^{TLD}$ refer to gamma and neutron dose, respectively.

The gamma attenuation, the fast neutron thermalization and radiative capture effects in the sphere were considered. These effects were taken into account during the calibration process in the radiation field of $^{60}$Co and Pu-Be and also during the experiment at SARA. The details of the corrections applied can be found in [48] (appendix D).

The neutron and photon dose–rates, at a distance of 50 cm from the Be target and at an angle of 0° (*i.e.* in the beam direction), are shown in Table II.

Table II: Neutron and photon dose–rates at 0° angle and at 50 cm from the Be target.

| $\dot{D}_n^{TLD}$ (Gy/h/$\mu$A) | $\dot{D}_\gamma^{TLD}$ (Gy/h/$\mu$A) |
|---|---|
| 4.24 ± 0.19 | 1.20 ± 0.03 |

Neutron ($\dot{D}_n^{TLD}$) and photon ($\dot{D}_\gamma^{TLD}$) dose–rates were deduced, individually, from TLD measurements using equations 2.5 and 2.6.

These results show that, at 0°, neutrons and photons contributed (78 ± 2)% and (22 ± 2)% to the total dose (100 % equal to 5.44 Gy/h/$\mu$A), respectively. The error calculation presented above is updated and supersedes the values published earlier ([48](appendix D)). The correlation between the errors on neutron and photon doses have been taken into account. Correlated errors (up to 8%) are associated with machine operation (current intensity fluctuation), irradiation time (start and stop times), TL reader (small fluctuations in heating time, PM high voltage instabilities, etc) and errors during the calibration processes. These errors do not contribute to the error on the percentage. The only errors that are not correlated are the statistical errors associated with each TL dosimeter (TLD-600 and TLD-700). It was measured:

$$D_n^{TLD} + D_\gamma^{TLD} = D_{total}$$

which account for 100% of the total dose (by definition), and:

$$p_n = 0.78$$

$$p_\gamma = 0.22$$

$$78\% + 22\% = 100\%$$

Since $p_n$ and $p_\gamma$ are related in the following way,

$$p_\gamma = \frac{D_\gamma^{TLD}}{D_\gamma^{TLD} + D_n^{TLD}} = 1 - \frac{D_n^{TLD}}{D_\gamma^{TLD} + D_n^{TLD}} = 1 - p_n$$

their errors, $\Delta\, p_n$ and $\Delta\, p_\gamma$ are equal.

$\Delta\, p_n = \Delta\, p_\gamma$ was calculated via:

$$\Delta\, p_n^2 = \Delta\, p_\gamma^2 = \left(\frac{\partial\, p_\gamma}{\partial R^6}\right)^2 \Delta\,(R^6)^2 + \left(\frac{\partial\, p_\gamma}{\partial R^7}\right)^2 \Delta\,(R^7)^2 \qquad (2.7)$$

where $\Delta\, R^6$ and $\Delta\, R^7$ are the errors on $R^6$ (TLD-600 dosimeter response) and $R^7$ (TLD-700 dosimeter response), respectively.

The partial derivatives of $p_\gamma$ with respect to $R^6$ and $R^7$ are given by the Jacobian of the inverse of the matrix of sensitivities to neutron and gammas of the two dosimeter types .

The neutron fluence within one day of operation, for neutrons between 1.0–25 MeV and at 50 cm from the source, is equivalent to $8.0 \times 10^{12}$ n/cm$^2$ at maximum intensity (*i.e.* for a deuteron beam current of 5 $\mu$A) giving rise to a dose of 509.0 Gy and 144.0 Gy for neutron and photon, respectively.

### Estimate of neutron dose–rates in Si and SiO$_2$

The estimate of dose in silicon material is of great interest since silicon detectors will be used extensively in the experiments to be performed at the LHC.

The neutron dose $D_n^{Si}$ in silicon strongly depends on the neutron energy. This dose–rate expressed in Gy/h/$\mu$A is related to the flux density measured at SARA by:

$$D_n^{Si} = \int_{1.0MeV}^{25MeV} \varphi_{Sara}(E) k_{Si}(E)\, dE \tag{2.8}$$

where $k_{Si}(E)$, the neutron kerma factor for the silicon material (Gy cm$^2$/neutron), is the kerma produced in that material per unit fluence of neutrons of energy E (see appendix A). The kerma factor values have been taken from reference [57].

The neutron dose–rate in silicon calculated using equation 2.8 is equivalent to 0.36 Gy/h/$\mu$A at 50 cm from the Be target, following the 1/d$^2$–law, where d is distance of the silicon sample from the source.

The estimated neutron dose–rate in silicon dioxide at the same distance ($d$

= 50 cm) is 0.47 Gy/h/$\mu$A. The kerma factors for the compound $SiO_2$ were calculated using equation A.5 and data from reference [57] (see Appendix A for details).

The neutron dose–rates estimated above for silicon and silicon dioxide (0.36 and 0.47 Gy/h/$\mu$A) are equivalent to the doses of 43.2 Gy and 56.4 Gy for one day of machine operation with a total fluence of $8.0 \times 10^{12}$ n/cm$^2$ at full intensity (5 $\mu$A of the deuteron beam) and at 50 cm from the neutron source.

In our previous publication [48] (appendix D), we estimated that the neutron doses in Si and $SiO_2$ would be 12.5 ± 2.5 times smaller than the neutron dose measured with TL dosimeters (*i.e.* 0.34 Gy/h/$\mu$A) – for the SARA mean neutron energy of 6 MeV. Within the errors, the present estimate of the neutron dose of 0.36 Gy/h/$\mu$A, agrees with our previous estimate.

## 2.2 Charged particle facilities

The hadronic component of the radiation (neutrons, protons, pions, etc...) produces most of the bulk damage in the silicon diodes to be used in the ATLAS detector. The evaluation of the damage further depends on the hadron energy, though, for relativistic charged hadrons, energy loss and damage change little with energy, as shown by the Van Ginneken and Huhtinen displacement damage curves [56, 58]. In the LHC experiments, close to the collision point, pions will be responsible for producing most of the bulk damage, together with other particles such as neutrons and protons. Farther away from the collision point, as the outgoing hadronic showers develop, the relative importance of protons and neutrons increases [58]. Because proton-proton collisions at LHC will produce a considerable number of pions, some (low energy pions) resulting from $\Delta$ resonances decay, it is important to study the radiation hardness of detector components exposed to low energy pions. For this reason, a pion beam ($\pi$E1) with momentum $p$ = 350 MeV/c at the Paul Scherrer Institute (PSI-Villigen) [59] was used to perform irradiations of silicon detectors. The problem of proton irradiations was addressed using a proton beam (ZT7) with momentum $p$ = 24 GeV/c at the Proton Synchrotron (PS) at CERN.

When pion and proton beams interact with the silicon samples and materials nearby, different kinds of particles, such as neutrons, protons, photons can be generated. These secondary particles can contribute additional damage to the silicon samples under study. The best way to quantify this contribution is to measure it, during the irradiation of silicon samples.

In order to perform the dosimetric measurements close to the beam (out-of-beam), the author designed an experimental set–up usable at both facilities (pion and proton). This experimental set-up includes dosimeters (alanine and LiF) and activation foils (In, Co and Ni) to measure the absorbed doses and particle fluences near the pion and proton beams [60, 61]. The dosimeters and activation foils were placed along the perpendicular axis (Y- and Z axis), in alternate positions.

The main pion and proton fluxes were measured by nuclear activation of aluminium foils and carbon slabs (the choice is explained below).

The measurements of particle fluences and doses near the hadron beams were performed to allow the study of the correlation between the fluences and doses and the damage inflicted to silicon detectors. This damage is directly monitored by changes in the electric characteristics of silicon detectors with fluence.

### 2.2.1 PSI-$\pi$E1 pion irradiation facility

Recent simulations of hadron fluxes in the LHC detectors [62] show the presence of high pion flux densities with energies between 0.1 -1 GeV. An estimate of the pion damage for energies above 1 GeV is presented in [56]. At these energies (above 1 GeV) the cross–sections are practically constant. At lower energies ($\sim$ 200 MeV), the damage induced by pions in silicon could be enhanced due to the production of $\Delta$ resonances, which lead to a larger $\pi$-nucleus total cross section [58]. Thus, this energy range is of particular interest for the physicists trying to understand the behavior of silicon detectors under pion dominated irradiations.

For this purpose, the Paul Scherrer Institute was chosen, since its facility provides access to a pion beam. This high intensity beam of pions ($\sim 10^8$ $\pi^+/\text{cm}^2/\text{s}$) was used to study the radiation damage effects in silicon detectors. In the framework of the dosimetric characterization of this facility, we have measured particle fluences (in- and out–of–beam) and doses, as this section will describe.

Complementary work done by the author that has not been published in any article is also presented. This work includes details of the estimate of pion absorbed doses in alanine and silicon materials, using the concept of the minimum ionizing energy loss rate. It also includes details of the corrections applied in neutron nuclear reactions due to possible proton contribution and the details of the calculations of the neutron and proton fluxes out-of-beam.

### $\pi$E1 beam line

The $\pi$E1 beam line at PSI supplies pions and muons with high intensity. Pions are produced in the collision of the intense proton beam (maximum current 800 $\mu$A) with a graphite target (12×10 mm FWHM). Beam optics permit the selection of pions with momenta ranging from 100 to 450 MeV/c. These pions are guided (via a beam line) down to an irradiation casemate. Graphite plate absorbers are placed at the end of the beam, in order to eliminate the presence of protons. The protons are stopped in carbon, some of them interacting with carbon and producing neutrons of low energy.

Table III: Graphite absorbers during $\pi$E1-PSI runs. The underlined pion momentum and graphite absorbers thickness were used in the present work.

| $P_{\pi^+}$ (MeV/c) | Proton mean free path (g/cm$^2$) | Graphite absorbers (g/cm$^2$) |
|---|---|---|
| 150 | 0.2 | 1.01 |
| 200 | 0.6 | 1.01 |
| 250 | 1.2 | 1.78 |
| 300 | 2.2 | 2.79 |
| $\underline{350}$ | $\underline{4.0}$ | $\underline{4.57}$ |
| 400 | 6.0 | 7.12 |
| 450 | 9.0 | 10.15 |

Table III shows the proton mean free path in graphite at the corresponding pion momentum and the density of the graphite plate absorbers used during the experiments.

The irradiation position was located 1 m downstream of the last quadrupole magnet (at a height of 1.5 m), see Fig. 20.

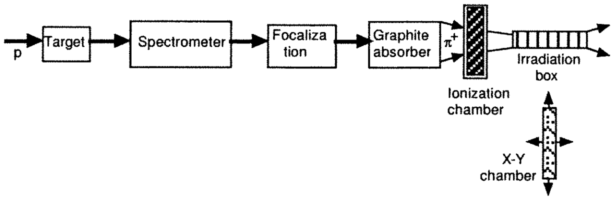

Figure 20: Diagram of the pion beam and irradiation set-up at $\pi$E1-PSI.

The silicon samples under study were mounted inside square cardboard frames. The silicon detectors were $\sim$ 9 k$\Omega$cm n–type ion–implanted single diodes with a thickness of $\sim$ 300 $\mu$m and an area of 5 $\times$ 5 mm$^2$, similar in resistivity and thickness to the silicon detectors that will be used in the LHC experiments (tracking regions), due to their high charge collection efficiency, and fast response. A fast response is needed due to the short time interval (every 25 ns) between two consecutive LHC bunches and to catch the created short–lived particles [63].

The frames containing the silicon samples were stacked, normal to the beam direction, in a box volume of 5$\times$5$\times$25 cm$^3$. The box was located on a table mobile along the X-,Y-, and Z-axes in order to optimize its position in the beam.

At the same time, aluminium foils cut to the same shape as the silicon samples were interleaved with the tested material. The measurement of their activation provided a way to evaluate the pion flux densities at the irradiation positions, as will be shown in the following subsections.

### Selection of pion momenta

Several runs (results reported in [31], attached as appendix E) at different pion momenta were made in order to select a single momentum, in the $\Delta$ resonance region, where the facility provides high flux densities. The maximum flux density was obtained in the region of 300–350 MeV/c (see Fig. 4 in [31], appendix E). The momentum of 350 MeV/c was thus selected to obtain a high beam intensity and to ensure that the corresponding kinetic energy was within the range of the $\Delta$ resonance. The pion kinetic energy corresponding to a momentum of 350 MeV/c is 237.23 MeV, as obtained from the relation:

$$K_{\pi^+} = \sqrt{p^2 + m_{\pi^+}^2} - m_{\pi^+}$$

where $p$ and $m_{\pi^+}$ are the $\pi^+$ momentum and mass, respectively.

### $\pi^+$ beam profile at 350 MeV/c

The pion beam was monitored by a system including an ionization chamber (two parallel plates), an X-Y wire chamber and a luminescent screen. The X-Y chamber was used to measure the transverse beam profile (*h*orizontal (Y–axis) and *v*ertical (Z–axis) FWHM). The transverse beam density, expressed as $[(\mathrm{FWHM})_h.(\mathrm{FWHM})_v]^{-1}$, was calculated at each position because it was necessary to determine the size and shape of the beam at each irradiation position. The transverse beam profile and transverse beam density are shown in Fig.2 of appendix E.

The average pion flux density measured by Al foils is shown in Fig. 21, as a function of the position along the irradiation box. As a comparison, the transverse beam density ($[(\mathrm{FWHM})_h.(\mathrm{FWHM})_v]^{-1}$) obtained from the X–Y profile chamber is also shown. The flux density strongly decreases from the front to the back of the box. Both measurements were in reasonably good agreement (see Fig. 21).

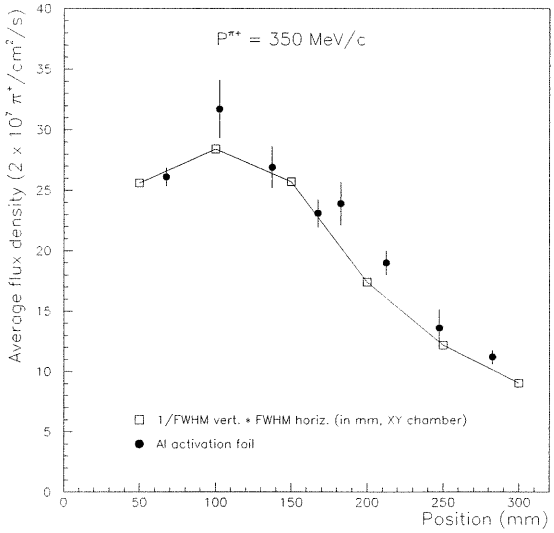

Figure 21: Comparison of the transverse beam density at a momentum of 350 MeV/c as obtained by the X–Y chamber (☐) and by the Al activation measurements (●) at $\pi$E1-PSI.

## Dosimetric characterization of the $\pi$E1 beam at PSI

This dosimetric characterization involves two steps: firstly, the measurement of pion flux density and dose in the beam (in-beam), and secondly, the measurements of particle flux density and dose close to the $\pi^+$ beam (out-of-beam).

## Pion flux density and pion dose measurements (in-beam)

### *Pion flux density measurements*

The activation of aluminium foils via the $^{27}Al(\pi^+,xN)^{24}Na$ reaction allowed the measurement of the pion flux densities. The Al activation method was selected due to several advantages: the cross section associated with this nuclear reaction is well known in the working energy range; the half-life (15 h) of the created isotope, $^{24}$Na, leaves enough time to perform the gamma activity measurements. The isotope has two gamma emissions of 1.368 MeV and 2.754 MeV. The soft Al metal has a high degree of purity (99.95 %) and can be cut in a convenient size.

Carbon slabs (using the $^{12}$C($\pi^+$,xN)$^{11}$C reaction) were used to provide a cross–check of the pion flux densities given by Al foils. $^{11}$C is a positron emitter with energy of 0.98 MeV and has a half-life of 20.4 min; this short half-life restricts the numbers of samples than can be employed in a given irradiation. It also means that a rapid transit for the slabs has to be arranged, between the location of irradiation and the location of measurement. $^{11}$C short half-life is a difficulty, but the technique has the advantage that it is sensitive to all hadrons with energies above 20 MeV.

The activity from $^{11}$C can be measured using a gamma spectrometer, counting the number of 0.511 MeV photons produced by positron–electron annihilation.

The pion activation results obtained with Al foils and C slabs were in agreement within 5 %.

The activities were measured at the PSI with a high purity Ge(p)–$\gamma$ spectrometer. The gamma spectra was analyzed by the INTERGAMMA code (the same code used at CERN for this kind of measurement), giving the activity. The saturation activities and, the corresponding particle fluence densities were calculated using equation 1.21 and equation 1.23 (see chapter 1).

Four Al runs were performed during the $\pi^+$ accumulation at a momentum of 350 MeV/c. For each run, Al foils of the same area were located in front of each group of silicon detectors. The pion flux density in each of the four runs as a function of each group of irradiated silicon detectors is shown in Fig. 22. Various pion runs (accumulation runs) were performed, until the accumulated fluence from the runs was in excess of $10^{14}$ $\pi^+/\text{cm}^2$.

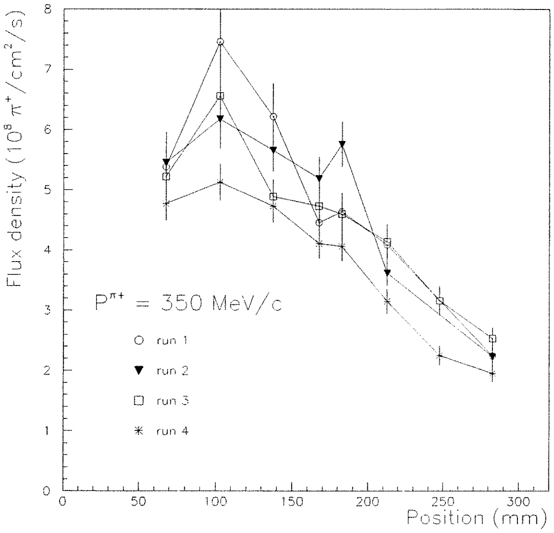

Figure 22: The pion flux density at $\pi$E1-PSI measured by Al activation foils during the four runs as a function of the longitudinal position in the irradiation box.

The Al runs were also used to calibrate the ionization chamber. The calibration factor, $c_j$, for the ionization chamber was obtained fitting the experimental points (Al fluence measurements versus ionization chamber counts) at a given position in the irradiation box.

Then, the calibration factors can be used to calculate the fluence, $\Phi$, at any position during the accumulation runs, using the relation:

$$c_j = \frac{\Phi_j}{N_{ic}} \Rightarrow \Phi_j = c_j N_{ic} \tag{2.9}$$

where $j$ denotes the longitudinal position of the silicon detectors in the irradiation box, $\Phi_j$ is the fluence received by each Al activation foil at the position $j$, and $N_{ic}$ is the number of counts from the ionization chamber.
In Fig. 23 are shown the pion average flux densities measured by Al activation foils and the estimated pion dose-rates in silicon along the irradiation box.

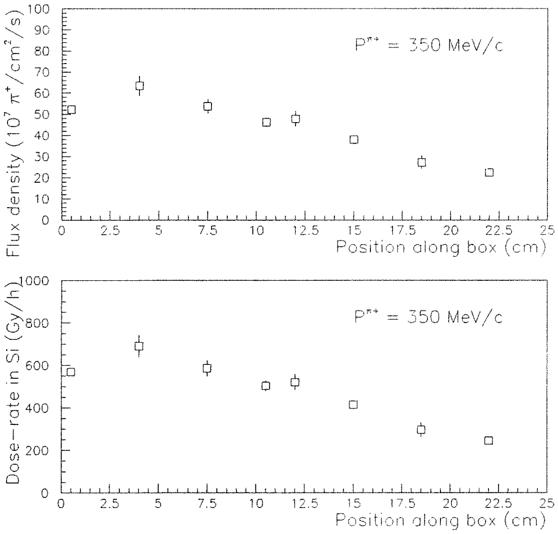

Figure 23: Pion average flux densities and pion average dose–rates in silicon as a function of the position along the irradiation box.

*Pion dose measurements in alanine*

Polymer alanine dosimeters (PAD) were placed in the rear of the box in order to measure the pion doses in alanine in the beam line. Alanine was chosen because it can be used in high level radiation environments, and has a linear dose response over a wide dose range (from 50 Gy to 30 kGy).

The alanine dosimeters were measured using Electron Spin Resonance technique (see appendix A), giving the pion dose in alanine. The measured mean value of the pion dose-rate in alanine is equivalent to (337.0 ± 7.2) Gy/h.

The estimated pion dose-rate (theoretical value), given the known pion flux (considering the pions as minimum ionizing particles [64]), is equal to (262.0 ± 13.6) Gy/h. The estimate was obtained as follows. First the estimate of the minimum ionizing energy loss rate, $(dE/dx)_{min}$ was done, taking into account the atomic weight A and atomic number Z of the material being traversed, in this case alanine (see appendix A).

$$\left(\frac{dE}{dx}\right)_{min} = 3.76\, Z/A \qquad MeV\, cm^2\, g^{-1} \tag{2.10}$$

with Z=48 and A=89 for alanine ($CH_3$-$CHNH_2$-$COOH$), which gives a minimum ionizing energy loss rate $\left(\frac{dE}{dx}\right)_{min}$ equivalent to 2.03 MeV cm$^2$ g$^{-1}$. Secondly, the conversion factor fluence–to–dose, CF, is:

$$CF = \frac{2.03\, MeV cm^2 g^{-1} \;\times\; 1\mu Gy\, h^{-1}}{1.73\, MeV g^{-1} s^{-1}} = 1.17\, \frac{\mu Gy\, h^{-1}}{cm^{-2} s^{-1}}$$

The theoretical pion dose–rate in alanine is then:

$$D^{alanine}_{\pi^+} = \left((22.4 \,\pm\, 1.16) \times 10^7\, \pi^+/cm^2/s\right) \times \left(1.17\, \frac{\mu Gy\, h^{-1}}{cm^{-2} s^{-1}}\right)$$

$$D^{alanine}_{\pi^+} = (262.0 \pm 13.6)\, Gy/h$$

where $(22.4 \pm 1.16) \times 10^7$ $\pi^+/\text{cm}^2/\text{s}$ is the corresponding pion flux density at the irradiation position (22.5 cm in the irradiation box).

The fact that the measured pion dose–rates in alanine are larger than the estimated dose–rates can be explained by the presence in the beam and around it of other types of particles (neutrons, electrons and photons) that contribute to the dose–rate.

*Estimate of the pion dose in silicon*

The same procedure was applied to estimate the theoretical pion dose-rate in silicon. At the focal point of the beam optics (3.5 cm in the irradiation box), where the pion flux density is maximal, the corresponding pion dose–rate in silicon is found to be (691.1 ± 52.3) Gy/h.

The estimated pion dose–rate in silicon dioxide ($SiO_2$) is the same as in silicon. This is because the ratios Z/A are equal (14/28 for Si and 30/60 for $SiO_2$).

### The particle flux density and dosimetric measurements close to the $\pi^+$ beam (out-of-beam).

The results for this section were reported in [60], which is attached to this thesis (appendix F).

In order to measure the neutron contamination close to the beam, Indium (In), Cobalt (Co) and Nickel (Ni) activation foils of 6 mm diameter were placed at different positions along the Y– and Z– axes (X–axis is the pion beam axis). The activation foils positions are shown in Fig. 24. As we explained in [60] (appendix F), In activation foils were chosen, because they present interesting nuclear reactions for thermal and medium neutron energies, with very large and well–known neutron cross–sections. An important component of the contamination spectrum will be measured with these reactions. Ni and Co activation foils present large cross-sections for neutron nuclear reactions at medium and high neutron energies. The associated cross sections can be found in the literature. These measurements will complete the understanding of the spectrum of neutrons responsible for contamination.

In order to quantify the proton contamination close to the beam, the same Ni and Co activation foils (6 mm diameter) were used. These foils can react with protons of medium and high energies. The positions of the activation foils are shown in Fig. 24.

Chips of LiF:Mg,Ti (TLD-700) were used to measure the photon dose near the beam, at positions shown in Fig. 24. These dosimeters have ~ 99.99 % of $^7$LiF and ~ 0.01 % of $^6$LiF in their composition, giving high photon sensitivity and negligible neutron sensitivity.

### *Neutron flux density measurements near the $\pi^+$ beam*

The irradiation of the In, Co and Ni activation foils was performed simultaneously with a group of Si samples at the pion facility during 28920 s. At the end of the irradiation, the photon emission of each activation foil was measured with a high purity Ge(p)-$\gamma$ spectrometer. Using the INTERGAMMA code, the gamma spectra were analyzed, identifying each peak of the spectra with a decaying nucleus.

A total of 4 radionuclei coming from neutrons were identified out-of-beam at $\pi$E1: two nuclei from In ($^{116}$In$^m$, $^{115}$In$^m$), one nucleus from Ni ($^{57}$Ni), and one nucleus from Co ($^{57}$Co) (see Table IV).

It must be said that among these 4 nuclei created, only $^{116}$In is coming

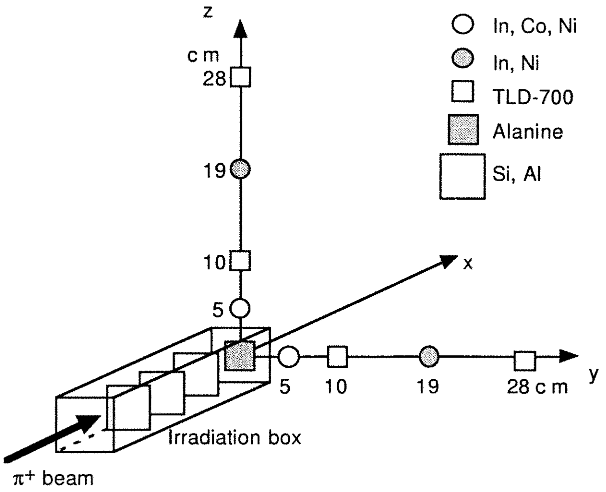

Figure 24: Diagram of the irradiation box and the activation foils and dosimeters positions at $\pi$E1 pion beam at PSI.

from an exclusive neutron reaction. $^{115}$In$^m$ could come from inelastic scattering with either neutrons or protons. Analyzing both cross sections for these reactions, the effective threshold energy [1] can be calculated and found to be 0.5 MeV for the neutron reaction and around 1000.0 MeV for the proton reaction [66]. For the $^{57}$Ni nucleus, the threshold energy is 12.6 MeV and 15.0 MeV for the neutron and proton reaction, respectively. For $^{57}$Co, this threshold is 20.4 MeV for neutrons and 35.0 MeV for protons. Considering that the quantity of low energy neutrons in the stray field around accelerators is larger than the quantity of protons [67, 68], and also taking into account the threshold effective energy of each nuclear reaction, it is assumed that $^{115}$In$^m$ is coming only from neutrons. In the case of the two last neutron

---

[1] The effective threshold energy, is defined [65] as the energy at which the cross–section is 1/100 of its peak value.

Table IV: Neutron reactions at different positions near the $\pi$E1 pion beam at PSI.

| Position (cm) | Nuclear reaction | Effective threshold energy (MeV) | Half-life of product | Energy of gamma ray (MeV) |
|---|---|---|---|---|
| **PSI** | | | | |
| 5y, 5z, 19y, 19z | $^{115}$In(n,$\gamma$)$^{116}$In$^m$ | thermal | 54.0 min | 0.417, 1.097, 1.29 |
| 5y, 5z, 19y, 19z | $^{115}$In(n,n')$^{115}$In$^m$ | 0.5 | 4.5 h | 0.336 |
| 5y, 5z, 19z | $^{58}$Ni(n,2n)$^{57}$Ni | 12.6 | 36.0 h | 0.51, 1.37 |
| 5y | $^{59}$Co(n,3n)$^{57}$Co | 20.4 | 271.7 d | 0.122, 0.136 |

nuclear reactions (on the $^{57}$Ni and $^{57}$Co nuclei) shown in Table IV, a correction for a possible proton contribution in the neutron reaction is applied (as described below), because the difference between proton and neutron effective energy thresholds is small. At relatively high energies (beyond 50 MeV) the neutron–nucleus cross sections ($\sigma_{nN}$) are slightly smaller than the proton–nucleus cross sections ($\sigma_{pN}$) [69]:

$$\sigma_{nN} = \sigma_{pN}/1.07 \tag{2.11}$$

The total activities of the created nuclei $^{57}$Ni and $^{57}$Co are:

$$\overline{Act}_{Total} = \overline{Act}_{nN} + \overline{Act}_{pN} \tag{2.12}$$

where:

$\overline{Act}_{nN}$ = Activity coming from neutron–nucleus interaction.

$\overline{Act}_{pN}$ = Activity coming from proton–nucleus interaction.

Then, from equation 1.18 (see chapter 1):

$$\overline{Act}_{Total} = S\sigma_{nN}\varphi_{nN} + S\sigma_{pN}\varphi_{pN} \tag{2.13}$$

where:

$$S = \frac{N_a\, P\, W\,(1 - e^{-\lambda\, t_c})(1 - e^{-\lambda\, t_i})}{\lambda\, e^{\lambda\, t_e}\, A\, t_c}$$

Thus, introducing equation 2.11 in equation 2.13 and assuming that $\varphi_p \leq \varphi_n$, the corrected neutron flux density, $\varphi_n^{corrected}$, can be obtained as:

$$\varphi_n^{corrected} \geq \frac{1}{2.07}\left(\frac{\overline{Act}_{Total}}{S\sigma_{nN}}\right) \tag{2.14}$$

As a first approximation, the neutron flux densities were estimated considering the cross sections associated with the most probable neutron energy ($\bar{E_n}$) at which the neutron nuclear reactions are enabled. In other words, through the following equation one calculates the effective neutron energy:

$$\bar{E_n} = \frac{\int_{E_{min}}^{E_{max}} \exp\left(-E/kT\right)\sigma\, E\, dE}{\int_{E_{min}}^{E_{max}} \exp\left(-E/kT\right)\sigma\, dE} \tag{2.15}$$

where:

$E$ = Neutron energy in MeV.

$k$ = Boltzmann constant.

$T$ = Characteristic "temperature" of typical evaporation reactions.

$kT$ = 200 MeV.

$\sigma$ = Neutron cross section in mb.

The estimated neutron flux densities are shown in Fig. 25. The cross sections were taken from reference [70].

Analyzing Fig. 25, the estimated flux densities of low energy neutrons at both distances (5 cm and 19 cm) in both axes were almost independent of the distance from the pion beam. Their values were spread between 1.5 and $2.0 \times 10^6$ n/cm$^2$/s. The estimated flux densities of medium energy neutrons were decreasing with the distance from the pion beam, and were generally decreasing with increasing neutron threshold energies.

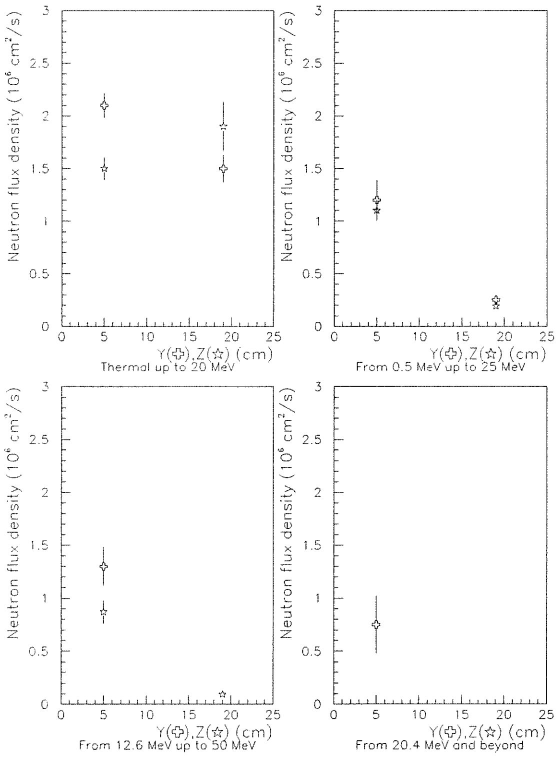

Thermal up to 20 MeV

From 0.5 MeV up to 25 MeV

From 12.6 MeV up to 50 MeV

From 20.4 MeV and beyond

Figure 25: Estimated neutron flux densities near $\pi$E1-PSI pion beam as a function of neutron energy and as a function of the distance from the pion beam.

The errors ($\Delta\varphi$) of these fluxes is varying between 6% to 27% at 5 cm and between 16% to 19% at 19 cm. The errors ($\Delta\varphi$) were calculated by taking into account the errors associated to the measured activities (between 5 and 30 %) and the measured weights of the foils (between 1.3 and 2.8 %). The errors associated with the cross sections were not taken into account, because they were not available explicitly. However, they are less than 5 %, typically. The error on the activity is the dominant one. $\Delta\varphi$ was calculated via:

$$\frac{\Delta\varphi}{\varphi} = \left[\left(\frac{\Delta Act_{sat}}{Act_{sat}}\right)^2 + \left(\frac{\Delta W}{W}\right)^2\right]^{1/2} \tag{2.16}$$

where:

$Act_{sat}$ = The saturation activity of the foil.
$W$ = The weight of the foil.
$\varphi$ = The measured flux density.

The estimated number of neutrons created per incident pion as a function of the neutron mean energy of the nuclear reaction are shown in Fig. 26.

*Proton flux density measurements close to the $\pi^+$ beam*

The analysis of the nuclear reactions found at 5 cm from the pion beam led to the following conclusion: three of them were corresponding to proton nuclear reactions. The nuclei produced were: $^{52}$Mn from Cobalt, $^{55}$Co and $^{52}$Mn from Nickel (see Table V). As seen above (estimate of neutron flux densities), the proton flux densities were estimated considering the cross sections associated with the effective proton energy, using a calculation similar to equation 2.15. The proton cross sections were taken from [66]. The errors on the activities were ranging from 2.4 up to 30 %, those on the weight were around 1 %. At

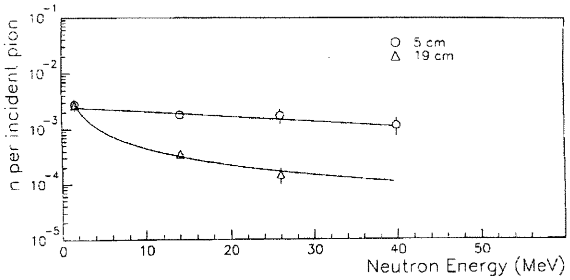

Figure 26: Estimated number of neutrons per $\pi^+$ at 5 cm (○) and at 19 cm (△) from the $\pi$E1 pion beam as a function of the neutron mean energy. At 5 cm, the line represents the results of a fit of the data to an exponential. At 19 cm, the curve is a fit to $C/E_n$, where $C$ is a fitted constant and $E_n$ is the neutron energy.

5 cm, the ratios of the estimated proton flux densities ($p$) to the maximum incident pion flux density ($\pi_{in}$) were: (0.00861 ± 0.00325) $p/\pi_{in}$ above 7.8 MeV up to 164.0 MeV, and (0.00158 ± 0.00089) $p/\pi_{in}$ above 40.0 MeV up to 370.0 MeV.

*Photon dose measurements close to the* $\pi^+$ *beam*

The thermoluminescent dosimeters were read with a Harshaw 2000 TLD reader coupled to a Harshaw TLD glow-curve analyzer model 2080. It was set to give a linear heating rate of 7°C/s from room temperature (about 20°C) to 280°C. The glow curve low temperature peaks were erased by a pre–readout annealing at 85°C during 25 min.

The photon doses were calculated using a $^{60}$Co calibration curve. The measured average photon dose–rates were (5.0 ± 0.8) Gy/h and (0.74 ±

Table V: Proton reactions at different positions near the $\pi$E1 pion beam at PSI.

| Position (cm) | Nuclear reaction | Effective threshold energy (MeV) | Half-life of product | Energy of gamma ray (MeV) |
|---|---|---|---|---|
| **PSI** | | | | |
| 5y, | $^{59}$Co(p,3p5n)$^{52}$Mn | 40.0 | 5.59 d | 1.43, 0.935, 0.744 |
| 5y, 5z | $^{58}$Ni(p,$\alpha$)$^{55}$Co | 7.8 | 17.5 h | 0.931, 0.477 |
| 5z | $^{58}$Ni(p,4p3n)$^{52}$Mn | 37.0 | 5.59 d | 1.43, 0.935, 0.744 |

0.03) Gy/h at 10 cm and 28 cm from the pion beam, respectively. The photon dose–rate close (10 cm) to the pion beam was 6 times larger than the measured dose–rate at the second position (28 cm).

### 2.2.2 ZT7-PS proton irradiation facility

The presence of damaging protons among other hadrons in the complex radiation field created after the p–p collision in the LHC detectors will be significant, hence the importance of performing proton radiation damage studies. This section presents the dosimetric characterization we have performed at a proton facility located at the Proton Synchrotron (PS) at CERN using the ZT7 beam line (high intensity primary beam), with 24 GeV/c protons. This proton beam was used to study the radiation hardness of silicon detectors.

Estimate of proton doses in alanine and silicon materials are also presented. These results have not been published previously.

### The ZT7 proton beam line

The ZT7 beam area is offering high proton intensities. It is located upstream of the beam T7. As mentioned above, ZT7 offers a primary proton beam with a momentum of 24 GeV/c, with either one or two spills (400 ms) of protons delivered to the irradiation zone per supercycle. Two consecutive spills are separated by at least 2.4 s during a 14.4 s supercycle. The irradiation position was located about 3 m downstream of the vacuum pipe. The maximum proton intensity was $2\times10^{11}$ protons per spill.

Similarly to the experiment done at PSI (see section 2.2.1), an ionization chamber (two parallel plates), a X-Y wire chamber and a luminescent screen were installed in order to monitor the proton beam, and a box of $5\times5\times25$ cm$^3$ of volume was placed normal to the beam direction, containing silicon samples and interleaved aluminium foils, all of them mounted in square cardboard frames. The aluminium foils were used to calculate the proton fluences by measuring the gamma (1.368 MeV) activity from the created isotope ($^{24}$Na).

Silicon single diodes of n– and p–type with an area of 1 cm$^2$ and thickness between 100 and 300 $\mu$m were irradiated.

Also, alanine dosimeters [33] were placed at the end of the box to measure the proton absorbed doses in alanine in the beam line. In order to optimize the box position in the beam, it was mounted on a table mobile along the three space axes.

### Dosimetric characterization of the ZT7 proton beam

The dosimetric characterization of the ZT7 proton beam (24 GeV/c) at PS involves two steps: first, the proton beam measurements (in-beam), and secondly the particle flux density measurements close to the proton beam (out-of-beam).

### Proton beam measurements (in-beam)

*Proton flux density measurements*

The proton fluences were measured by activation of Al foils by proton through the nuclear reaction

$$^{27}Al \ + \ p \Rightarrow \ 3pn \ + \ ^{24}Na.$$

The activation of graphite slabs via the nuclear reaction

$$^{12}C \ + \ p \ \Rightarrow \ pn \ + \ ^{11}C,$$

was used as a cross–check of the proton fluences given by the Al foils. $^{24}$Na decay emitting two gammas and $^{11}$C decay by a positron emission. The activities from the isotopes created $^{24}$Na and $^{11}$C were measured by a gamma spectrometer, as it was explained in the section devoted to the measurements at PSI section. The cross sections for these nuclear reactions in Al and C were taken from [66]. The results obtained with Al and C foils were in agreement within 5 %. The proton flux density was measured by activation of Al foils. The proton flux density was equivalent to $(2.7 \pm 0.15) \times 10^9$ p/cm$^2$/s.

*Estimate of the proton dose in silicon*

Using the above proton flux, one can estimate the proton dose–rate in silicon. The estimate of proton dose-rate in silicon was $(3.0 \pm 0.16)$ kGy/h (the same procedure as in section 2.2.1). The conversion factor, CF, from fluence-to-dose is equivalent to CF= 1.09 $\mu$ Gy h$^{-1}$/cm$^{-2}$ s$^{-1}$.

The estimated proton dose–rate in silicon dioxide ($SiO_2$) is the same as in silicon. This is because the ratios Z/A are equal (14/28 for Si and 30/60 for $SiO_2$).

*Proton dose in alanine*

The experimental proton dose-rates in alanine were measured again through Electron Spin Resonance technique. The measured proton dose–rate in alanine is (3.4 ± 0.08) kGy/h.

The estimated proton dose–rate in alanine is equal to (3.2 ± 0.18) kGy/h. Both results, the measured (experimental) and the estimated (theoretical) proton dose–rates in alanine, show very good agreement.

### Particle flux measurements close to the proton beam (out-of-beam)

In order to measure the contamination of hadrons (especially neutrons and protons) close to the proton beam, Indium (In), Cobalt (Co) and Nickel (Ni) activation foils were placed at different distances from the proton beam (X-axis) along the Y- and Z- axes.

All three activation foils can react with neutrons, but Ni and Co also have exclusive proton reactions. The positions are shown in Fig. 27.

The irradiation of the activation foils was performed simultaneously with a group of silicon samples. The irradiation time was 7440 s. After irradiation, the same procedure described in section 2.2.1 to measure the induced activity in the foils was applied.

*Neutron flux density measurements close to the proton beam (out-of-beam)*

At this facility, seven neutron nuclear reactions were identified. The created radionuclei were: $^{116}In^{m}$ and $^{115}In^{m}$ from In activation foil, $^{57}Co$, $^{58}Co$ and $^{56}Mn$ from Co activation foil, $^{57}Ni$ and $^{58}Co$ from Ni activation foil.

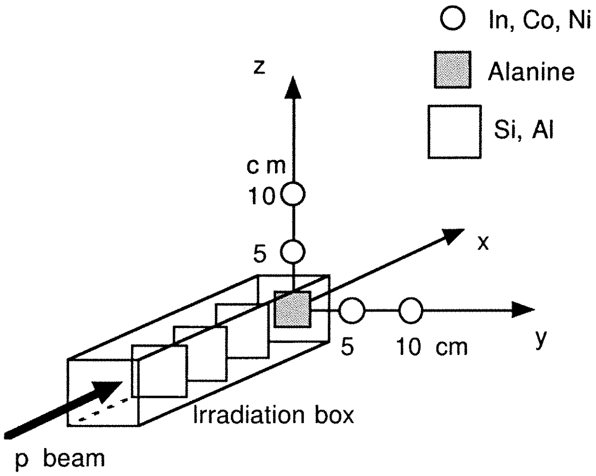

Figure 27: Set-up of the experiment at the ZT7 proton beam line at PS.

These neutron nuclear reactions are shown in Table VI with the corresponding positions of the foils on the Y-axis and Z-axis, together with their approximate effective threshold energy, half-life of the nuclei and energy of the emitted gamma rays.

Similarly to the section 2.2.1, a correction for a possible proton contribution must be applied in the case of the isotopes $^{57}Co$ and $^{58}Co$ from Cobalt and in the case of the isotope $^{57}Ni$ from Nickel. The effective neutron threshold energy is 20.4 MeV for $^{57}Co$, 10.3 MeV for $^{58}Co$ and 12.6 MeV for $^{57}Ni$. The effective proton threshold energy is 35.0 MeV for $^{57}Co$, 15.0 MeV for $^{58}Co$ and $^{57}Ni$. The total activities of these isotopes ($^{57}Co$, $^{58}Co$ and $^{57}Ni$) were calculated in the same way as done in the section 2.2.1, via equation 2.12. Then, the corrected neutron flux density can be obtained using equation 2.14.

Table VI: Neutron reactions at different positions near the ZT7 proton beam at PS.

| Position (cm) | Nuclear reaction | Effective threshold energy (MeV) | Half-life of product | Energy of gamma ray (MeV) |
|---|---|---|---|---|
| **PS** | | | | |
| 5y, 5z, 10y, 10z | $^{115}$In(n,$\gamma$)$^{116}$In$^m$ | thermal | 54.0 min | 0.417, 1.097, 1.29 |
| 5y, 5z, 10z | $^{115}$In(n,n')$^{115}$In$^m$ | 0.5 | 4.5 h | 0.336 |
| 5y, 5z, 10y, 10z | $^{58}$Ni(n,2n)$^{57}$Ni | 12.6 | 36.0 h | 0.51, 1.37 |
| 5y, 5z | $^{58}$Ni(n,p)$^{58}$Co | 1.3 | 71.3 d | 0.51, 0.81 |
| 5y, 5z, 10y, 10z | $^{59}$Co(n,3n)$^{57}$Co | 20.4 | 271.7 d | 0.122, 0.136 |
| 5y, 5z, 10y, 10z | $^{59}$Co(n,2n)$^{58}$Co | 10.3 | 71.3 d | 0.51, 0.81 |
| 5y, 5z | $^{59}$Co(n,$\alpha$)$^{56}$Mn | 5.2 | 2.58 h | 0.85 |

The estimated neutron flux densities are shown in Fig. 28. The cross sections were taken from [70].

The neutron flux densities were estimated calculating the effective neutron energy. The estimated neutron flux densities of four of the seven nuclear reactions found at ZT7-PS are shown in Fig. 28. As it was the case at $\pi$E1-PSI, the dominant component of the neutron spectra were low energy neutrons. This component was almost independent of the distance from the proton beam. The values of the estimated neutron flux densities were decreasing from the first (5 cm from the proton beam) to the second irradiation position (10 cm from the proton beam). At 5 cm, the errors of estimated neutron flux densities were varying between 11% and 35% (depending on the energy), and at 10 cm they were between 5% and 12%.

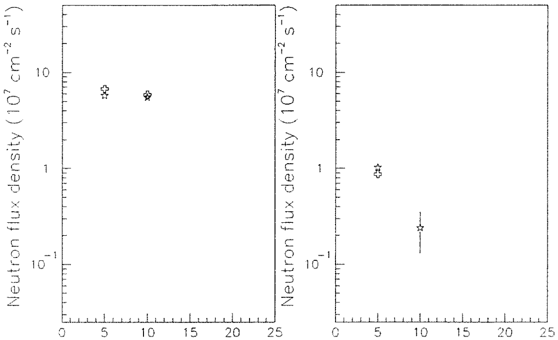

Thermal up to 20 MeV

From 0.5 MeV up to 25 MeV

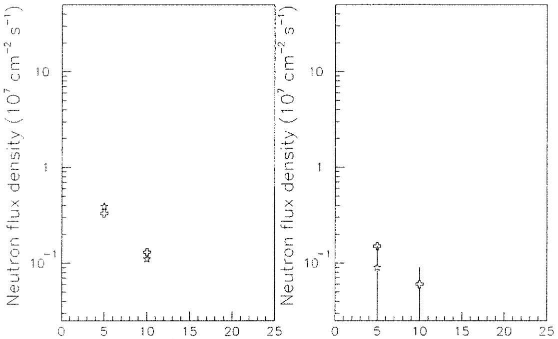

From 12.6 MeV up to 50 MeV

From 20.4 MeV and beyond

Figure 28: Estimated neutron fluxes near the proton beam at ZT7-PS as a function of the neutron energy and as a function of the distance from the proton beam.

The errors related to the estimated neutron flux densities were obtained by considering the errors associated to the activities (5 to 30%) and weights (1.3 to 2.8 %) of the foils. The error on the activity is dominant.

The estimated number of neutrons per incident proton as a function of the neutron mean energy are shown in Fig. 29.
At 5 cm from the proton beam, the amount of neutrons created per incident proton was decreasing with the neutron energy. At 10 cm, the amount of neutrons created per incident proton was also decreasing with neutron energy, but more sharply at low neutron energy (2 – 14 MeV).

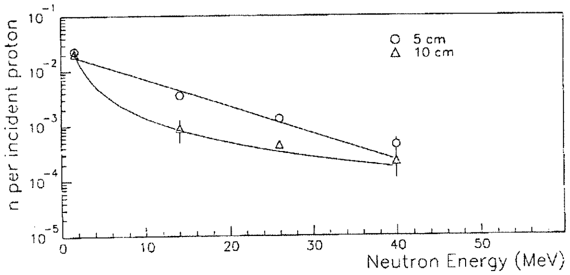

Figure 29: Estimated number of neutrons produced per incident proton at ZT7-PS, at 5 cm (○) and at 10 cm (△) from the proton beam as a function of the neutron mean energy. At 5 cm, the line represents the results of a fit of the data to an exponential. At 10 cm, the curve is a fit to $C_{1.5}/E_n^{1.5}$, where $C_{1.5}$ is a fitted constant and $E_n$ is the neutron energy

*Proton flux density measurements close to the proton beam*
Four proton nuclear reactions were found out of the beam at this facility. The radionuclei produced were: $^{52}$Mn and $^{48}$V from Co activation, $^{55}$Co and $^{52}$Mn from Ni activation. The proton nuclear reactions are shown in Table VII.

The proton cross sections were taken from [66].

The ratios of proton (out-of-beam) per incident proton (in–beam), were

Table VII: Proton reactions at different positions near the ZT7 proton beam at PS.

| Position (cm) | Nuclear reaction | Effective threshold energy (MeV) | Half-life of product | Energy of gamma ray (MeV) |
|---|---|---|---|---|
| **PS** | | | | |
| 5y, 5z, | $^{59}$Co(p,3p5n)$^{52}$Mn | 40.0 | 5.59 d | 1.43, 0.935, 0.744 |
| 5y, 5z | $^{59}$Co(p,5p7n)$^{48}$V | 70.0 | 16.1 d | 0.5, 0.98, 1.3 |
| 5y, 5z | $^{58}$Ni(p,$\alpha$)$^{55}$Co | 7.8 | 17.5 h | 0.931, 0.477 |
| 5y, 5z | $^{58}$Ni(p,4p3n)$^{52}$Mn | 37.0 | 5.59 d | 1.43, 0.935, 0.744 |

estimated considering a proton flux density equivalent to (2.7 ± 0.15) × $10^9$ p/cm$^2$/s and the mean value of the fluxes of created proton measured at the same distance from the proton beam (for example, at 5y and 5z). Below is an example of these calculations in the case of positions 5y and 5z:

$$\varphi_p(proton\,beam) \;=\; (2.7 \pm 0.15)\;\times\;10^9\,p\,/cm^2/s \tag{2.17}$$

$$\varphi_p(5y) \;=\; (2.88 \pm 0.1)\;\times\;10^7\,p\,/cm^2/s \tag{2.18}$$

$$\varphi_p(5z) \;=\; (2.97 \pm 0.08)\;\times\;10^7\,p\,/cm^2/s \tag{2.19}$$

Taking the average of the proton fluxes at the positions 5y and 5z, the resulting value must be divided by $(2.7 \pm 0.15)\;\times\;10^9\,p\,/cm^2/s$, and it gives (0.01080 ± 0.00023) proton per incident proton ($p/p_{inc}$).

The ratio of the observed proton (out-of-beam) flux density to the proton (in–beam) flux density given to the silicon samples at 5 cm are: (0.01080 ± 0.00023) $p/p_{inc}$ above 7.8 MeV up to 164.0 MeV, (0.00612 ± 0.00131) $p/p_{inc}$ above 40.0 MeV and up to 370.0 MeV, and (0.01370 ± 0.00212) $p/p_{inc}$ from 70.0 MeV to 370.0 MeV.

The estimated proton flux densities are decreasing with the proton threshold energy, but the dominant contamination proton component is above 70 MeV. The activation nuclear reactions used for these measurements were exclusively proton reactions. They are listed in Table VII.

As it was the case for the estimated neutron flux density, the errors associated with the proton flux density were calculated by taking into account the errors associated to the activities (15 to 40 %) and weights (1.3 to 2.8 %) of the foils. The error on the activity is again the dominant error.

## 2.3 Results and conclusions: hadron facilities

The experimental part of this work has been performed during several years, starting with the dosimetric characterization of the SARA facility, followed by the measurements at PSI and PS facilities. The experiments in all the facilities, including the contamination measurements around the main beams, are original and have been designed and largely performed by the author. Many details in the measurements and estimates have not been published previously in any article.

The main results for the hadron facilities are:

### 2.3.1 Neutron facility

The SARA neutron irradiation facility offers the possibility to carry out neutron irradiation studies at both cryogenic and room temperatures. At the same time the user can measure on–line the deterioration of the electronic performance of the tested circuits. The dosimetric measurements allows one to study the evolution of the damage with the absorbed dose (or fluence). Another important purpose of this facility is to study the pollution of the liquid argon under fast neutron irradiation due to the outgassing of materials inside the cryostat [11, 12].

The FLUKA Monte–Carlo code allowed to estimate the neutron energy spectrum inside the liquid argon cryostat. At the position of 10.3 cm from the neutron source (2.15 cm in liquid argon), the total attenuation of the neutron fluence inside the liquid argon cryostat was found equivalent to 22 % of the neutron fluence measured by TOF technique.

In the dosimetric characterization performed at SARA facility, the alanine dosimeters allowed the measurements of the angular total dose distribution from -45° to +45°. The total dose–rate at 0° and at 50 cm from the Be target was $2.7 \pm 0.05$ Gy/h/$\mu$A. It was found to be reasonably flat inside a cone of $\simeq 10°$.

The combination of $^6$LiF (TLD-600) and $^7$LiF (TLD-700) dosimeters proved to be an effective method to separate neutron and photon doses in a mixed field such as the SARA field. The experiment performed at SARA using a polyethylene moderator with a pair of TL dosimeters fitted inside was proposed and done by the author, as well as the experiment to measure the dose distribution by alanine dosimeters, the Monte–Carlo simulation and the estimate of doses in Si and $SiO_2$.

A dosimetric characterization of the SARA facility shows that neutron and gamma components of the mixed radiation field give rise to (78 ± 2)% and (22 ± 2)% of the LiF total dose, respectively. The photon contamination of the field at SARA was found equivalent to 1.20 Gy/h/$\mu$A dose–rate and 4.24 Gy/h/$\mu$A for the neutron dose–rate, for a normalized neutron flux density of $6.67 \times 10^{10}$ n/cm$^2$/h/$\mu$A at a distance of 50 cm from the neutron source.

At the same distance from the neutron source, the estimated neutron absorbed dose–rate in silicon was equal to 0.36 Gy/h/$\mu$A and 0.47 Gy/h/$\mu$A for silicon dioxide.

### 2.3.2 Pion facility

The high fluence pion beam of the Paul Scherrer Institute (PSI) at Villigen, was used to irradiate hundreds of silicon detectors of different types. The $\pi$E1 beam line at PSI was set up specifically for silicon irradiation studies. The results of the silicon irradiation studies can be found elsewhere [71].

The dosimetric measurements can be summarized as follows: the maximum pion flux density measured by aluminium activation at the focal point of the beam optics (3.5 cm in the irradiation box) was $(6.34 \pm 0.48) \times 10^8$ $\pi^+$/cm$^2$/s. The cyclotron proton intensity was $\sim$ 750 $\mu$A and the pion momentum was 350 MeV/c.

At the same position (3.5 cm in the irradiation box), the corresponding estimated pion dose-rate in silicon and silicon dioxide was (691.1 ± 52.3) Gy/h.

The experimental measured dose–rate (22.5 cm in the irradiation box) from alanine dosimeter was (337.0 ± 7.2) Gy/h. This was in reasonable agreement with the estimate of the theoretical dose-rate in alanine of (262.0

± 13.6) Gy/h, considering the possible contribution of secondary particles to the measured dose–rate in alanine. The dose–rate in silicon was (244.2 ± 12.6) Gy/h at the same irradiation position as the alanine (22.5 cm in the irradiation box).

The neutron and proton contamination flux densities were few percents of the main pion flux density. At 5 cm from the pion beam, the ratio of neutrons per incident pion shows a smooth decrease with increasing neutron energy (consistent with an exponential shape). At 19 cm, the ratio of neutrons per incident pion seems to behave approximately as the inverse of the neutron energy ($1/E_n$) (where $E_n$ is the neutron energy). At this distance the low neutron energy component dominates.

In the case of the proton contamination, the protons were found only at 5 cm from the pion beam and the estimated flux densities were decreasing as a function of the proton energy; *i.e.* at low energy there are high contamination proton fluxes and at higher energies there are low contamination proton fluxes.

The average contamination photon dose–rates measured were (5.0± 0.8) Gy/h and (0.74 ± 0.03) Gy/h at 10 cm and 28 cm from the pion beam, respectively.

Despite several complex phenomena that tend to complicate the relationship between the actual dose and the flux of pions coming from the beam, a simple relationship between measured doses and doses calculated from the particle flux density has been established for the PSI facility as a result of the author's work; furthermore, there is evidence that flux densities from proton and neutron contamination close to the pion beam remain within acceptable small limits.

### 2.3.3 Proton facility

The proton flux density measured by the aluminium activation technique was found equivalent to (2.7 ± 0.15) × $10^9$ p/cm$^2$/ s at the focal point of the beam optics. The corresponding proton dose–rate estimated in silicon and silicon dioxide was found to be (3.0 ± 0.16) kGy/h, using the concept of minimum ionizing energy loss rate.

The measured proton dose–rate (experimental) in alanine was (3.4 ± 0.08) kGy/h and the corresponding estimated proton dose–rate (theoretical) was (3.2 ± 0.18) kGy/h. These values show good agreement between the experimental and theoretical results.

The contamination of neutrons and protons close to the beam (out-of-beam), were also a few percents of the proton flux density. At this facility, at 5 cm from the proton beam the neutron contamination decreased slowly with the neutron energy. At 10 cm, the neutron contamination component followed a law $1/E_n^{1.5}$ (where $E_n$ is the neutron energy).

This result is not far from an estimate done at stray fields in high–energy proton accelerators, where the tail of high energy neutrons varies approximately as $1/E_n^{1.7}$ [68]. The low energy component was found dominating.

Evidence of created protons was found only at 5 cm from the proton beam. The dominant contamination proton energy is above 70 MeV.

The radiation damage results for the silicon samples irradiated simultaneously with the foils and dosimeters used in this work can be found elsewhere [72].

The main conclusion of this chapter is the importance of the dosimetric characterization of the irradiation facilities as part of any LHC radiation damage program. The accuracy of the measurements of the particle fluences or doses are relevant when one needs to correlate these measurements with the inflicted damage to the detector components and electronics under study. When someone studies bulk damage effects in silicon, he must know the exact number of particle per square centimeter, that interact with the irradiated material. In other studies, such as studies of surface damage effects in $SiO_2$ or GaAs, the exact measurement of the absorbed dose is crucial.

# Chapter 3

# Non-Ionizing Energy Loss (NIEL) and hardness factor

The dosimetric characterization of the hadron irradiation facilities: SARA facility for neutrons, $\pi$E1-PSI facility for pions and ZT7-PS facility for protons, was presented in the chapter 2. An important part of the research program at these facilities was the study of silicon detectors under irradiation. The radiation effects in silicon mater~~ials~~ depend on the particle type and on the particle energy. In order to compare the radiation damage results obtained with different types of particles at various energies, it is useful to renormalize the particle fluence of a specific irradiation to the equivalent fluence of 1 MeV neutrons. This renormalization is done through the Non Ionizing Energy Loss hypothesis, which is based on the assumption that the variation in the induced displacement damage in a material scales linearly with the amount of energy imparted in displacing collisions.

The NIEL hypothesis applies to bulk damage, while surface damage effects are not thought to obey NIEL scaling.

This chapter briefly describes the NIEL scaling hypothesis and its application to the calculation of the **equivalent fluence of 1 MeV neutrons** and the hardness factor at the SARA, $\pi$E1-PSI and ZT7-PS hadron irradiation facilities. These results and estimates have not been published in any of the attached publications (appendices C,D,E,F).

## 3.1 Non-Ionizing Energy Loss (NIEL) and hardness factor

The main cause of bulk damage (or displacement damage) in silicon is due to **N**on-**I**onizing **E**nergy **L**oss (NIEL) interactions with atoms. The silicon atoms are being knocked–out of their lattice positions and in the case of high-energy hadrons (e.g. neutrons or protons), they can also interact producing silicon nuclear reactions where the reaction products move through the lattice interacting with other atoms, knocking them also out of their lattice locations. Light particles, such as electrons and photons, also produce displacement damage in silicon, but the electrons and photons cross–sections are much lower.

Therefore, instead of quoting NIEL, one frequently talks about displacement damage cross–section or displacement kerma factor ($DK(E)$).

The NIEL value of silicon is usually given in [keV cm$^2$/g] and for silicon (A= 28.086 g/mol) the relation between $DK(E)$ and NIEL is: 100 MeV mb = 2.087 keV cm$^2$/g [73].

Using the displacement kerma factor ($DK(E)$), it is possible to define the equivalent fluence of 1 MeV neutrons ($\Phi_{eq}^{1MeV}$) which produces the same damage as any particle beam with a specific energy distribution and fluence ($\Phi_{meas.}$).

The **equivalent fluence of 1 MeV neutrons** is defined by:

$$\Phi_{eq}^{1MeV} = \kappa\, \Phi_{meas.} \tag{3.1}$$

where $\Phi_{meas.}$ is the measured fluence of the particle beam equal to:

$$\Phi_{meas.} = \int_{E_{min}}^{E_{max}} \varphi(E)\, dE$$

$\varphi$ is the particle flux density.

$\kappa$ is the hardness factor defined as:

$$\kappa = \frac{1}{DK(1MeV)} \frac{\int_{E_{min}}^{E_{max}} \varphi(E)\, DK(E)\, dE}{\int_{E_{min}}^{E_{max}} \varphi(E)\, dE} \tag{3.2}$$

where $DK(1MeV)$ is the normalization factor equal to (95 ± 4) MeV mb, value recommended by the American Society for Testing and Materials (ASTM) [74], and $DK(E)$ is the displacement kerma factor. $DK(1MeV)$ is an average value of neutron displacement kerma factor near 1 MeV. This value is difficult to determine because of sharp neutron cross section resonances in that energy region. However, Namenson et al. have calculated this factor using various tabulations of $DK(E)$ versus energy [75].

The silicon displacement kerma factor ($DK(E)$) at energy, $E$, is given by [76]:

$$DK(E) = \sum_k \sigma_k(E) \int dE_R\, f_k(E, E_R)\, P(E_R) \tag{3.3}$$

where the sum is over all the reactions between the silicon and the incident particle, $\sigma_k$ is the corresponding cross section of these reactions, $f_k(E, E_R)$ is the probability that a particle with energy, $E$, produces a recoil with energy, $E_R$, through the reaction $k$, and $P(E_R)$ is the partition function derived by Lindhard [77]. The Lindhard function has been calculated in the LSS (Lindhard screened potential scattering) theory. Lindhard has studied the process of partitioning the energy of a recoil nucleus between electrons (electronic excitation or ionization) and elastic and inelastic collision that could produce displacement atoms from their lattice sites (non–ionizing displacements). This quantity ($DK(E)$) has been calculated for the interaction of various types of particles as neutrons, pions, protons and photons with silicon and as a function of particle energy [56, 74, 76, 78, 79, 62, 58, 80].

## 3.2 "Equivalent fluence of 1 MeV neutrons" for: SARA, $\pi$E1-PSI and ZT7-PS

### 3.2.1 SARA neutron facility

To calculate the "equivalent fluence of 1 MeV neutrons" for the SARA neutron facility, first the hardness factor $\kappa$ was estimated using the neutron displacement kerma factors (DK(E)) in silicon from references [56, 74, 76, 78]. A lower and upper bound of integration of 100 keV and 25 MeV were considered in equation 3.2, respectively.
The estimates of SARA hardness factor are shown in Table VIII.

The calculations of the hardness factors of the SARA facility, using silicon displacement kerma factors from different authors, show small discrepancies between them, of the order of 8% (see Table VIII). If one takes the mean value of the hardness factors, one finds $\kappa = 1.53 \pm 0.13$.

Table VIII: $\kappa$ hardness factor for the SARA neutron facility.

| Neutron Facility | $E_{min}$ (MeV) | $E_{max}$ (MeV) | $\int_{E_{min}}^{E_{max}} \varphi(E)dE$ $\times 10^{10}$ (n/cm$^2$/h/$\mu$A) | $\overline{E}$ (MeV) | $\kappa$ | Displacement kerma factors |
|---|---|---|---|---|---|---|
| SARA | 0.100 | 25.0 | 8.00 | 6.0 | 1.66 | [56] |
| | 0.100 | 25.0 | 8.00 | 6.0 | 1.62 | [74] |
| | 0.100 | 25.0 | 8.00 | 6.0 | 1.42 | [76] |
| | 0.100 | 25.0 | 8.00 | 6.0 | 1.43 | [78] |

Then, the **"equivalent fluence of 1 MeV neutrons"** per year for the SARA facility at the maximum beam intensity (5$\mu$A) and at 50 cm from the Be source is:

$$\Phi_{eq}^{1MeV} = 0.17 \times 10^{16} \quad (n_{eq}/cm^2)$$

The LHC annual running time has been taken equivalent to $10^7$ s (115 days) for the estimate of the equivalent fluence of 1 MeV neutrons.

### 3.2.2 $\pi$E1-PSI pion facility

The "equivalent fluence of 1 MeV neutrons" and the $\kappa$ hardness factor for the $\pi$E1-PSI facility are shown in Table IX.
In the case of $\pi$E1-PSI, the estimate of the hardness factor was done using the displacement kerma factors from references [56, 58, 80].

As can be seen in Table IX, the equivalent fluence of 1 MeV neutrons for the $\pi$E1-PSI facility depends on the reference value for the silicon displacement kerma factors used for the hardness factor estimates. The value

Table IX: The equivalent fluence of 1 MeV neutrons ($\Phi_{eq}^{1MeV}$) per year for the $\pi$E1-PSI pion facility, and the $\kappa$ hardness factor.

| Facility | Particle | Spectrum | Energy (MeV) | $\kappa$ | Displacement kerma factors | $\Phi_{eq}^{1MeV}$ $\times 10^{16}$ ($n_{eq}/cm^2$) |
|---|---|---|---|---|---|---|
| PSI | $\pi^+$ | monoener. | 237.2 | 0.71 | [56] | 0.45 |
| | $\pi^+$ | monoener. | 237.2 | 0.91 | [58] | 0.58 |
| | $\pi^+$ | monoener. | 237.2 | 1.54 | [80] | 0.98 |

of the $\kappa$ factor is larger than one (1.54) only in one case, when Lazanu *et al.* calculations were utilized. In the other two cases, the values of $\kappa$ are smaller than unity (0.71 and 0.91), but differing in between them by 22%. If one takes a mean value of these two last values, the hardness factor will be 0.81 ± 0.14 and the corresponding equivalent fluence of 1 MeV neutrons per year will be:

$$\Phi_{eq}^{1MeV} = 0.51 \times 10^{16} \quad (n_{eq}/cm^2)$$

The pion flux density is equal to $6.34 \times 10^8$ pion/cm$^2$/s.

### 3.2.3 ZT7-PS proton facility

The estimate of hardness factor $\kappa$ for this facility was done using the displacement kerma factors DK(E) at the energy of 9 GeV from reference [62], because there exists no DK(E) value for the 24 GeV/c protons. The estimated hardness factor is $\kappa = 0.51$.

The proton displacement kerma factors DK(E) in silicon has been also calculated by other authors [56, 79]. The experimental damage results for protons are in better agreement with Huhtinen *et. al.* calculations. This is not the case with the tabulations by Van Ginneken [56], which have been proven to be wrong at high energies (above 100 MeV) [81]. Then, it is recommended to use Huhtinen's proton displacement kerma factors [82].

If one takes a hardness factor $\kappa = 0.51$, the **"equivalent fluence of 1 MeV neutrons"** per year for the ZT7-PS facility is:

$$\Phi_{eq}^{1MeV} = 1.42 \times 10^{16} \quad (n_{eq}/cm^2)$$

A proton flux density equal to $2.79 \times 10^9$ p/cm$^2$/s has been taken. In the literature, previous estimates of $\kappa$ were 0.93 [83] and 1.19 [84]. These values were overestimated.

## 3.3 Conclusions

The **"equivalent fluence of 1 MeV neutrons"** for SARA, $\pi$E1-PSI and ZT7-PS hadron facilities were calculated. All of the **"equivalent fluence of 1 MeV neutrons"** are of the order of $10^{15}$–$10^{16}$ equivalent neutrons ($n_{eq}$) per cm$^2$ (similar to the fluence accumulated during ten years of LHC running).

The hardness factor $\kappa$ was estimated for all hadron facilities. The discrepancies between the various values of the hardness factor $\kappa$ are mainly due to the energy cuts in the particle spectrum, and to the displacement kerma factors utilized. The hardness factor relates the NIEL of a particular particle to that of a 1 MeV neutron which has a displacement kerma factor of 95 MeV mb.

# Chapter 4

# Conclusions

The main result of this thesis is the dosimetric characterization of hadron facilities that can be used as reference for work in radiation damage studies for LHC detectors. Using the present measurements of the particle fluences and doses, the physicists can correlate quantitatively fluence or dose measurements with the damage being observed in irradiated materials and equipment. Three hadron facilities have been characterized: SARA for neutrons, $\pi$E1-PSI for pions, and ZT7-PS for protons. Each facility provides accelerated damage testing for specific LHC detector components: SARA makes available high neutron fluences and a cryostat filled with liquid argon to test the radiation hardness of liquid argon calorimeters parts and electronics under cold conditions. It was important to know the relative contributions of photons and neutrons at this facility, because the neutrons produce more significant bulk damage than photons, creating cluster and point defects in the silicon materials. $\pi$E1-PSI provides high pion fluences in silicon detectors around the delta resonance zone, a crucial energy region where the induced damage on silicon could be enhanced; ZT7-PS allows the study of the radi-

ation hardness of silicon detectors exposed to high-energy protons.
In the case of $\pi$E1-PSI and ZT7-PS facilities, it was important to measure the contamination around the pion and proton beams (out–of–beam), because this contamination could contribute additional damage to the silicon detectors under study.

Regarding the evaluation of the radiation hardness of the detectors in preparation for LHC operation, the most important result from this thesis is the confirmation that the hadron facilities deliver fluences and doses dominated by the intended particle type, and the contamination out–of–beam is not significant. The use of irradiation set–ups similar to these utilized in the present work for future irradiation hardness studies of samples at these facilities will certainly lead to meaningful results. This, we believe, is a non-negligible contribution of the present work.

At $\pi$E1-PSI and ZT7-PS, the daily fluence was $5.5 \times 10^{13}$ pions per $cm^2$, and $2.4 \times 10^{14}$ protons per $cm^2$, respectively. At SARA the daily fluence inside the liquid argon cryostat was $1.48 \times 10^{14}$ neutrons per $cm^2$, corresponding to the fluence of about 10 years of LHC operation, as far as the sensitive ATLAS electronics is concerned.

Another important result of this thesis was to show that the dose at SARA was dominated by the neutron dose (78%n, 22%$\gamma$). Depending on the Z of the material, the relative doses will vary somewhat, but it is fundamental to know that the neutron dose dominates when designing an irradiation set-up, or while analyzing results. In the $\pi$E1-PSI and ZT7-PS facilities, the beam was narrow and the contamination changed in character from a broad spectrum of energy and particle types at 5 cm from the beam to a steeply falling energy distribution of neutrons (1/E) at 10 cm from the beam and beyond. However, these small contaminations of neutrons and protons remain within acceptable small limits.

At the $\pi$E1-PSI, neutrons were present representing a fraction of 0.2 – 0.8 % of the pion beam (thermal and above 500 keV) and protons representing a fraction of 0.1 – 0.8 % of the pion beam (energy above 7.8 MeV). At the ZT7-PS, neutrons were representing a fraction between 0.1 – 2.3 % (thermal and above 500 keV) and between 0.6 – 1.4 % (energy above 7.8 MeV) of the proton beam, respectively. Again, these results will guide the designers of future irradiation experiments to take the appropriate precautions to deal with beam contamination.

The particle fluence measurements at the charged hadron facilities and the particle contamination measurements around the irradiation beams were done by the activation technique. This is a reliable technique. It can be used over a wide range of fluences, and is insensitive to the pulsed structure of accelerator fields. The activity of the foils can be measured at convenience after the experiment (considering both the half–life of the nucleus (or nuclei) created and the activity of the foil).

Direct measurements of absorbed doses in the main beam of the hadron facilities were performed with alanine dosimeters. They present a linear response over a wide range of doses (50 Gy to $30 \times 10^3$ Gy), good time stability of the induced free radicals, availability of a non–destructive read–out technique, accuracy, repeatability and reproducibility of measurements.

Alanine dosimeters can be recommended to measure absorbed doses at charged hadron facilities and it can be used to measure total dose distribution, as for example in the stray fields in the LHC tunnel.
Thermoluminescent dosimeters (TLD) were used to measure the photon absorbed doses around the beams, and the combination of two different kinds of TLD fitted inside a moderator polyethylene sphere, allowed to separate the neutron and photon components in the case of mixed fields. The moderator sphere method proved to be an effective method to separate the neutron from the photon component in a mixed field. These dosimeters also present small size, easy handling and good accuracy in their responses.

Ultimately, it is the radiation damage inflicted to the detector components, electronics and equipment which constitutes a major preoccupation for the LHC physicists in their ambitious plan to discover the mechanism of the origin of mass after operating the LHC detectors for several years.
For the ATLAS experiment, silicon is part of the detection systems and of the read electronics and therefore deserves particular attention.
The expected bulk damage in silicon, dominantly caused by neutrons and charged hadrons, does scale with the non–ionizing energy loss and is therefore characterized in terms of equivalent fluence of 1 MeV neutrons. Therefore, the "equivalent fluence of 1 MeV neutrons" using the NIEL scaling hypothesis, and the correct hardness factor for each facility were estimated in chapter 3. Signal loss as a consequence of the liquid argon pollution is another preoccupation for the ATLAS experiment. After 10 years of LHC operation, without any replacement or any purification of the liquid argon, the total calorimeter signal loss is expected to be lower than 1.5 %.

The hadron facilities presented in this thesis were used during many years. Thanks to the dosimetric characterization of these facilities, and others around the world, the radiation damage research programmes of the different R&D groups are ongoing, trying to cover their main objectives: predict the radiation damage in the detector components, electronics and equipment for LHC applications, and improve the radiation hardness especially of the detector components.

# Bibliography

[1] The LHC study group, *Design Study of the Large Hadron Collider (LHC), A Multiparticle Collider in the LEP Tunnel*, CERN 91–03, 1991.

[2] **ATLAS** Collaboration, *Letter of Intent for a General–Purpose pp Experiment at the Large Hadron Collider at CERN*, CERN/LHCC/92–4, LHHC/I2, 1992.

[3] **ATLAS** Collaboration, *Technical Proposal for a General–Purpose pp Experiment at the Large Hadron Collider at CERN*, CERN/LHCC/94–43, LHCC/P2, 1994.

[4] **CMS** Collaboration, *The Compact Muon Solenoid*, Letter of Intent, CERN/LHCC/92-3, LHCC/I1, 1992.

[5] **CMS** Collaboration, *CMS: The Muon Project Technical Design Report*, CERN-LHCC-97-32, CMS-TDR-3, 1997.

[6] **ALICE** Collaboration, *ALICE Technical Proposal for a Large Ion Colliders Experiment at the CERN-LHC*, CERN LHCC 95-71, LHCC/P3, 1995.

[7] **LHC-B**: *Letter of Intent: A Dedicated LHC Collider Beauty Experiment for Precision Measurements of CP–Violation*, CERN-LHCC-95-5, LHCC-I-8, 1995.

[8] K. M. Potter, M. Höfert and G. R. Stevenson, *Radiation Protection at the Large Hadron Collider, LHC* CERN/TIS-RP/96-04/CF, 1996.

[9] C. Leroy, S. Pospíšil, I. Štekl, and J. Sodomka, *Remarks on a Concept of the ATLAS Forward Region Shielding*, ATLAS Internal Note, TECH-No 032, 1998.

[10] ATLAS LARG Unit, *Technical Design Report Liquid Argon Calorimeter*, CERN/LHCC/96-141, ATLAS TDR 2, 1996.

[11] Ph. Martin, *Pollution of Liquid Argon due to Neutron Irradiation*, ATLAS Internal Note, LARG-052, 1996.

[12] J. Collot, Ph. Martin and A. Belymam, *Signal Loss Extrapolation from Pollution Measurements done at SARA using an Alpha Cell to the Case of the Barrel EM calorimeter*, ATLAS Internal Note, LARG-056, 1996.

[13] L. R. Evans, *The Large Hadron Collider*, Report CERN AC/95-02 (LHC) LHC Note 320, 1995.

[14] M. Höfert and G. R. Stevenson, *Potential Exposures at High–Energy Proton Storage Rings*, CERN/TIS-RP/95-13 CF, 1995.

[15] G. R. Stevenson, A. Fassò and J. M. Zazuela, *The Estimation of Parameters of Radiological Interest for the LHC Main Ring*, CERN/TIS-RP/IR/9208, 1992.

[16] J. E. Gover and J. R. Srour, *Basic Radiation Effects in Nuclear Power Electronics Technology*, Sandia Labs Report SAND85-0776, 1985.

[17] T. P. Ma and P. Dressendorfer, *Ionizing Radiation Effects in MOS Devices and Circuits*, J.Wiley, 1988.

[18] V. A. J. Van Lint et al., *Mechanisms of Radiation Effects in Electronics Materials*, Vol. 1, Wiley–Interscience, New York, 1980.

[19] V. A. J. Van Lint, Nuclear Instrum. and Meth. **A 253**, p.453, 1987.

[20] W. R. Dawes Jr., Nuclear Instrum. and Meth. **A 288**, p.54, 1990.

[21] G. Hall, IC/HEP/90/8, 1990.

[22] H. W. Kraner, Nuclear Instrum. and Meth. **225**, p.615, 1984.

[23] E. Heijne, CERN Yellow Report 83-06, 1983.

[24] E. Borchi, M. Bruzzi and M. S. Mazzoni, London Conference on Position Sensitive Detectors, 1990.

[25] G. Lindström et al., DESY Report 90-109, 1990.

[26] E. Heijne, CERN-PPE 88-061, 1988.

[27] E. León Florián, C. Leroy and C. Furetta, *Particle Fluence Measurements by Activation Technique for Radiation Damage Studies*, CERN-ECP 95-15, 1995.

[28] M. Tavlet and E. León Florián, *PSAIF: The PS-Acol Irradiation Facility at CERN.* Proceedings of the First European Conference on Radiation and its Effects on Devices and Systems, La Grande-Motte, France, 9–12 Sep, 1991, IEEE Catalog Number 91TH0400-2, 582, 1992.

[29] M. Edwards and D. R. Perry, *The Radiation Hardness Test Facility*, Rutherford Laboratory Internal Report RAL-90-065, 1990.

[30] J. Collot, P. De Saintignon, P. Gabor, A. Hoummada, G. Mahout, D. Marchand, F. Merchez, E. León Florián, C. Leroy, Ph. Jean and B. Merkel, *A Neutron Irradiation Facility Featuring Cryogenic Temperatures and Dedicated to Large Hadron Collider Detector Design*, Nucl. Instr. and Methods **A350**, p.525, 1994.

[31] C. Furetta, S.J. Bates, M. Glaser, F. Lemeilleur, M. Tavlet, E. León Florián, C. Leroy and RD2 Collaboration, *Fluence and Dosimetric Measurements for a* $\pi^{\pm}$ *Irradiation Facility*, CERN-ECP/95-2, 1995. Proceedings of the 4th International Conference on Advanced Technology and Particle Physics, Como, Italy, 3–7 Oct. 1994, Nucl. Phys. B **44**, p.503, 1995.

[32] St. Charalambus, J. Dutrannois and K. Goebel, *Particle Flux Measurements with Activation Detectors*, CERN/DI/HP 90, 1966.

[33] E. León Florián, H. Schönbacher and M. Tavlet, *Data Compilation of Dosimetry Methods and Radiation Sources for Material Testing*, CERN/TIS-CFM/IR/93-03, 1993.

E. León Florián, H. Schönbacher and M. Tavlet, *Facilities and Dosimetry for Detector Material Irradiations*, CERN-LAA/RA/92-006, 1992.

[34] D. F. Jackson, *Nuclear Reactions*, Methuen & Co Ltd, London, 1970.

[35] K. Kikuchi and M. Kawai, *Nuclear Matter and Nuclear Reactions*, North-Holland Publishing Company, Amsterdam, 1968.

[36] B. Cohen, *Concepts of Nuclear Physics*, McGraw-Hill Book Company, 1971.

[37] M. Barbier, *Induced Radioactivity*, North-Holland Publishing Company, Amsterdam, 1969.

[38] K. Debertin and R. G. Helmer, *Gamma and X-Ray Spectrometry with Semiconductor Detectors*, ISBN: 0 444 871071, North-Holland, 1988.

[39] Adams and Dams, *Applied Gamma–Ray Spectrometry*, Pergamon Press, 1970.

[40] Intertechnique Intrumentation Nucleaire, INTERGAMMA software package, Version 5.10N.

[41] C. Leroy, private communication.

[42] G. Hall, *Prospects for Silicon Detectors in the 1990s*, IC/HEP/90/2, 1990.

[43] E. Fretwurst, Nuclear Instrum. and Meth. **A288**, p.1, 1990.

[44] R. Wunstorf *et. al.*, Nuclear Physics B (Proc. Suppl.) **23A**, p.324, 1991.

[45] Université Joseph–Fourier CNRS–IN2P3, ISN *SARA Experimental Facilities.*

[46] J. Collot, P. De Saintignon, P. Gabor, A. Hoummada, G. Mahout, D. Marchand, F. Merchez, E. León Florián, C. Leroy, Ph. Jean and B. Merkel, *SARA, A Neutron Irradiation Station Featuring Cryogenic Temperatures.* Proceedings of the Large Scale Application and Radiation Hardness of Semi-Conductors, Florence, Italy, 7–9 July 1993, Eds. A. Baldini and E. Focardi, SIF, Bologna, Vol. 46, p.191, 1994.

[47] J. Collot, P. De Saintignon, P. Gabor, A. Hoummada, G. Mahout, D. Marchand, F. Merchez, E. León Florián, C. Leroy, Ph. Jean and B. Merkel, *SARA, A Neutron Irradiation Station Dedicated to Large Hadron Collider Detector Design.* Proceedings of the Fourth International Conference on Calorimetry in High Energy Physics, La Biodola, Isola d'Elba, Italy,, 19–25 September 1993. Eds. A. Menzione and A. Scribano, World Scientific (Singapore), p.635, 1994.

[48] E. León Florián and C. Leroy, *Neutron and Photon Doses Measured Using Thermoluminescent Dosimeters at the SARA Irra-*

*diation Facility*, Nuclear Science Journal **Vol. 31** No 5, p.380, 1994.

[49] A. Fassò, A. Ferrari, J. Ranft, P. R. Sala , G. R. Stevenson, J. M. Zazula, *FLUKA92*. Presented at the Workshop on Simulating Accelerator Radiation Environments, Santa Fe, USA, 1-15 January 1993.

[50] A. Fassò, A. Ferrari, J. Ranft, P. R. Sala, *FLUKA: Present Status and Future Developments.* Presented at the IV International Conference on Calorimetry in High Energy Physics, La Biodola, Italy, 21-26 September 1993.

[51] P. A. Aarnio, A. Fassò, A. Ferrari, J.-H. Möhring, J. Ranft, P. R. Sala, G. R. Stevenson and J. M. Zazula, *FLUKA: Hadronic Benchmarks and Applications*, CERN TIS-RP/93-08/CF, 1993.

[52] G. R. Stevenson, A. Fassò, A. Ferrari and P. R. Sala, *The Radiation Field in and Around Hadron Collider Detectors*, CERN/TIS/RP/92-07CF, 1992.

[53] M. B. Emmett, *The MORSE Monte–Carlo Radiation Transport Code System*, Oak Ridge National Laboratory Report ORNL-4972, 1975.

[54] W. Guber, J. Nagel, R. Goldstein, P. S. Mettelman and M. H. Kalos, Report MAGI-6701, 1967.

[55] R. Brun, M. Hansroul, P. Palazzi, B. Peuchot, *Hbook User Guide*, CERN-DD 75-11, 1975.

[56] A. Van Ginneken, *Non Ionizing Energy Deposition in Silicon for Radiation Damage*, Technical Report FN-522, Fermi National Accelerator Laboratory, 1989.

[57] R. S. Caswell, J. J. Coyne and M. L. Randolph; *Kerma Factors for Neutron Energies Below 30 MeV*, Radiation Research **83**, p.217, 1980.

[58] M. Huhtinen and P. Aarnio, *Pion Induced Displacement Damage in Silicon Devices*, Nucl. Instrum. and Methods **A335**, p.580, 1993.

[59] Paul Scherrer Institut: *Users' Guide Accelerator Facilities*, edited by Paul Scherrer Institut, Villigen and Würenlingen, CH-5232 Villigen PSI, 1994.

[60] E. León Florián and C. Leroy, *Particle Contamination Measurements around Hadron Beams used for Irradiation of Silicon Detectors for the LHC.* Proceedings of the 3ème Colloque Européen: Radiations et leurs Effets sur les Composants et Systèmes, RADECS 95, Arcachon, France, 18-22 September 1995, IEEE Trans. Nucl. Sci., IEEE Catalog Number 95TH8147, p.101, 1995.

[61] E. León Florián and C. Leroy, *Neutron and Photon Contamination near $\pi^+$ Beams during Irradiation of Silicon Detectors.* Proceedings of the 2nd International Conference on Large Scale Applications and Radiation Hardness of Semiconductors Detectors, Eds. E. Catacchini and E. Focardi, SIF, Bologna, p.1389, 1996.

[62] P. Aarnio and M. Huhtinen, *Hadron Fluxes in Inner Parts of LHC Detectors*, Nucl. Instr. and Methods **A336**, p.98, 1993.

[63] C. Leroy, S. Bates, B. Dezillie, M. Glaser, F. Lemeilleur, I. Trigger, *Study of Charge Collection and Noise in Non–irradiated and Irradiated Silicon Detectors*, Nucl. Instr. and Methods **A388**, p.289, 1997.

[64] A. H. Sullivan, *A Guide to Radiation and Radioactivity Levels near High Energy Particle Accelerators*, Nuclear Technology Publishing, ISBN 1 870965 18 3, 1992.

[65] A. Smith, *Threshold Detectors Applications to Neutron Spectroscopy at the Berkeley Accelerator*, LBL, 1965.

[66] Landolt, Hans Heinrich, Landolt-Börnstein, *Numerical Data and Functional Relationships in Science and Technology*, New series Group I: Production of Radionucleides at Intermediate Energies, d: Interactions of Protons with Nuclei, Vol. 13, Springer-Verlag, Berlin, ISBN 3-544 0-57540-5, 1994.

[67] G. N. Timoshenko and A. R. Krylov, *The High Energy Neutron Spectrometry in Mixed Unidirectional Radiation Fields Behind Accelerator Shielding*, JINR-E16 89-59, 1989.

J. Russ et. al., *Low Energy Neutron Measurements in an Iron Calorimeter Structure Irradiated by 200 GeV/c Hadrons*, CERN/TIS-RP/89-02, 1989.

[68] G. R. Stevenson, A. Fassò, M. Höfert and J. Tuyn, *Dosimetry at High–Energy accelerators*, CERN/TIS-RP/95-07/PP, 1995.

[69] J. Ranft, *Estimation of Radiation Problems around High Energy Accelerators using Calculations of the Hadronic Cascade in Matter*, Particle Accelerators, p.129, 1972.
H.J. Möhring, *Hadron–nucleus Inelastic Cross–Sections For Use in Hadron–Cascade Calculations at High Energies*, TIS-RP/116, 1983.

[70] V. McLane, C. L. Dunford, and P. Rose, *Neutron Cross Sections*, National Nuclear Data Center-Brookhaven National Laboratory, ISBN 0-12-484-220-8, Vol. 2, Academic Press, Inc., 1988.

[71] S.J. Bates, C. Furetta, M. Glaser, F. Lemeilleur, C. Soave and E. León Florián, *Damage Induced by Pions in Silicon Detectors.* Proceedings of the 4th International Conference on Advance Technology and Particle Physics, Villa Olmo, Como, Italy, 3-7 October 1994, Nucl. Phys. B, Proc. Suppl. **44**, p.510, 1995.
G. N. Taylor *et. al.*, *Radiation Induced Bulk Damage in Silicon Detectors*, Nucl. Instrum. and Methods **A383**, p.144, 1996 .

[72] S. J. Bates, B. Dezillie, C. Furetta, M. Glaser, F. Lemeilleur and E. León Florián, *Proton Irradiation of various Resistivity Silicon Detectors.* Proceedings of the 3ème Colloque Européen: Radiations et leurs Effets sur les Composants et Systèmes, RADECS 95, Arcachon, France, 18-22 September 1995, IEEE Trans. Nucl. Sci, IEEE Catalog Number 95TH8147, p.487, 1995.

[73] A. Vasilescu, *The NIEL Scaling Hypothesis Applied to Neutron Spectra of Irradiation Facilities and in the ATLAS and CMS SCT*, ROSE/TN/97-2, 1997.

[74] **ASTM**, *Standard practice for Characterization Neutron Energy Fluence Spectra in Terms of an Equivalent Monoenergetic Neutron Fluence for Radiation–Hardness Testing of Electronics* Annual Book of ASTM Standard, Vol 12.02, Chap ASTM E722-85, 1985.

[75] A. I. Namenson, E. A. Wolicki, and G. C. Messenger, *Average Silicon Displacement Kerma Factor at 1 MeV*, IEEE Transactions on Nuclear Science **NS–29**, p.1018, 1982 .

[76] M. S. Lazo et al. Sandia Nat. Lab. Technical Report SAND87-0098 Vol. 1. Proceeding of the Fast Burst Reactor Workshop, p 85, 1986.

T. F. Luera, J. G. Kelly, H. J. Stein, M. S. Lazo, C. E. Lee and L. R. Dawson, *Neutron Damage Equivalence for Silicon Dioxide and Gallium Arsenide*, IEEE Transactions on Nuclear Science **NS–34**, No 6, p.1557, 1987.

[77] J. Lindhard, V. Nielson, M. Scharff and P.V. Thomsen, K. Dan. Vidensk, Mat. Fys. Medd., Vid Selsk. **33(10)**, Number 14, 1963.

[78] A. M. Ougougag, J. G. Williams, M. B. Danjaji, S.-Y. Yang and J. L. Meason, *Differential Displacement Kerma Cross Section for Neutron Interactions in Si and GaAs*, IEEE Transactions on Nuclear Science **NS–37**, No. 6, 1990.

[79] G. P. Summers, E. A. Burke, P.Shapiro, S. R. Messenger and R. J. Walters, *Damage Correlations in Semiconductors Exposed to Gamma, Electron and Proton Radiations*, IEEE Transactions on Nuclear Science **Vol.–37**, No. 6, 1993.

[80] I. Lazanu, S. Lazanu, U. Biggeri, E. Borchi and M. Bruzzi, Nucl. Instr. and Methods **A388**, p.370, 1997.

[81] M. Moll, *Radiation Damage in Silicon Particle Detectors– microscopic defects and macroscopic properties*, Ph.D. thesis, University of Hamburg, DESY–THESIS–1999–040, ISSN 1435–8085, 1999.

[82] The ROSE Collaboration, *RD48 Status Report*, CERN/LHCC 97-39, 1997.

[83] A. Chilingarov et.al., Nucl. Instr. and Methods **A360**, p.432, 1995.

[84] S. J. Bates, *The Effects of Proton and Neutron Irradiations on Silicon Detectors for the LHC*, Ph.D. Thesis, University of Cambridge, Cambridge, UK, 1993.

[85] T. Kojima et al., *Alanine Dosimeters Using Polymers as Binders*, Applied Radiation and Isotopes **6**, p.37, 1986.
D. F. Regulla et al., Int. Applied Radiation and Isotopes **33**, p.1101, 1982.
U. Deffner et al., *Influences of Physical Parameters on High-Level Amino Acid Dosimetry*, Nucl. Instr. and Methods **175**, p.134, 1980.

[86] M. Coche, F. Coninckx, H. Schönbacher, A. Bartolotta, S. Onori, A Rosati, *Comparison of High–Dose Dosimetry Systems in Accelerator Radiation Environments*, TIS Comission Report, 1988.
F. Coninckx, H. Schönbacher, A. Bartolotta, S. Onori and A.

Rosati, *Alanine Dosimetry as the Reference Dosimetric System in Accelerator Radiation Environments*, Applied Radiation and Isotopes **40** No 10-12, p.977, 1989.

F. Coninckx,H. Schönbacher, M. Tavlet, G. Paic, D. Razem, *Comparison of High–dose Dosimetry Systems for Radiation Damage Studies in Collider Detectors and Accelerators* Nucl. Instrum. and Method., **B 83**, p.181, 1993.

[87] Y. Furuta et al., *Response of $^6$LiF and $^7$LiF Thermoluminescence Dosimeter to Fast Neutrons*, Nucl. Instr. and Methods **104**, p.365, 1972.

L. Larsson, M. Alpsten, B. A. Lindskoug and Sköldborn, *The Response of LiF Dosimeters in the Radiation Field of a 14 MeV Neutron Generator*, Nucl. Instr. and Methods **175**, p.189, 1980.

M. Singh, J. L. Gaines and J. R. Parlagreco, *Local Energy Transfer to TLDs by Neutrons and Photons*, Nucl. Instr. and Methods **175**, p.31, 1980.

Wang Tien-Ko, *On the Use of TLD for Gamma Ray Dosimetry Evaluation in Mixed Fast Neutron and Gamma Ray Fields*, Radiation Protection Dosimetry **33**, No 1/4, p.359, 1990.

[88] K. Becker, *Solid State Dosimetry*, Boca Raton, Florida: CRC Press Inc., ISBN 0-87819-046-5, 1973.

K. Mahesh et al., *Thermoluminescence in Solids and its Applications*, Nuclear Technology Publishing, Ashford, UK, 1989.

[89] K. R. Kase and W. R. Nelson, *Concepts of Radiation Dosimetry*, ISBN 0-08-0231624, Pergamon Press Inc., 1978.

[90] Edited by K. R. Kase, B. E. Bjärngard and F. H. Attix, *The Dosimetry of Ionizing Radiation*, Volume II, Academic Press, Inc., 1987.

[91] G. Paič, *Ionizing Radiation Protection*, CRC Press, Inc., Boca Raton, Florida, ISBN 0-8493-6713-1, 1988.

[92] A. H. Wells, *A Consistent Set of Kerma Values for H, C, N and O for Neutrons of Energies from 10 to 80 MeV*, Radiation Research **80**, p.1, 1979.

[93] E. León Florián, H. Schönbacher and M. Tavlet, *Facilities and Dosimetry for Detector Material Irradiations.* Proceedings of the 20th Workshop of the INFN Eloisatron Project "GaAs Detectors and Electronics for High-energy Physics", ISBN 981-02-1148-1, Editors: C.del Papa, P.G. Pelfer & K. Smith World Scientific, 145,1992.

[94] G. R. Stevenson, *Normalization for Non-Uniform Irradiation of Activation Detectors*, Rutherford Laboratory Internal Report RHEL RP/PN 39, 1969.

[95] W. L. Zijp, *Review of Activation Methods for the Determination of Neutron Flux Density Spectra.* Proceedings of the First ASTM-EURATOM Symposium on Reactor Dosimetry, Report EUR e/f Vol. I, p.233, 1977.

# Appendix A

# Dosimetry methods and absorbed dose calculations

This appendix starts with a short description of the ESR and TLD dosimetry methods used in the present work. Calculations of absorbed doses from photons, neutrons, and charged particles are also presented.

## A.1 Dosimetry techniques

### A.1.1 ESR: Polymer-alanine dosimeters (PAD)

The alanine dosimeter uses the stable paramagnetic centers generated by ionizing radiation in the $\alpha$-amino acid: $CH_3$-$CHNH_2$-COOH. The created free radicals ($CH_3$-$\dot{C}H$-COOH) are detected by the Electron Spin Resonance Technique, and they represent a measure of the amount of the energy imparted to the material [85]. The peak-to-peak signal height is used as a dose dependent parameter (see Fig. 30).

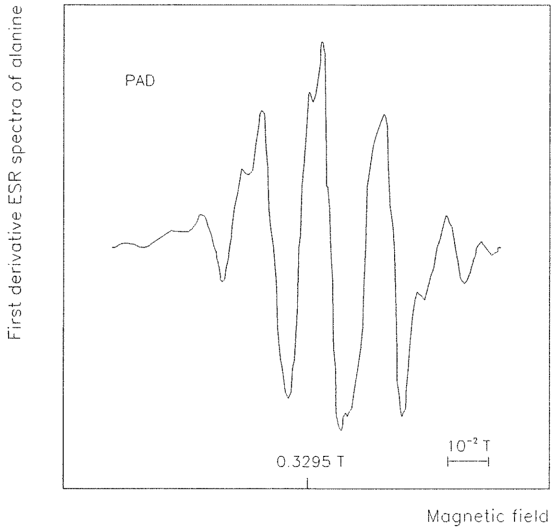

Figure 30: ESR spectra of Polymer-alanine dosimeter (PAD) at $10^3$ Gy with $^{60}$Co. Recording conditions: temperature 18°C; microwave power 1.25 mW; modulation amplitude $2.5 \times 10^{-4}$ Tesla; scan range $10^{-2}$ Tesla; field set at 0.3295 Tesla; microwave frequency 9.425 GHz; time constant 0.3 s; scanning time 60 s; gain $1.5 \times 10^4$.

The dosimeter is based on a homogeneous mixture of 33% of polymer-ethylene-propylene rubber (EP-rubber) and 67% DL-$\alpha$ alanine, by weight. One of the advantage of this dosimetric technique for radiation-damage studies is its wide dose range: 10 Gy to $5 \times 10^5$ Gy [86]. The response is linear over the range 50 Gy to 30 kGy, as shown in Fig. 31.

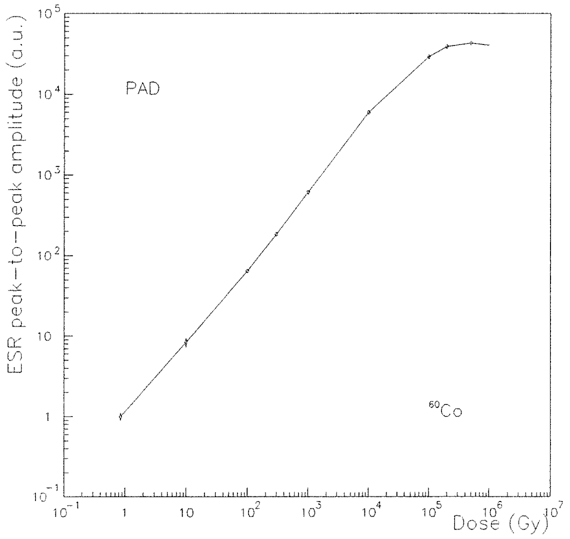

Figure 31: Polymer-alanine dosimeter (PAD) calibration curve-(CERN). The alanine dosimeters were calibrated using $^{60}$Co gamma rays.

### A.1.2 Thermoluminescence dosimetry

When a thermoluminescent crystals is exposed to ionizing radiation, electrons are raised from the valence band to the conduction band and move freely through the crystal. Normally, these electrons would fall back into the valence band, but some are trapped by lattice defects and impurities. The electrons will remain in these traps until they acquire sufficient energy to escape. This energy is provided in the form of heat. Escape and return to the valence band is accompanied by emission of one or more photons. Free positively charged holes are produced along with the free electrons and may undergo a similar process. The net result of the heating is recombination of the electrons and holes. The resulting light emission occurs at temperatures corresponding to the depths of the traps.

The emission of light as a function of temperature is known as the **glow curve**. The shape of this curve, and the heights of the peaks, are determined by the intrinsic qualities of the basic phosphor and by the activator concentrations. Each TL phosphor has a characteristic glow curve (see Fig. 32). The area of a glow peak is a function of the number of electrons released from the corresponding traps, and it is proportional to the radiation absorbed dose.

The most important families of phosphors used for dosimetric purposes are: lithium fluoride (LiF) [87], lithium borate ($Li_2B_4O_7$), calcium sulfate ($CaSO_4$), and calcium fluoride ($CaF_2$) [88]. A thermal treatment called **annealing** is necessary in order to re–use the dosimeter. For LiF, the annealing consists of: 1 hour at 400°C, followed by 2 hours at 100°C in air, and cooling at room temperature.

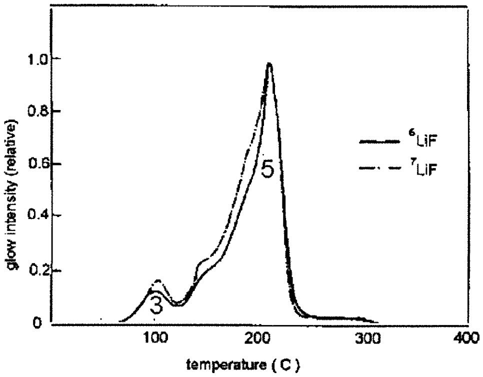

Figure 32: Glow curves of $^6$LiF (TLD-600) and $^7$LiF (TLD-700) irradiated by $^{60}$Co gamma rays (main peak is normalized to unity at 210°C).

## A.2 Absorbed dose calculations

### A.2.1 Calculation of absorbed doses from gamma rays

The calculation of the photon absorbed dose is as follows:

1. First the photon flux density ($\varphi_i$ in cm$^{-2}$ s$^{-1}$) is determined (or measured) at the point of interest;
2. $\varphi_i$ is multiplied by the energy of the photons (E$_i$ in MeV) to obtain the energy flux density;
3. energy flux density is multiplied by the mass energy absorption coefficient ($(\mu_{en}/\rho)_m^{E_i}$ in cm$^2$ g$^{-1}$) of the medium, to determine how much of the energy is actually deposited at the point of interest;
4. finally, the appropriate constants are applied to convert the units to Gray (Gy) and multiplying by the time $t$ during which the photon flux density was present yields the absorbed dose [89].

Mathematically:

$$D(Gy) = 1.6 \times 10^{-10} \sum_i \varphi_i \, E_i \, (\mu_{en}/\rho)_m^{E_i} \, t \tag{A.1}$$

When the photon absorbed dose is calculated by means of equation A.1, charged particle equilibrium (CPE) is assumed at the point of interest, since the mass energy absorption coefficient considers only the energy deposited by photon interactions in the mass element at the point of interest. If charged particle equilibrium is not achieved, one must somehow calculate the difference between energy entering and leaving the mass element on charged particles.

### A.2.2 Calculation of absorbed doses from neutrons

The differential neutron fluence (or fluence spectrum) Φ(E) (in neutrons per MeV per square meter) is defined by Φ(E) dE, the number of neutrons of energy in the range E, E + dE per unit area. The neutron absorbed dose D (in Grays) is related to the fluence [90] by:

$$D = \int_0^\infty \Phi(E) k(E)\, dE \tag{A.2}$$

where $k$(E) is the neutron *kerma factor* of the material (Gy $m^2$/neutron).

#### Kerma factor

When the neutron does interact, it may undergo a variety of nuclear processes depending on its energy. For energies up to 20 MeV, interactions are either elastic ((n,n)), inelastic ((n,n'), (n,n'$\gamma$)) scattering or they are simple (n,2n), (n,p), and (n,$\alpha$) reactions. The sum of the kinetic energies of all charged ionizing particles produced in these interactions represent the **kerma** [1] **K**. For neutrons of energy E, one has [91]:

$$K_n(E) \;=\; \Phi(E)\, E \sum_{i,j} N_i\, \sigma_{i,j}(E)\, f_{i,j} \tag{A.3}$$

where Φ is the neutron fluence, $N_i$ is the number of nuclei of the $i$th element per unit mass, $\sigma_{i,j}$ is the cross section of the reaction on the $i$th element resulting in the charged particle $j$, and $f_{i,j}$ is the average fraction of the

---

[1] The **kerma** (Kinetic Energy Released per unit MAss), is the quotient of $dE_{tr}$ by $dm$, where $dE_{tr}$ is the sum of the initial kinetic energies of all charged ionizing particles liberated by uncharged ionizing particles (or indirectly ionizing particles) in a material of mass $dm$.

energy that is transferred to kinetic energy in the particular process.
Equation A.3 can be rewritten as:

$$K_n(E) = \Phi(E)\, k(E) \tag{A.4}$$

where $k$(E) is the *kerma factor* per unit fluence. At low energies (less than 5 MeV) this quantity is dominated by the elastic scattering. When the neutron energy increases, the contribution of inelastic scattering and two–body nuclear reactions are more significant. At energies above 15 MeV, the multiple breakup is dominant. The many-body cross sections are not well known, and this gives a large uncertainty in the kerma factors above 20 MeV. In addition to the kinetic energy released by the nuclear reaction products, some of these products are radioactive and their $\beta$ decays make an additional contribution to the kerma. The kerma does not include the gamma ray contribution.
Kerma factors for many materials and compounds have been calculated by [57, 92]. The kerma factors for silicon and silicon oxide are shown in Fig. 33. The compounds kerma factors can be calculated using the following relation:

$$k_{compound}(E) = \sum_i a_i\, k_i(E) \tag{A.5}$$

where $a_i$ is the fraction by weight (atomic mass of the element divided by the compound atomic mass) and $k_i$(E) are the kerma factors corresponding to each element at certain energy E. For example, in the case of $SiO_2$, the atomic mass of silicon is 28, and 16 for oxygen, then:

$$k_{SiO_2}(E) = 28/60 \times k_i^{Si}(E) + 32/60 \times k_i^{O}(E)$$

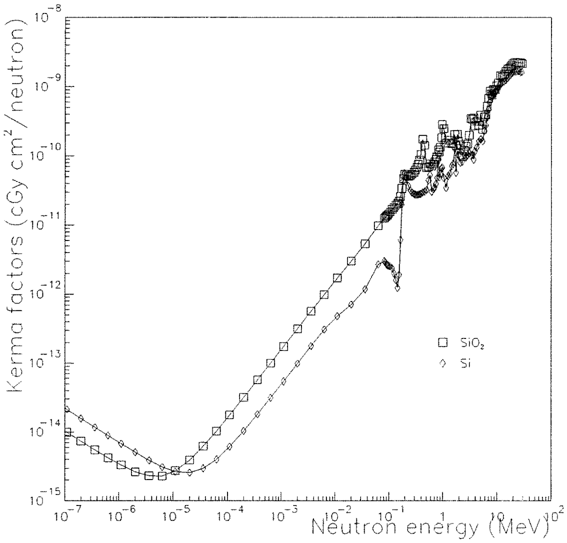

Figure 33: Kerma factors per unit of fluence for silicon (Si) and silicon dioxide ($SiO_2$).

### A.2.3 Calculation of absorbed doses from charged particles

For a particle fluence per unit of energy $\Phi(E)$ that enters a volume of cross section area dA and depth dl, the dose for electrically charged particles is defined as [89]:

$$D(Gy) = \frac{1.6 \times 10^{-10}}{\rho} \int_0^{E_m} \frac{dE}{dx}(E)\,\Phi(E)\,dE \qquad \text{(A.6)}$$

where the beam of particles has a spectrum with a maximum energy $E_m$. In this equation the stopping power, $dE/dx$, is in units of MeV $cm^{-1}$. The fluence $\Phi$ is in units of particles $cm^{-2}$ $MeV^{-1}$, and the density $\rho$ in units of g $cm^{-3}$. The factor $1.6 \times 10^{-10}$ comes from 1 Gy = $6.24 \times 10^{9}$ MeV $g^{-1}$.

In the case of high energy charged particles, as can be seen in Fig. 34, the stopping power passes through a broad minimum where the rate of energy loss in the region is 2 MeV $cm^2$ $g^{-1}$. Charged particles in this energy range are referred to as **minimum ionizing particles** or **mip's**. An estimate of the minimum ionizing energy loss rate, $(dE/dx)_{min}$, taking into account the atomic weight A and the atomic number Z of the material being traversed, is approximated by [64]:

$$\left(\frac{dE}{dx}\right)_{min} = 3.76\, Z/A \qquad MeV\, cm^2\, g^{-1} \tag{A.7}$$

The energy loss is mainly deposited along the track of the particle, but at very high energies, appreciable energy (a few MeV) can be transferred to electrons (also called $\delta$–rays) that deposit energy away from the primary track, effectively reducing the rate of energy deposition close to the charged particle track.

The dose absorbed by a thin object placed in a charged particle beam depends primarily on the rate of energy loss of the particles and their distribution across the beam. As shown in Fig. 34, protons of energy greater than about 600 MeV and muons and pions with energy above about 100 MeV deposit energy at a rate of about 2 MeV $cm^2$ $g^{-1}$ in practically all target materials. This so-called **minimum ionizing energy loss** rate can be converted to absorbed dose per unit of fluence of high energy charged particle (conversion factor CF) and is equivalent to:

$$CF = \frac{3.76}{1.73}\,\frac{Z}{A}\,\frac{\mu Gy\, h^{-1}}{cm^{-2}\, s^{-1}} \tag{A.8}$$

where $1\mu$ Gy $h^{-1}$ = 1.73 MeV $g^{-1}$ $s^{-1}$ was used.

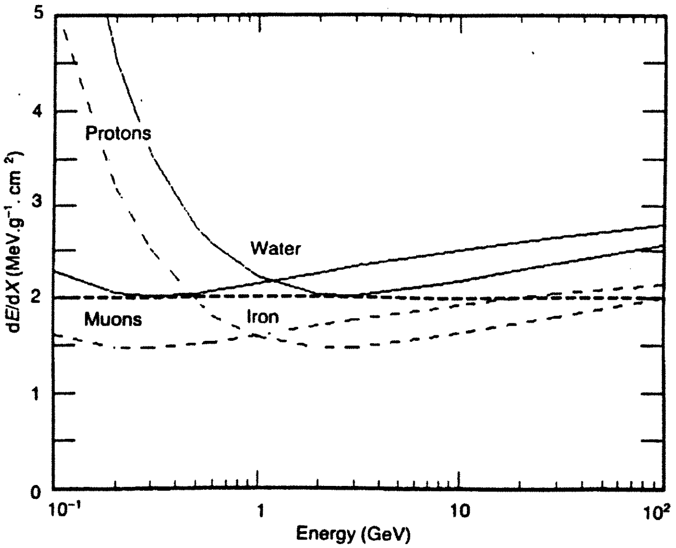

Figure 34: The stopping power of protons and muons in water (solid curves) and iron (dashed curves) as a function of the particle energy. The stopping power for pions will be similar to that of muons.

For the purpose of calculating the dose in a charged particle beam, it is conventional to express the particle flux density as *particles* per $cm^2$ per *second* [64]. In which case, the appropriate factor (CF) to convert flux density into absorbed dose–rate becomes (considering $\left(\frac{dE}{dx}\right)_{min} = 2$ MeV cm$^2$ g$^{-1}$):

$$CF = 1.16\ \frac{\mu Gy\, h^{-1}}{cm^{-2}\, s^{-1}} \tag{A.9}$$

An example of this is the calculated absorbed dose in silicon material due to proton fluences, shown in experimental results at ZT7-PS.

# Appendix B

# Particle flux density measurements

Particle flux density measurements require a careful selection of the reactions considering both practical and physical constraints [27]. Usually, the reactions are selected for a given type of particle, for a given range of energy, corresponding to the energy spectrum of the particles produced at the irradiation facility, and well known cross-sections and characteristics of the produced nuclei (half-life, decay mode, decay energy).

The duration of the irradiation to be monitored is another constraint to consider. If the half-life of the measured isotope is very much longer than the irradiation time, the reaction may be too insensitive. If, on the other hand, the irradiation time is very much longer than the half-life of the reaction product, the result obtained may be quite inaccurate.

In the high energy environment of accelerators, one must take special care while selecting reactions because multiple reactions could take place with the resulting production of many radionucleides.

Another aspect to consider is that the component materials of the activation foil should be free of interfering impurities. The total size and thickness should be small enough to avoid excessive self-absorption and attenuation of the softest gamma-rays to be measured and it must present no unacceptable handling difficulties.

Thermal neutrons are usually detected by (n,$\gamma$) reactions. The choice of the activation foil depends on the low energy neutron flux density to be measured and the time over which it has to be measured [28, 29]. It is easy to find (n,$\gamma$) reaction with suitable half-life and absorption cross-section [70]. Medium and high energy neutrons are measured using threshold activation foils [28, 30, 93]. Threshold activation foils require a minimum neutron energy to initiate activation. They give no response below threshold. Above it, they have a response proportional to the excitation functions of the activation foil. Differences in the response function of activation foils [70] are the basis for methods developed to determine spectra from activation data.
In reference [27] there are useful neutron and charged particles reactions associated with their approximate effective threshold energy, half-life and gamma energy emission of the created nuclei.

## B.1 Analytical methods

### B.1.1 Gamma spectrometry

A typical gamma spectrum consists of a number of peaks corresponding to the gamma rays of the elements measured. The peaks are superimposed over a continuous background originating from the Compton scattering of gamma rays in the detector (that can be NaI(Tl) scintillators, high purity Ge or Si(Li) semiconductor detectors for instance) [38, 39]. The number of counts in a peak, less the background, is a measurement of the activity of a specific nuclei. Modern gamma spectrometers are linked to computers that perform all the needed calculations according to a radionucleus data table stored in it. A computer program such a INTERGAMMA [40], provides a reliable printout of activities a few minutes after the end of the measurement.

## B.2 Computation methods

This section briefly describes the computer programs used in activation analysis.

**INTERGAMMA**

This program permits the automatic processing of the spectra. It needs the experimental efficiency curve and the nuclei table as inputs supplied by the user. The output gives the photopeaks: their energy in keV, the identified nuclei, the net area in counts, the FWHM (Full Width at Half Maximum), the statistical error of the measurements and the activity corrected by decay during the counting time, expressed in Bq [40].

**ENNUI** (Effective normalization for non-uniform irradiations)

ENNUI can be used in the case of accelerators, where fluctuations in the intensity of the beam frequently happen. This directly affects the activity produced in the foil. It is therefore necessary that the results of measurement be normalized as to what they would have been in the case of uniform irradiation. From a history of the fluences, ENNUI calculates the ENNUI normalization factor [94].

## B.3 Source of errors in the activation measurements

Impurities and errors in component masses and the effects of impurities are small when high-purity materials are used. The uncertainties from these effects are of the order of less than 1%.

Weighing of foils (during their use) is another source of uncertainties. In the worse case, it gives errors of the order of 5%. This could happen when the foils are cut mechanically and then, special care should be taken when small foils are going to be used.

For threshold activation foils, neutron self-shielding effects are very small if the masses of the foils are well below one gram. Related uncertainties are below 1 %.

In the case of radiation damage studies, the activation foils used are usually thin, with a well defined geometry. The attenuation in thin foils is negligible, but in the case of thick foils with an emission of low energy gamma rays, the attenuation can be estimated with great accuracy.

The errors in the gamma spectrum counting and analysis are due to statistical variations in the pulse counts, errors in efficiency calibration, errors in the peak area calculation, and errors in branching ratios and half-lives.

The largest source of error seems to be on the efficiency calibration of the gamma spectrometer. These errors, however, can be reduced considerably if calibration is performed frequently (three times a year, for example) or performed specifically before a measurement. Then, when the gamma spectrum is automatically processed, the total uncertainty in the activity determination can be obtained as the root of the sum of the squares of the errors on the various contributions and is typically about 5%.

Estimated uncertainties carried out by cross-sections are in the range 5 to 14% [95].

# Appendix C

# Nuclear Instruments and Methods A 350, p. 525–529, 1994.

Nuclear Instruments and Methods in Physics Research A 350 (1994) 525-529

ELSEVIER

NUCLEAR INSTRUMENTS & METHODS IN PHYSICS RESEARCH
Section A

# A neutron irradiation facility featuring cryogenic temperatures and dedicated to Large Hadron Collider detector design

J. Collot [a,*], P. De Saintignon [a], P. Gabor [a], A. Hoummada [a,1], G. Mahout [a], D. Marchand [a], F. Merchez [a], E. León Florián [b], C. Leroy [b,2], Ph. Jean [c], B. Merkel [c]

[a] *Institut des sciences nucléaires de Grenoble, CNRS IN2P3 – Université Joseph Fourier, 53, Av. des Martyrs, 38026 Grenoble Cedex, France*
[b] *Université de Montréal, Centre de physique nucléaire, C.P. 6128, succursale "A" Montréal, Québec H3C3J7, Canada*
[c] *Laboratoire de l'accélérateur linéaire d'Orsay, CNRS IN2P3 – Université de Paris Sud, Bâtiment 200, F91405 Orsay Cedex, France*

Received 17 December 1993; revised 13 June 1994

## Abstract

The SARA facility at Grenoble provides the possibility to carry out neutron irradiation studies at both cryogenic and room temperatures, and permits at the same time to measure on-line the deterioration of the electronic performance of the tested circuits. The cryogenic vessel consists of a 10 l liquid argon cryostat placed behind the neutron source. A TOF technique was used to measure the neutron energy spectrum produced by the collision of a 20 MeV deuteron beam on a thick Be target. Alanine and thermoluminescent dosimeters were used to determine the neutron and photon doses. The results show that the neutron and the gamma dose components are about 78% and 22%, respectively. The angular distribution of the dose was also measured.

## 1. Introduction

The very large neutron fluences (up to $\approx 10^{13}$–$10^{14}$ neutrons/cm$^2$/yr) foreseen for the next generation of hadron colliders, will create a high-level radiation environment and challenge the performance of the detectors and their readout electronics. Furthermore, calorimetry using liquid argon as an active medium will be certainly used and raises the question of the radiation hardness of the detector components at cryogenic temperatures.

Neutron sources based on stripping of deuterons ($^9$Be(d,n)$^{10}$B) on thick beryllium targets have been used for decades in studying the damage effects of neutrons on various materials [1]. On light ion accelerators, this process offers the most effective way of producing high intensity neutron fluxes at low cost. This neutron production technique is also particularly interesting in the context of the R&D efforts dedicated to the design of the LHC detectors. Here, and at least for the ATLAS detector [2,3] high neutron fluences under cryogenic conditions are required for investigating realistically the deterioration induced by radiation exposure. Cryogenic temperatures are hardly conceivable in the environment of nuclear reactors that constitute the classical neutron sources, whereas they can be easily achieved in the context of small accelerators. Another useful property of this type of source is the fact that, as opposed to nuclear reactors, they produce very few thermal neutrons. This is due to the kinematics of the production reaction and the reduced quantity of material needed to build a target assembly. The absence of thermal neutrons drastically lowers the undesirable activation of the exposed samples.

We present in this article the main characteristics of a neutron irradiation station that was recently installed at a cyclotron located in Grenoble. It permits us to expose electronic circuits, opto-electronic components such as optical fibers and LED's, as well as mechanical parts at cryogenic temperatures provided by a liquid argon cryostat. Real-time measurements, especially of the electronic and optical performance of the tested circuits, were also made possible.

A time-of-flight technique was used to measure the neutron energy spectrum. Alanine and thermoluminescent dosimeters were utilized to determine the neutron and photon doses.

## 2. Description of the site

A thick beryllium target 35 mm in diameter (Fig. 1) constitutes the neutron source, and is located at the end of one of the SARA [4] beam lines. A 5 $\mu$A beam of 20 MeV deuterons is stopped on the Be disk producing a high neu-

---

[*] Corresponding author. Tel. +33 76 28 40 00, fax +33 76 28 40 04.

[1] Guest professor of Université Joseph Fourier. Permanent address: Faculté des sciences Ain Chock B.P. 5366 Maarif Casablanca, Marocco.

[2] Killam Fellow.

*SSDI* 0168-9002(94)009485-1

tron flux by stripping reactions. The Be thickness required to absorb this beam completely is 1.6 mm. For safety reasons, we decided to mount a 3 mm thick Be disk. The beam power (100 W) released in the Be target is removed by a water coolant flow that is placed in thermal contact with the source through a brazed copper ring. At the full beam power, the highest temperature on the target does not exceed 40°C. At the design level, some precautions have been taken to maintain the Be disk electrically insulated, thus permitting an on-line monitoring of the beam current that stops in it. Because of the emission of secondary electrons from the beryllium, the beam current as seen by the target is approximately 20% higher than the real one. In order to ease the tuning and the positioning of the beam on the target with a radiation-robust system, a carbon ring segmented into four separate sectors whose currents are independently read out, was fixed a few centimeters upstream. It defines the allowed external diameter (25 mm) in which the beam is focused.

The liquid argon cryostat consists of a cylindrical vessel 30 cm in diameter, surrounded by a 5 cm thick external thermal insulation. The vessel walls have been made of aluminum in order to minimize the neutron activation and consequently to ease its handling after the exposures. It can contain up to 10 l of liquid argon kept cool by circulating pressurized liquid nitrogen through an internal heat exchanger. As can be seen in Fig. 1, the cryostat is installed as close to the Be target as possible, reaching a minimal irradiation distance of 10 cm. Some feedthroughs allow us to bias the exposed electronic circuits, to read their output pulses, and to insert optical fibers used in opto-electronic tests. During the room temperature irradiations, the cryostat walls are removed, and an aluminum plate is installed to support the exposed samples in front of the target.

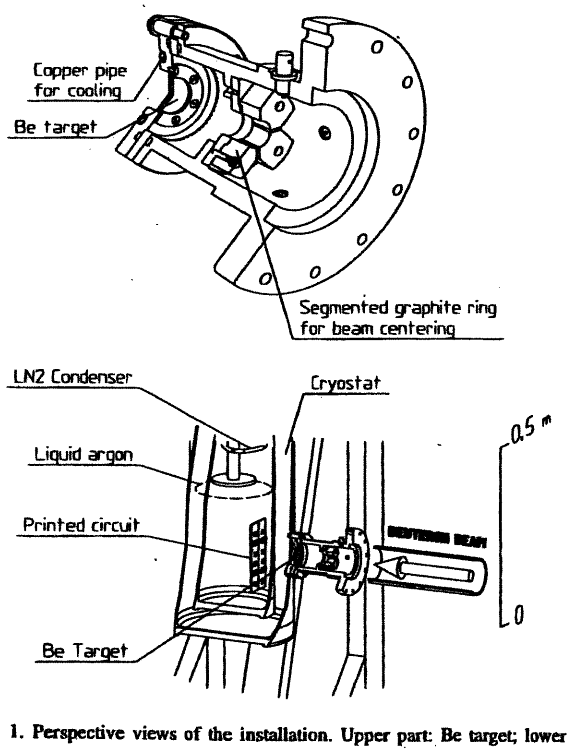

Fig. 1. Perspective views of the installation. Upper part: Be target; lower part: liquid argon cryostat with the target mounted in front.

The entire assembly is located in an irradiation casemate which features 2 m thick walls of concrete loaded with barium ore. No noticeable neutron flux leakage was registered outside the casemate when operating at full power.

## 3. Neutron yield and energy spectrum

In a previous dedicated experiment, we measured the neutron yield in the beam direction, i.e. at 0°, from the thick Be target. We utilized a conventional neutron detector consisting of a NE213 cylinder (5 cm thick, 10 cm in diameter) [5] that was operated with a neutron threshold of 1 MeV. As the overall efficiency of such a detector depends on the shape of the neutron energy spectrum, we were led to determine this feature. This was accomplished in the same experiment by recording the time of flight of neutrons over a target-to-detector distance of 2.5 m. The neutron detector efficiency was computed as a function of the neutron energy by the Monte Carlo program of Cecil [6]; it is presented in Fig. 2. Averaged over the energy spectrum, $\varepsilon_n$ was found to be 24% for a neutron threshold of 1 MeV. The neutron yield at 0° was determined to be $4.8 \times 10^7$ (±15%) neutrons $(\mathrm{nA})^{-1}\,\mathrm{sr}^{-1}\,\mathrm{s}^{-1}$ which is in good agreement with other results [1] as depicted in Fig. 3. According to the same references, the neutron yield only drops by less than 20% for emission angles around 10°. It has therefore been assumed that the neutron flux available at 10 (30) cm away from the Be target, is approximately maximal and homoge-

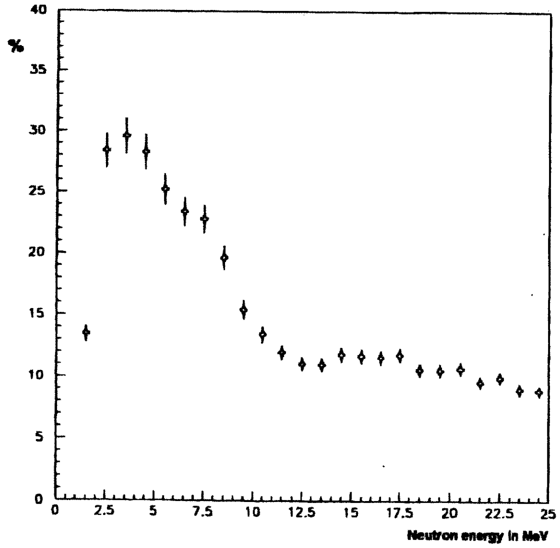

Fig. 2. Neutron detector efficiency as computed by the Monte Carlo program of Cecil.

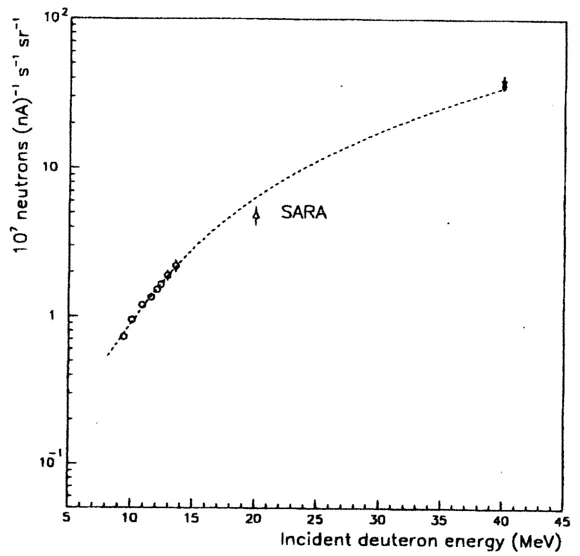

Fig. 3. Neutron yield at 0° for a threshold of 1 MeV as a function of the deuteron incident energy.

neous on a disk of 7 (60) cm$^2$ area centered on the beam axis. The homogeneity statement is reinforced if we take into account the radial extension of the beam impact profile on the target that presents a Gaussian shape of around 6 mm in standard deviation.

The higher energy part of the spectrum shown in Fig. 4 is the result derived from the time-of-flight recording on the NE213 detector. The horizontal error bars reflect the TOF resolution that was estimated around 2 ns mostly due to the deuteron burst duration. The low energy part down to 100 keV was measured by the same TOF technique applied on a fission detector that offers the advantage to remain efficient for observing slow neutrons. It consisted of a $^{235}$U plate mounted a few mm in front of a commercial silicon diode; this assembly being housed in a small evacuated vessel. Neutrons were unambiguously identified by detecting the fission products on the junction. The energy dependence of the neutron efficiency for such a device is proportional to the fission cross section which is precisely known in this domain. The kinematic properties of the fission products are not affected by the variation of the neutron incident energy. Thus, the efficiency variation merely corresponds to the energy variation of the fission cross section. This detector was placed at 70 cm downstream from the Be target to allow 100 keV neutrons to cover this distance in less than the burst period (280 ns). This experiment was achieved with the same typical TOF resolution of 2 ns.

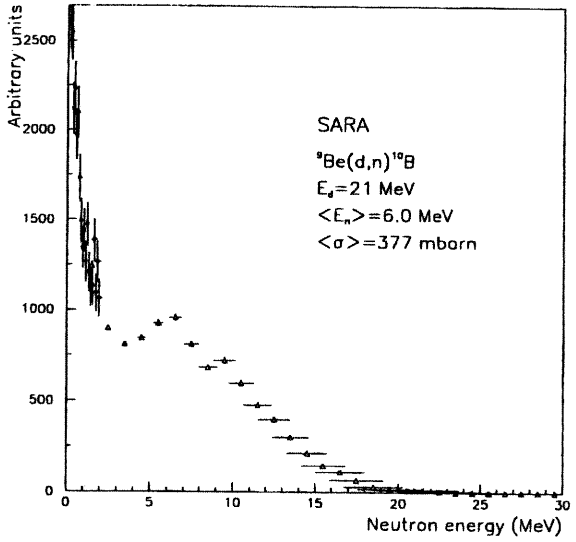

Fig. 4. Neutron energy spectrum measured at 0° with a threshold of 100 keV.

A few irradiations both with and without liquid argon were conducted and showed that, at 10 cm away from the target, neutron fluences of $\approx 2 \times 10^{14}$ neutrons cm$^{-2}$ were obtainable within one day of operation. Fluences measured in irradiations without liquid argon are in good agreement with the predictions deduced from the neutron yield determined at 0° in the TOF experiment, increased by 15% to take into account the part of the neutron spectrum below 1 MeV (except for target-to-sample distances lower than 6 cm where the source transverse size has to be considered). The neutron fluences were measured using an activation method based on the charge exchange reaction on $^{58}$Ni ($^{58}$Ni(n,p)$^{58}$Co) contained in natural Ni samples 4 mm in diameter and 125 $\mu$m thick. For our neutron spectrum at 0°, the mean activation cross section is 377 mb. The neutron fluences are deduced from the $^{58}$Co activities measured on the irradiated Ni samples by the expression: $\Phi = 1.24(\pm 15\%) \times 10^{14}\,[A/\text{nCi}]/[M/\text{mg}]$ neutrons cm$^{-2}$ where $A$ and $M$ refer to the $^{58}$Co activities and the Ni sample masses, respectively. The same method was applied to measure fluences obtained in irradiations with liquid argon in the cryostat. Here, the Ni disks were locally glued on the tested samples. At 11 cm from the Be target, we measured $4.3(\pm 15\%) \times 10^{14}$ neutrons cm$^{-2}$ for an irradiation of 1.04 C of deuterons. For such a charge, the expected value in air (no cryostat) was $4.7(\pm 15\%) \times 10^{14}$ neutrons cm$^{-2}$. Using the FLUKA Monte Carlo program [7], we computed the neutron flux attenuation and distortion in the liquid argon cryostat (the mean free path of 6 MeV neutrons in liquid argon is 12.4 cm). At the 11 cm position (2 cm in liquid argon), we found almost no distortion of the energy spectrum and a flux global attenuation of 25%(±5%). The neutron flux reduction reaches 60% at 20 cm from the target. Given this, the predicted fluence in liquid argon (at 11 cm) was $3.6(\pm 15\%)\ 10^{14}$ neutrons cm$^{-2}$, which is compatible with the measured value quoted above.

The displacement damage power of a given neutron source is commonly characterized by a standard equivalent 1 MeV neutron fluence defined by [8]

$$\Phi_{eq} = M \int_{0.01\ \mathrm{MeV}}^{\infty} \Phi(E)\,\mathrm{d}E = \int_{0.01\ \mathrm{MeV}}^{\infty} \Phi(E)\frac{D(E)}{\overline{D}(1\ \mathrm{MeV})}\,\mathrm{d}E,$$

where $\Phi_{eq}$ is the equivalent 1 MeV neutron fluence, $\Phi(E)$ is the spectral fluence of the neutron source at the specified neutron energy $E$, $D(E)$ is the kerma displacement cross section of the considered material, $\overline{D}(1\ \mathrm{MeV})$ is the kerma displacement cross section averaged in the vicinity of 1 MeV, and $M$ is the equivalent factor.

$\overline{D}(1\ \mathrm{MeV})$ was computed according to the method described in Ref. [9] and the kerma displacement cross sections recently published for GaAs and Si [10]. The values which we found for Si and GaAs are $\overline{D}(1\ \mathrm{MeV}) =$ 92 MeV mb and 70 MeV mb, respectively. Putting these results in the expression above, we finally obtained $M = 1.5(\pm 0.2)$ and $M = 2.3(\pm 0.3)$ with respect to Si and GaAs.

## 4. Gamma dosimetry

This neutron source, as all fast neutron sources, is contaminated with some photon radiation. The precise relative contributions of photons and neutrons to the total dose are not easy to measure, especially if we consider that it is difficult to find dosimeters exclusively sensitive to a single type of radiation. Polymer–Alanine dosimeters (PADs) were essentially used to measure the angular distribution of the total dose [11,14]. The neutron to photon dose ratio was determined through the combined irradiation of two types of thermoluminescent dosimeters ($^6$LiF, $^7$LiF) [12,15].

After irradiation, the Alanine dosimeters were measured by means of a VARIAN-E3 ESR spectrometer. The dosimeters (4.8 mm in diameter, 30 mm long, trade name: *Elcugray*) were based on a homogeneous mixture of polymer and Alanine (33%–67% in weight). The dosimeters showed a good reproducibility and a very satisfactory dose response when they were calibrated with a $^{60}$Co source in the range of 10 to $5 \times 10^5$ Gy. The dose response of PADs depends on the radiation type: their relative sensitivity is close to 1 for photons and approximately 0.5 for fast neutrons. In addition, PADs have a neutron sensitivity threshold at around 1 MeV [13,16]. The Alanine dosimeters were mounted on a semi-circular support presenting a radius of 34.5 cm. The whole assembly was centered on the Be target so that the dosimeters effectively measured the angular distribution of the dose. They were irradiated with a total charge of deuterons of 43 mC.

Lithium fluoride dosimeters have many advantages as TLDs for photons, particularly due to their effective atomic number which is close to that of air. They also present a typical response to neutrons, since the lithium element has two stable isotopes ($^6$Li and $^7$Li) which have very different thermal neutron cross sections. To determine the neutron and photon sensitivity of both thermoluminescent dosimeters, a photon source of $^{60}$Co and a Pu–Be neutron source were used at CERN. The calibration was done using a high-density polyethylene moderator sphere of 5 in. of radius in order to slow down and thermalize the neutrons. This sphere provided a cavity into which the $^6$LiF–$^7$LiF dosimeter pairs were fitted practically without air gap. In this study we have used $3.2 \times 3.2 \times 0.98$ mm$^3$ chips of TLD-600 (95.6% $^6$Li, 4.4% $^7$Li) and TLD-700 (0.01% $^6$Li, 99.99% $^7$Li) from a single batch of Harshaw Chemical Co. At the irradiation facility, the sphere moderator containing the TLD dosimeters was placed at 50 cm from the Be target. They received an irradiation of 132 μC of deuterons. A standard annealing (1h at 400°C, then 2h at 100°C) was performed before the irradiation. Following the neutron exposure, a pre-readout annealing (25 mn at 85°C) was accomplished. For the readout, a Harshaw 2000 TLD reader was coupled to a Harshaw TLD glow-curve analyzer using a linear heating rate from room temperature to 280°C.

The results are shown in Table 1, where the dose rates are given at an angle of 0° and at 50 cm from the Be target for a deuteron beam current of 1 μA. The angular distribution of the dose rate, measured by Alanine dosimeters, is dis-

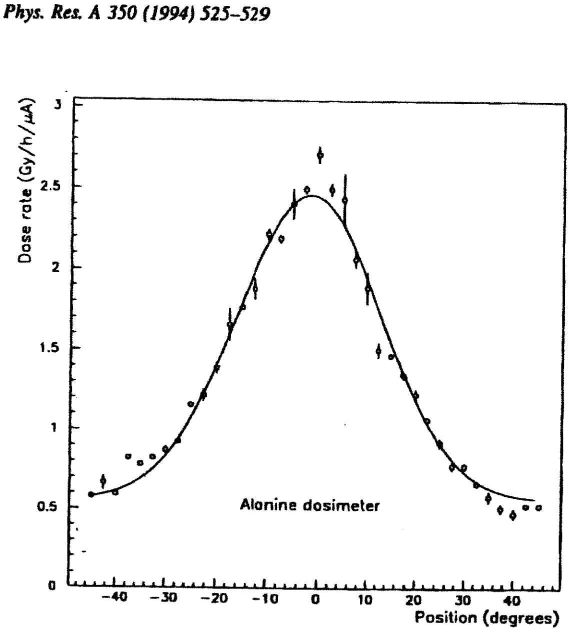

Fig. 5. Angular distribution of the total dose rate normalized at 50 cm from the Be target.

Table 1

Dose rates at 0° and 50 cm from the Be target

| | |
|---|---|
| $D_\gamma^{TLD}$ (Gy/h/μA) | 1.20 ± 0.03 |
| $D_n^{TLD}$ (Gy/h/μA) | 4.24 ± 0.19 |
| $D_{total}^{PAD}$ (Gy/h/μA) | 2.70 ± 0.05 |
| $D_n^{PAD}$ (Gy/h/μA) ($E_n \geq 1$ MeV) | 3.10 ± 0.16 |

played in Fig. 5. It shows a bell shape, close to a Gaussian. Photon and neutron doses were deduced from the TLD measurements ($D_{\gamma}^{\mathrm{TLD}}$ and $D_{\mathrm{n}}^{\mathrm{TLD}}$, respectively in Table 1). Since both dosimeter types have approximately the same response to photons, the neutron dose can as well be derived by subtracting the TLD photon dose from the total dose ($D_{\mathrm{total}}^{\mathrm{PAD}}$) given by the PAD dosimeters, and by doubling the resulting value to take into account the fast neutron relative sensitivity of PADs which is 0.5. The obtained dose is a factor 1.4 lower than the TLD result. The reason is that $^6$LiF TLDs are sensitive to all neutrons while PADs only react to neutrons above 1 MeV. These results show that the dose at 0° in the mixed radiation field at SARA comes for about 22% from photons and for about 78% from neutrons. In silicon, if the mean energy of the gamma spectrum is lower than 150 keV, the photon absorbed dose could be larger than the one obtained here, while for neutrons it strongly depends on the incident energy and is in general much lower. For instance, it is reduced by a factor of about 12.5 at 6 MeV [17]. Direct measurements using silicon diodes are currently under way, and their results will be communicated later. Nevertheless, we can already conclude that the photon dose is practically negligible when compared to the neutron fluence on the basis of their relative induced damage effects.

## 5. Conclusion

At the irradiation facility presented in this paper, neutron exposures at both cryogenic and room temperatures of front-end preamplifiers, mechanical parts, and of opto-electronic devices have been performed with fluences up to $4 \times 10^{14}$ neutrons cm$^{-2}$ on a fiducial area of $\sim 10$ cm$^2$.

This neutron source is now well characterized, and its photon contamination is low: 3.6 kGy for $2 \times 10^{14}$ neutrons cm$^{-2}$. The equivalent 1 MeV neutron fluence in Si (GaAs) is 1.5 (2.3) times larger than the real value measured by Ni activation. Because the thermal component of the neutron flux is small in this type of source, very little material activation is induced. This substantially facilitates the handling of the exposed samples.

Real-time measurements of the performance of the tested devices were made possible. They are of special interest when studying the evolution with the imparted neutron fluence of either the electronic noise of complex circuits, or the characteristics of transistors. Transient effects induced by neutron interactions in the active regions of the circuits may also be observed and investigated at this facility.

## Acknowledgements

The authors are grateful to A. Beteille, J. Collin, B. Guerre-Chaley, G. Laborie, M. Leménez, G. Mondin, J.F. Muraz, and P. Oustric for the valuable and dedicated work they have provided in building this facility, and acknowledge the determinant contribution of the SARA cyclotron operation crew. R. Brissot is to be thanked for the activation measurements of the Ni samples, and J. Bourges for performing the calibration irradiations of TLD dosimeters. One of us (C.L.) wants to thank the Killam Foundation and the Canada Council for their support. The authors wish to cordially thank M. Tavlet for the interest he has manifested concerning this work, and in general the CERN TIS division for lending some of the equipment used for the present measurements.

## References

[1] C.M. Logan et al., Nucl. Instr. and Meth. 145 (1977) 77;
L. Schmieder et al., Nucl. Instr. and Meth. A 256 (1987) 457;
H.J. Brede et al., Nucl. Instr. and Meth. A 274 (1989) 332;
M.J. Saltmarsh et al., Nucl. Instr. and Meth. 145 (1977) 81.
[2] CERN/LHCC/92-4 (1992).
[3] CERN/DRDC/90-31 (1990);
CERN/DRDC 92-40 (1992).
[4] R. Jean, J. Aucouturier and H. Leboutet, Annales de Radioélectricité 21 (1966) 122;
M. Lieuvin, 9th Int. Conf. on cyclotrons and their applications (Les éditions de physique, 1981, Les Ulis) p. 81.
[5] J. Alarja, Thesis 1988, Université Joseph Fourier de Grenoble - ISN 88.81.
[6] R.A. Cecil et al., Nucl. Instr. and Meth. 161 (1979) 439.
[7] P.A. Aarnio et al., CERN TIS-RP/106 (1984);
P.A. Aarnio et al., CERN TIS-RP/129 (1984);
P.A. Aarnio et al., CERN TIS-RP/190 (1987).
[8] G. Messenger and M. Ash, The effects of radiations on electronic systems (Van Nostrand Reinhold, New York, 1986), ISBN 0-442-25417-2.
[9] A. Namenson, E. Wolicki and G. Messenger, IEEE Trans. Nucl. Sci. NS-29 (1982) 1018.
[10] A.M. Ougouag et al., IEEE Trans. Nucl. Sci. NS-37 (1990) 2219.
[11] F. Coninckx and H. Schönbacher, Appl. Radiat. Isot. 44 (1993) 67.
[12] Y. Furuta and S. Tanaka, Nucl. Instr. and Meth. 104 (1972) 365.
[13] E. León Florián, H. Schönbacher and M. Tavlet, CERN/TIS-CFM/IR/93-03.
[14] F. Coninckx et al., Appl. Radiat. Isot. 40 (1989) 977.
[15] K. Becker, Solid State Dosimetry (CRC Press, 1973), ISBN 0-87819-046-5;
F. Attix et al., The dosimetry of ionizing radiation, Vol. II (Academic Press, 1987), ISBN 0-12-400402-4.
[16] Y. Katsumura et al., Radiat. Phys. Chem. 28 (1986) 337.
[17] M.H. Van de Voorde, CERN 69-12 (1969).

# Appendix D

## Nuclear Science Journal Vol. 31, No 5, p. 380-387, 1994.

NSJ Reprint

核子科學　第卅一卷第五期　中華民國八十三年十月

# 利用熱發光劑量計於SARA照射設施量測中子與光子劑量

# NEUTRON AND PHOTON DOSES MEASURED USING THERMOLUMINESCENT DOSIMETERS AT THE SARA IRRADIATION FACILITY

*Elena León Florián, Claude Leroy**
*University of Montreal, Montreal (Quebec)H3C 3J7, Canada*

*(Received April 19, 1994; Accepted June 29, 1994)*

The SARA facility at Grenoble provides the possibility to carry out neutron irradiation studies at both cryogenic and room temperatures. Neutrons are produced, at this facility, by collision of a 20 MeV deuteron beam on a thick Be target. This fast neutron source is unavoidably contaminated with a photon component. $^6$LiF and $^7$LiF dosimeters were used to determine the neutron and photon doses. The neutron and gamma dose components of the mixed radiation field were measured to be (78 ± 1)% and (22 ± 1)%, respectively. The photon contamination was found to be equivalent to 144 Gy for $8 \times 10^{12}$ neutrons/cm$^2$, at a deuteron beam current of 5 $\mu$A and at 50 cm from the enutron source.

Key words: neutron and photon dosimetry, dosimeters:
$^6$LiF, $^7$LiF, radiation damages

## INTRODUCTION

The future Large Hadron Collider (LHC) will be put into operation at the beginning of the next century at CERN (Centre Européen pour la Recherche Nucléaire), Geneva, Switzerland. It will bring protons into headon collisions at the centre-of-mass energy of 14.0 TeV.[1]

The conditions of operation of the LHC will create a high-level radiation environment with very large neutron fluences (up to $\approx 10^{13} - 10^{14}$ neutrons/cm$^2$/year) and doses ($\approx 10^4 - 10^6$ Gy/year). Such an environment will challenge the performances of the detectors and of their readout electronics. In order to assess the radiation hardness of these components, neutron irradiation facilities become, then, essential tools as they may reproduce the neutron fluences and doses expected at the LHC. Furthermore, the

---

* Killam fellow

foressen use of calorimeters using liquid argon,[2] as active medium, raises the question of radiation hardness at cryogenic temperatures.

The SARA(Service Accélérateur Rhône-Alpes) neutron facility installed at Grenoble allows irradiation studies both at room and cryogenic temperatures. It permits to expose various types of detectors, readout electronics and mechanical parts to high fluences of neutrons. The cryogenic conditions are provided by a 10 liters liquid argon cryostat.

A combination of thermoluminescent dosimeters (TLD), $^6$LiF and $^7$LiF, is used to determine the neutron and photon doses. The neutron energy spectrum is measured by a standard time-of-flight technique.

## BRIEF DESCRIPTION OF THE SARA FACILITY

A 3 mm thick beryllium target, 35 mm in diameter, is the neutron source, located at the extremity of one of the SARA beam lines. A 5 $\mu$A beam of 20 MeV deuterons is stopped on the Be disk, producing a high neutron flux by stripping reactions. The cryogenic environment, when needed, is provided by a liquid argon cryostat consisting of a cylindrical cryogenic vessel that may contain up to 10 liters of liquid argon.[3]

The neutron yield at 0° (i.e. in the beam direction) was measured with a NE213 scintillator detector, and was found equivalent to $4.8 \times 10^7$ ($\pm$ 15%) neutrons $(nA)^{-1}$ $Sr^{-1}$ $s^{-1}$ for a neutron energy threshold of 1 MeV. The shape of the neutron energy spectrum was determined by recording the time-of-flight (TOF) of neutrons. The mean neutron energy of the energy spectrum is 6 MeV. Further details may be found in Ref.(3).

## DOSIMETRY

The d + Be neutron source, as all fast neutron sources, is contaminated with some photon radiation. The precise neutron and photon relative contributions to the total dose are not easy to measure, specially considering that it is difficult to find dosimeters exclusively sensitive to a single type of radiation.

The use of TL phosphors, in a mixed field of neutrons and photons, has been proved to be successful. The phosphors which have been shown to have the highest thermal neutron responses are: $^6$LiF:Mg, Ti (main isotopic composition $^6$Li) known as TLD-600, $Li_2B_4O_7$:Mn and $CaSO_4$:Mn, $^6$Li. Because the unavoidable and variable photon contamination of the neutron beam, the use of TLDs in neutron dosimetry imposes to have also phosphors with low neutron sensitivity, such as $^7$LiF: Mg,Ti (main isitopic composition $^7$Li, known as TLD-700, $CaSO_4$: Dy and $CaSO_4$: Tm, in order to perform correct mixed field dosimetry measurements.[4-7]

Lithium fluoride dosimeters have many advantages as TLD for photons, particularly due to their effective atomic number which is close to that of the air. They also present typical responses to neutrons, since the lithium element has two stable isotopes $^6$Li and $^7$Li) which have very different thermal neutron cross sections.

Both thermoluminescent phosphors have a characteristic "glow curve", with its main dosimetric peak (peak 5) around 200 °C and its secondary peaks, 6 and 7, around 260 °C.

The neutron to photon dose ratio has been determined through the combination of two types of TLDs (TLD-600, TLD-700).[8-12] Chips of $3.2 \times 3.2 \times 0.98$ mm$^3$ of TLD-600 (approximately 95.6% $^6$LiF, 4.4% $^7$LiF) and TLD-700 (~0.01% 6LiF, ~99.99% $^7$LiF)from a single batch of Harshaw Chemical Co, were used in this study.

Several factors must be considered in neutron dosimetry: the photon contamination, fluctuations in the deuteron beam in the present case, and variation of the neutron energy dependence of the dosimeter material.

### Calibration of the Dosimeters

A photon source of $^{60}$Co and a Pu-Be neutron source [calibrated by means of secondary standard ionization chambers (LSO1, LS10) and Precision Long Counter (De Pangher PLC)[13]] were used, at CERN, to determine the photon and neutron sensitivity of both TLD, $^{6}$LiF and $^{7}$LiF. The calibration was done by using a high-density polyethylene moderator sphere. This choice was driven by the following consideration. If a thermal neutron detector is surrounded by increasing thickness of an efficient moderator (e.g. polyethylene), its response increases to some optimum value at which the production of thermal neutrons is maximum. Beyond this optimum thickness, the response declines because of increasing attenuation of the incident fast neutrons in the moderator. This "buildup", and subsequent reduction in response, depends upon the average energy of the incident neutron spectrum.

A sphere of 12.7 cm of radius was chosen. This value of the radius shows the highest response to neutrons with mean energies between 4 to 6 MeV (as it is the case for the Pu-Be and SARA neutron energy spectra). The same procedure was applied with $^{60}$Co, in order to reproduce the same experimental conditions and to include the photon attenuation within moderator in the calibration procedure. This sphere provided a cavity into which the $^{6}$LiF-$^{7}$LiF pairs were fitted practically without air gaps, in order to reduce the perturbations of the fluence in the medium.

An additional irradiation in free air with $^{60}$Co was done in order to compare the TLD's responses.

The thermoluminescent dosimeters were annealed before each irradiation through a thermal treatment of 400 °C for one hour, followed by two hours at 100 °C. Following the photon and neutron exposure, a pre-readout annealing was performed (85 °C for 25 min) to erase the low temperature peaks.

A Harshaw 2000 TLD reader, utilized for thermoluminescent (TL) evaluation at the Radioprotection Site & Services Section, at CERN, was coupled to a Harshaw TLD glow-curve analyzer model 2080, using a linear heating rate from room temperature to 280°C, at a rate of 7°C/s.

Three different calibration doses were used from both sources. Figure 1 shows the thermoluminescence response of peak 5(○) and peak 7(△) in nanocoulomb (nC) as a function of the calibration dose in milligray (mGy). The photon contamination from the Pu-Be neutron source (measured by Liquid Scintillator and GM counter[13]) was taken into account.

The neutron and photon sensitivities of peaks 5 and 7 for both TLDs were calculated by solving the equations:

$$\left\{ \begin{array}{c} R^{6}_{\gamma}(p)=S^{6}_{\gamma}(p)D_{\gamma} \\ R^{6}_{\gamma'+n}(p)=S^{6}_{\gamma'}(p)D_{\gamma'}+S^{6}_{n}(p)D_{n} \end{array} \right\} \qquad (1)$$

and

$$\left\{ \begin{array}{c} R^{7}_{\gamma}(p)=S^{7}_{\gamma}(p)D_{\gamma} \\ R^{7}_{\gamma'+n}(p)=S^{7}_{\gamma'}(p)D_{\gamma'}+S^{7}_{n}(p)D_{n} \end{array} \right\} \qquad (2)$$

with the approximation:

$$\begin{array}{c} S^{6}_{\gamma}(p)=S^{6}_{\gamma'}(p) \\ S^{7}_{\gamma}(p)=S^{7}_{\gamma'}(p) \end{array} \qquad (3)$$

where the superscripts 6 and 7 are for TLD-600 and TLD-700, respectively, and

$R^{6}_{\gamma}(p)$, $R^{7}_{\gamma}(p)$ = dosimeter responses to $^{60}$Co gamma source expressed in nC,

$R^{6}_{\gamma'+n}(p), R^{7}_{\gamma'+n}(p)$ = dosimeter responses to Pu-Be neutron source expressed in nC,

$S^{6}_{\gamma}(p), S^{7}_{\gamma}(p)$ = photon sensitivities expressed in nC/mGy,

$S^{6}_{\gamma'}(p), S^{7}_{\gamma'}(p)$ = photon contamination sensitivities expressed in nC/ mGy,

$S^{6}_{n}(p), S^{7}_{n}(p)$ = neutron sensitivities expressed in nC/mGy.

$D_{\gamma}$ = photon calibration absorbed dose expressed in mGy,

$D_{n}$ = neutron calibration absorbed dose expressed in mGy,

$p$ = peak number (5 and 7).

The solutions to Eqs. (1)and (2) are shown in Table 1. They are expressed as the mean value of the responses of the four samples for each TLD type and for each calibration dose. The given uncertainty corresponds to a one standard deviation.

After the determination of the sensitivites, the calibrated dosimeters could be placed in the mixed radiation field to measure its components.

## EXPERIMENT AT SARA

At the irradiation facility, the sphere moderator, containing the TLD-pairs (4 samples of each type), was located at 50 cm from the Be target. The samples were irradiated for 22392 s, with a mean current of 5.9 nA, in the beam direction.

The response of the dosimeters located in the mixed radiation field obeys the equations:

$$\left\{ \begin{array}{l} R^{6}(p)=S^{6}_{\gamma}(p)D_{\gamma}+S^{6}_{n}(p)D_{n} \\ R^{7}(p)=S^{7}_{\gamma}(p)D_{\gamma}+S^{7}_{n}(p)\ D_{n} \end{array} \right\} \qquad (4)$$

The chips were annealed at 400 °C for one hour, followed by two hours at 100 °C . The irradiated samples were post-annealed at 85 °C for 25 min, to eliminate the low temperature peaks.

A Harshaw 2000 TLD reader coupled to a Harshaw TLD glow-curve analyzer model 2080, was used for TL evaluation. The heating rate was 7 °C/s and the maximum read-out temperature was 280 °C.

## RESULTS

The gamma attenuation and the fast neutron thermalization effects in the sphere were

**Table 1** Neutron and $\gamma$ sensitivities for TLD-600 and TLD-700. [$S_{\gamma}$ (p) and $S_{n}$ (p) are the photon and neutron sensitivities of peak p, respectively.]

| | $S_{\gamma}(5)$ (nC/mGy) | $S_{\gamma}(7)$ (nC/mGy) | $S_{n}(5)$ (nC/mGy) | $S_{n}(7)$ (nC/mGy) |
|---|---|---|---|---|
| TLD-600 | 0.9988±0.047 | 0.0702±0.006 | 23.750±0.5145 | 11.563±1.544 |
| TLD-700 | 0.9952±0.007 | 0.0798±0.006 | 0.244±0.0004 | 0.0474±0.022 |

considered. Both effects were taken into account during the calibration in the radiation field of $^{60}$Co and Pu-Be, respectively. Small corrections were then applied, for the relative effective efficiencies given the fact that the energy spectra are different. In the case of photons, the variation of efficiency with energy was sufficiently small, so that this effect could be neglected. Typically, for energies between 1173 and 1332 keV from $^{60}$Co, the attenuation is corresponding to a 27% reduction, and given the low Z, this attenuation does not vary very much with energy.

To take into account the effect of the (n, $\gamma$ ) reaction produced with the hydrogen in the volume of the sphere, we have computed the ratio between the effective efficencies for both neutron spectra, as follows:

$$f = \left( \frac{\int_{Emin}^{Emax} \varepsilon(E)\,\phi_{Pu\text{-}Be}(E)}{\phi^{total}_{Pu\text{-}Be}} \right) \left( \frac{\int_{Emin}^{Emax} \varepsilon(E)\,\phi_{Sara}(E)}{\phi^{total}_{Sara}} \right)^{-1} \quad (5)$$

where:

$\varepsilon$ = Efficiency of the sphere over the neutron energy range in each case,

$\phi_{Pu\text{-}Be}$ = Differential flux for Pu-Be source,

$\phi_{Sara}$ = Differential flux for SARA facility,

$\phi^{total}_{Pu\text{-}Be}$ = Integral flux for Pu-Be source,

$\phi^{total}_{Sara}$ = Integral flux for SARA facility.

The $\varepsilon$ of the sphere was taken from Ref. (14). The ratio of the effective efficiencies was found to be 1.1.

In the process of the photon calibration of the TLDs, it was observed that peak 7 did not exhibit a linear dose response (uncertainties of the oreder of 8% to 50%) as shown in **Fig.1**, while peak 5, or main dosimetric peak for both TLDs, shows a very good linear dose response (uncertainties of the order of 1% to 5%).

For the TLDs, there exist differences between the thermoluminesecnce induced by photons and that induced by neutrons. In the interaction with neutrons, the thermoluminescence is induced by triton and $\alpha$ particles or $^{6}$Li and F recoiling nuclei in $^{6}$LiF (TLD-600), and by $^{7}$Li and F recoiling nuclei in $^{7}$LiF (TLD-700).

For the neutron calibration, differences are observed between TLD-600 and TLD-700 responses. The main difference is peak 7, around 260 ℃. TLD-700 does not show a well defined peak, while TLD-600 shows a pronounced peak that could be induced mainly by the $^{6}$Li(n, $\alpha$ )t reaction. Peak 5 of TLD-600 shows good linearity at all calibration doses, while peak 5 of TLD-700 is rather small, compared with that of the TLD-600's, due to its poor neutron sensitivity.

All these differences, discussed above, are expressed in the sensitivities shown in **Table 1**. In order to avoid all these discrepancies, related to peak 7, only peak 5 is taken into account for the calculations. This simplifies the solution to Eq. (4). Also the neutron sensitivity for TLD-700 ($S^{7}_{n}$(p)) is not taken into account, because it is negligible if compared with the neutron sensitivity of TLD-600 ($S^{6}_{n}$(p))and with its gamma sensitivity ($S^{7}_{\gamma}$ (p)). Then, the photon absorbed dose, $D_\gamma$ , is only expressed as a function of $S^{7}_{\gamma}$ (5) in Eq. (4)as:

$$D_\gamma = \frac{R^7(5)}{S^7_\gamma(5)} \quad (6)$$

while the neutron dose, Dn, is expressed as:

$$D_n = [R^6(5) - \frac{S^6_\gamma(5)}{S^7_\gamma(5)} R^7(5)][S^6_n(5)]^{-1} \quad (7)$$

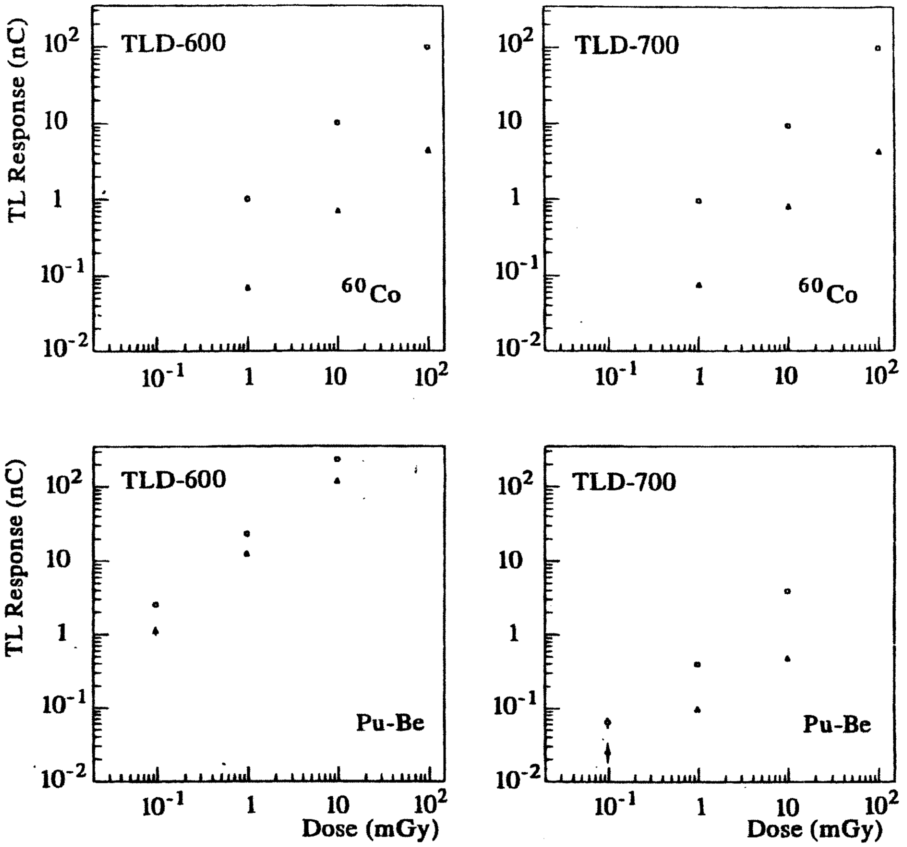

**Fig.1** Thermoluminescence response in nanocoulombs (nC) of TLD-600 and TLD-700 to different calibration doses in mGy from $^{60}$Co and Pu-Be [peak 5( ◦ ), peak 7(△)].

**Figure 2** shows the TLD glow-curves from irradiations performed at SARA. They confirm the poor neutron sensitivity of TLD-700 and, at the same time, the relative smallness of the photon component at that facility.

The dose rates, at 50 cm from the Be target and at an angle of 0° (i.e. in the beam direction), are shown in **Table 2** for a deuteron beam current of 1 $\mu$A. Thsese results show that the dose at 0°, in the mixed radiation field at SARA, comes for about (78 ± 1)% from neutrons and (22 ± 1)% from photons. The quoted errors are statistical.

The neutron fluence within one day of operation, at 50 cm from the source, is equivalent to 8 $\times 10^{12}$ n/cm$^{2}$ at full intensity (i.e. for a deuteron beam current of 5 $\mu$ A) corresponding to 509 Gy and 144 Gy of neutron and photon doses, respectively.

The measurement of doses, in Si and SiO$_2$ materials, is of great interest since silicon will be extensively used as active medium of detectors in the experiments to be performed at the LHC. Therefore, the doses must be measured in such material. However in this experiment, the doses are measured in TLD materials. Then, it becomes necessary to check how these doses will change for the Si and SiO$_2$ cases.

The neutron doses in Si and SiO$_2$ strongly depend on the neutron energy. At the neutron mean energy of 6 MeV, as measured at SARA, the neutron dose will decrease by a factor of 12.5 ± 2.5 compared with that measured in this experiment, according to Ref. (15) which takes into account the energy absorbed by Si and $SiO_2$ materials in Gy per unit of fluence, through the kinetic energy and the cross-section for elastic scattering of the neutrons.

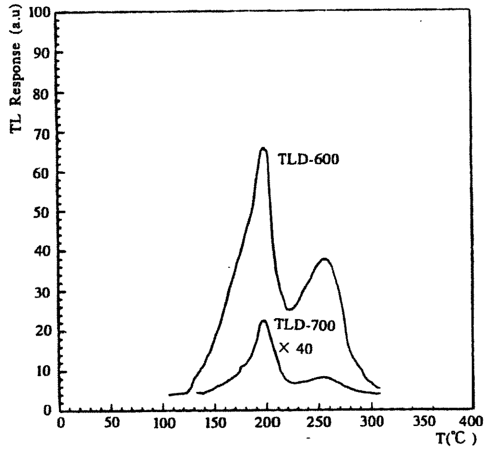

**Fig.2** Glow-curves in arbitrary units (a.u.) as function of the temperature in degrees centigrades, of TLD-600 and TLD-700 irradiated at SARA. [The original TLD-700 curve has been multiplied by a factor of 40.]

**Table 2** Dose rates at 0° and at 50cm from the Be target.

| $D_\gamma$(Gy/h/$\mu$A) | $D_n$(Gy/h/$\mu$A) |
|---|---|
| 1.20±0.03 | 4.24±0.19 |

The gamma spectrum at SARA is presently unknown, but its measurement is contemplated in a near future. However, some comments can be made prior to that measurement. The measured photon dose at SARA will be increased, by a factor of 1.6 ± 0.4 and 1.3 ± 0.2 for Si and $SiO_2$, respectively, if the photons have a mean energy of less than 150 keV. Above 150 keV and up to 8 MeV, the differences in Si and $SiO_2$ will be small, and the respective doses will be slightly modified by a factor of 0.96 ± 0.04 and 0.95 ± 0.02. At energies above 8 MeV, the doses will be increased by a factor 1.2 ± 0.05 in the case of Si and by a factor of 1.1 ± 0.06 in the case of $SiO_2$.

The above calculations are made according to Ref. (15) which takes into account the energy absorbed by Si and $SiO_2$ materials, through the mass energy absorption coefficient of each constituent in the material relatively to the mass energy absorption coefficient of air, at different photon energies. The corrections factors only serve as in dicators since large errors are attached to them.

## CONCLUSIONS

The combination of $^6$LiF (TLD-600) and $^7$LiF (TLD-700) dosimeters is a convenient method to measure gamma and neutron doses in a mixed radiation field.

A dosimetric characterization of the SARA facility has, then, been performed in view of radiation damage studies. The results showed that neutron and gamma dose components of the mixed radiation field were (78 ± 1)% and (22 ± 1)%, respectively. This makes a convenient "neutron source" for radiation damage studies, because its photon contamination is relatively small and found equivalent to 144 Gy for $8 \times 10^{12}$ n/cm$^2$ at full intensity (i.e for a deuteron beam current of 5 $\mu$A), and at 50 cm from the neutron source.

## ACKNOWLEDGEMENTS

The authors are grateful to J. Collot and co-workers, from Grenoble, for their help and discussions. The CERN TIS division is acknowledged for lending the equipments used for the present work. In the course of this work, we have enjoyed many discussions with C.

Furetta and J. Tuyn. Claude Leroy also wants to thank the Killam Foundation and the Canada Council for their support.

## REFERENCES

1. "Design Study of the Large Hadron Collider (LHC) — A multiparticle collider in the LEP tunnel", CERN 91-03, 1991.
2. Letter of intent of the ATLAS collaboration, CERN/LHCC/92-04.
3. J. Collot et al., "A neutron irradiation facility featuring cryogenic temperatures and dedicated to Large Hadron Collider detector design," Submitted for publication to Nuclear Instruments and Methods A.
4. F. Attix et al., *The Dosimetry of Ionizing Radiation,* Volume II, Academic Press, Inc., 1987, ISBN 0-12-4004024.
5. K. Becker, *Solids State Dosimetry,* CRC Press, Inc., 1973, ISBN 0-87819-046-5.
6. Edited by N. Holm and R.J. Berry, Manual on radiation dosimetry, Marcel Dekker, Inc., 1970.
7. K. Mahesh et al., *Thermoluminescence in Solids and Its Applications,* Nuclear Technology Publishing, Ashford, UK (1989).
8. Y. Furuta et al., "Response of $^6$LiF and $^7$LiF thermoluminescence dosimeter to fast neutrons," *Nuclear Instruments and Methods,* 104, 365-374 (1972).
9. Larsson et al., "The response of LiF dosimeters in the radiation field of a 14 MeV neutron generator," *Nuclear Instruments and Methods,* 175, 189-190 (1980).
10. M. Sohan et al., "Local energy transfer to TLDs by neutrons and photons," *Nuclear Instruments and Methods,* 175, 31-33 (1980).
11. Tien-Ko Wang, "On the use of TLD for gamma ray dosimetry evaluation in mixed fast neutron and gamma ray fields," *Radiation Protection Dosimetry* Vol. 33, No.1/4 pp 359-363(1990).
12. E. León Florián et al., "Use of thermoluminescent dosimeters in a mixed radiation field of an irradiation facility at CERN," *Nuclear Science Journal,* Vol. 30, No.5 pp. 331-338 (1993), Chung Hua Nuclear Society, R.O.C.
13. R. C. Raffnsoe: Yearly source comparison 1990, TIS-RP-CD/90-03(1990).
14. R. Sanna, "Thirt one group response matrices for the multisphere neutron spectrometer over the energy range thermal to 400MeV", HASL-267, United States Atomic Energy Commission, New York, N.Y. 10014(1973).
15. H. Van de Voorde, "Effects of radiation on materials and components", CERN 69-12, 1969.

# Appendix E

## Nuclear Physics B 44,
## p.503–509, 1995.

ELSEVIER

Nuclear Physics B (Proc. Suppl.) 44 (1995) 503–509

NUCLEAR PHYSICS B
PROCEEDINGS
SUPPLEMENTS

# Fluence and dosimetric measurements for a $\pi^{\pm}$ irradiation facility

RD2 Collaboration

C. Furetta, S.J. Bates, M. Glaser, F. Lemeilleur, M. Tavlet[a]
E. León-Florián, C. Leroy[b]

[a]CERN, Geneva, Switzerland

[b]University of Montreal, Montreal, Canada

This paper briefly describes the pion irradiation facility used by the SIRAD (Silicon Radiation) Collaboration in mid-1994 at the Paul Scherrer Institute (PSI) in Villigen, Switzerland, and reports the fluence measurements carried out with the Al activation technique during silicon detector irradiations. Calibration factors were determined as a ratio between the fluence and the number of counts from an ionization chamber. Some dosimetric measurements were also performed using alanine and thermoluminescent dosimeters, which allowed the $\pi$ and the $\gamma$ dose rates to be determined. $^{115}$In activation was also used to determine the neutron contamination around the $\pi$-beam.

## 1. INTRODUCTION

The Large Hadron Collider (LHC), operational by the beginning of the next century at CERN, will bring protons into head-on collisions at a centre of mass energy of 14 TeV with an expected peak luminosity of $1.7 \times 10^{34}$ cm$^{-2}$ sec$^{-1}$. The LHC operating conditions will create a high-level radiation environment producing radiation damage in detectors and their associated electronic components. Silicon is expected to be used as the active medium for several detectors in the future LHC experiments. As a consequence, detailed studies are under way to understand the behaviour of the silicon detectors in such an adverse environment.

The irradiation modifies the crystalline structure of the silicon detectors as well as their electrical characteristics. The charge collection efficiency is reduced and the leakage current increases. The effective doping concentration also changes. Generally speaking, the degradation phenomena can be described in terms of minority carrier lifetime reduction, acceptor creation and carrier mobility reduction.

The establishment of a correlation between damage and irradiation primarly requires a good understanding of the environmental conditions. This knowledge is provided by a precise determination of the particle fluxes and/or absorbed doses involved during irradiation of the silicon detectors. The aim of this paper is to give a brief description of the pion irradiation facility used by the SIRAD (Silicon Radiation) collaboration in mid-1994 at the Paul Scherrer Institute (PSI), Villigen, and to present the results of the fluence and dosimetric measurements.

## 2. EXPERIMENTAL SET-UP

The high intensity PSI pion beam (II-E1) has a momentum range from 100 to 450 MeV/$c$. Pions, produced by the collision of the cyclotron proton beam with a graphite target, are guided via a beam line down to the irradiation zone. The maximum proton current of the cyclotron is $\sim 800\ \mu$A. After the production target, the pion beam is contaminated with a large number of protons filtered by means of graphite plate absorbers. Proton interactions in graphite produce a yield of neutrons which must be measured. The lepton contamination of the pion beam at the irradiation position (estimated to be $\sim 10\%$) is expected to induce damage in silicon of at least one order of magnitude lower than that of hadrons [1]. Therefore, the damaging effect of leptons can be safely neglected to a first approximation.

The irradiation position is located $\sim 1$ m downstream of the last quadrupole magnet at a height of $\sim 1.5$ m. A sketch of the experimental set up

0920-5632/95/$09.50
*SSDI* 0920-5632(95)00576-5

Table 1
List of the activation detectors used during the pion irradiations and their main characteristics

| ACTIVATION DETECTORS | | | | | | |
|---|---|---|---|---|---|---|
| MATERIAL | AREA ($mm^2$) | THICKNESS (mm) | REACTION | HALF LIFE ($T_{1/2}$) | $\gamma$ EMISSION | RADIATION DETECTED |
| Aluminium | 10 x 10<br>8 x 8<br>5 x 5<br>6 x 12 | 0.1<br>0.1<br>0.1<br>0.1 | $^{27}AL(\pi^{\pm},xN)^{24}NA$ | 15.06 h | 1369 keV (99%) | $\pi$ |
| Carbon | 10 x 10 | 1 | $^{12}C(\pi^{\pm},xN)^{11}C$ | 20.39 min | 511 keV (200%) | $\pi$ |
| Indium | 28.3 | 0.3 | $^{115}In(n,n')^{115m}In$<br>$^{115}In(n,\gamma)^{116m}In$ | 4.50 h<br>54.0 min | 336 keV (46%)<br>417 keV (29%)<br>1097 keV (56%)<br>1294 keV (85%) | n(0.5–14.0 MeV)<br>thermal neutrons |

is shown in Fig. 1. An ionizing chamber, an X–Y chamber and a luminescent screen were used to monitor the beam. The ionization chamber was present during the whole period of irradiation and the digitized induced current, $N_{ic}$, (proportional to the total pion beam intensity) was used to record the fluence during the irradiation periods (see Section 5). The X–Y chamber was moved along the beam direction to measure the vertical and horizontal FWHM beam profile at each position of irradiation. The transverse beam density, expressed as $1/[(FWHM)_H \cdot (FWHM)_V]$, was then calculated at each position. Figure 2 shows the transverse $\pi^+$ beam profile and density, as a function of longitudinal position, obtained at 350 MeV/*c*.

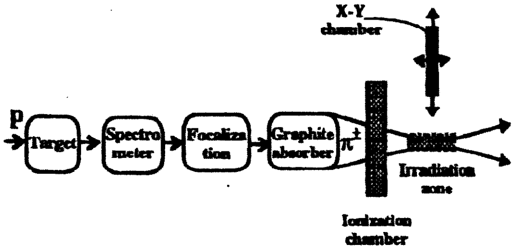

Figure 1. Diagram of the beam and irradiation set-up

The technique of activation was chosen to measure the fluences during the irradiations. The activation detectors and their characteristics are summarized in Table 1. Table 2 lists the type of dosimeters used to estimate gamma and neutron production during the $\pi^+$ irradiation.

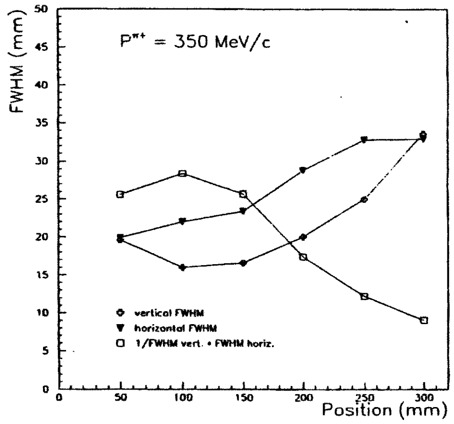

Figure 2. Transverse $\pi^+$ beam profile and density versus longitudinal position at a momentum of 350 MeV/*c*

Figure 3 shows the respective positions of the activation detectors and the dosimeters in the irradiation box.

The activation detectors were Aluminium, Carbon and Indium foils, mounted in cardboard frames. The Al foils had the same area as the detectors to be irradiated and were located in the irradiation box between the groups of silicon detectors. The box was mounted on a table movable in three dimensions (x, y, z) to optimize its position in the beam.

Table 2
List of dosimeters used during the pion irradiation and their main characteristics

| DOSIMETERS | | | | | | |
|---|---|---|---|---|---|---|
| MATERIAL | AREA ($mm^2$) | THICKNESS (mm) | PHYSICAL EFFECT | TECHNIQUE OF MEASUREMENT | MEASURED QUANTITY | RADIATION DETECTED |
| LiF:Mg, Ti (TLD-700) | 9 | 0.9 | Electron excitation | Heating | Light | $\gamma$ |
| Alanine (PAD) | 144 | Ø4.8 | Free radical production | Electron Spin Resonance | Free radical number | $\pi$ |

Thermoluminescent (TLD) and polymer-alanine (PAD) dosimeters were inserted in plastic bags. The TLDs were located out of the beam line because this type of dosimeter is not suitable for high-level dosimetry (the linearity of the absorbed dose is only valid up to about 1 Gy); on the contrary the PADs were positioned in the beam because their dose range is linear up to about 50 kGy. The dose rate due to pions is estimated to be of the order of 180 Gy/h in water and about one order of magnitude lower in silicon.

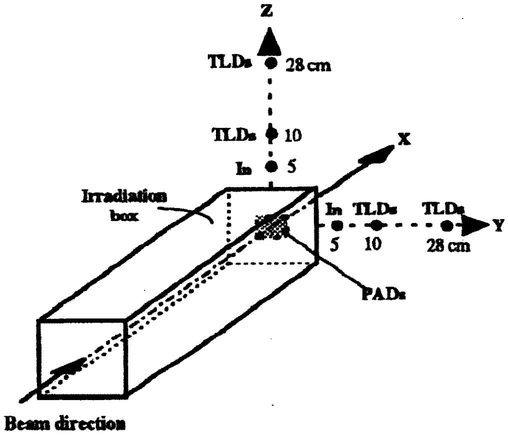

Figure 3. Diagram of the irradiation box and the dosimeter positions

Before irradiation of the silicon detectors, a range of photographic films were exposed in the beam in order to determine the exact position of the beam spot for aligning the irradiation box. The films were fixed at the front and the rear of the box.

## 3. FLUENCE MEASUREMENTS

The fluence measurement required is the integrated flux of specific particles over the irradiation time. The fluence can be determined from the activity, A, induced in the given materials, and a brief description of the techniques is given below.

### 3.1. Mathematical treatment

The activity of the irradiated material at the end of the irradiation is given by:

$$A = \varphi \cdot \sigma \cdot N_0[1 - \exp(-\lambda t_i)] \quad , \qquad (1)$$

where $\varphi$ is the particle flux, $\sigma$ is the activation cross-section, and $N_0 = N \cdot P \cdot W/M$, is the number of atoms in the target element, with $N = 6.022 \times 10^{23}$, the Avogadro constant, P the isotopic abundance, M the atomic mass of target element, and W the weight of target element.

The expression in brackets is the correction factor for decay during irradiation, where $t_i$ is the irradiation time, $\lambda = \ln 2/T_{1/2}$ is the decay constant, and $T_{1/2}$ is the half-life of the radioactive nuclei.

The saturation activity, $A_\infty$, is the asymptotic value achieved, within 1%, at about seven times the half-life:

$$A_\infty = \varphi \cdot \sigma \cdot N_0 \ . \qquad (2)$$

As the sample activity is measured by a spectrometer at a time $t_e$ (elapsed time) after the end of the irradiation and during a time $t_c$ (counting time), two more factors have to be taken into account:

a) a factor depending on the elapsed time $t_e$:

$$\exp\left(-\lambda \cdot t_e\right) \quad , \qquad (3)$$

b) a factor depending on the counting time $t_c$:

$$\overline{A} \cdot \lambda \cdot t_c / [1 - \exp(-\lambda \cdot t_c)] \quad , \tag{4}$$

where $\overline{A}$, the activity measured by the spectrometer, is given by:

$$\overline{A} = \text{counts}/[t_c \cdot \eta\% \cdot \varepsilon\%] \quad , \tag{5}$$

$\eta$ being the emission probability and $\varepsilon$ the detection efficiency of the HPGe(p)–$\gamma$ spectrometer.

Combining all the previous expressions:

$$\begin{aligned} A_\infty \quad = \quad & \overline{A} \cdot \lambda \cdot t_c \cdot \exp(\lambda \cdot t_e) / \\ & \{[1 - \exp(-\lambda \cdot d_c)] \\ & [1 - \exp(-\lambda \cdot t_i)]\} \ . \end{aligned} \tag{6}$$

The flux expression is then given by

$$\begin{aligned} \varphi \quad = \quad & A \cdot \lambda \cdot t_c \cdot \exp(\lambda \cdot t_e) \cdot M / \\ & \{N_A \cdot P \cdot W \cdot \sigma \cdot \\ & [1 - \exp(-\lambda \cdot t_c)] \\ & [1 - \exp(-\lambda \cdot t_i)]\} \end{aligned} \tag{7}$$

and the fluence is the flux times the irradiation time $t_i$, hence

$$\Phi = \varphi \cdot t_i \ . \tag{8}$$

### 3.2. Fluence from Aluminium foils

The production of $^{24}$Na from $^{27}$Al [$^{27}$Al($\pi^{\pm}$, xN)$^{24}$Na] was used to measure the fluence of $\pi^{+}$ and $\pi^{-}$ in the energy range of about 50–350 MeV. $^{24}$Na decays through $\beta$ and $\gamma$ emissions. The $^{24}$Na activities were measured by a HPGe(p)–$\gamma$ spectrometer selecting the 1369 keV $\gamma$-rays with a resolution of about 2.0 keV at FWHM. The collected spectra were computed by the INTERGAMMA code, giving sample activity. The activities at saturation and, then, the corresponding fluences, were calculated by using Eqs. (7) and (8) with the reaction cross-sections obtained from Ref. [2].

### 3.3. Fluence from Carbon foils

Graphite foils were used to provide a cross-check of the pion fluence values obtained by Al foils. The graphite foils were used in tandem with Al foils. The activity of $^{11}$C produced by the $^{12}$C($\pi^{\pm}$,xN)$^{11}$C reaction was measured by detecting the 511 keV $\gamma$-ray decay with the spectrometer mentioned above. The cross-section is taken from Ref. [2]. Due to the frequent beam stops and short half life of $^{11}$C (20.39 minutes), graphite foils were not routinely used. The results obtained with Al and C were in agreement to within 5%.

### 3.4. Fluence from Indium

$^{115}$In disc shaped samples were used to detect the neutron contamination around the pion beam.

The neutron activation technique based on the $^{115}$In(n, n′)$^{115}$In$^m$ reaction is well suited for fluence measurements of neutrons with an energy above 500 keV for several reasons:

- the activation cross-section is large, and well known [3];
- the threshold at about 500 keV prevents activation by low-energy neutrons;
- the half-life of 4.50 hours is convenient for the periods of irradiation considered;
- the activity of $^{115}$In$^m$ is determined by its 336 keV gamma ray decay. The technique based on the $^{115}$In(n, $\gamma$)$^{116}$In$^m$ reaction has been also used to detect thermal neutrons. The activity of $^{116}$In$^m$ is measured by the detection of 416.9, 1097.3 and 1293.5 keV gamma rays.

The $^{115}$In discs were located on the Y and Z axis, at 5 cm from the beam line (See Fig. 3).

## 4. DOSIMETRIC MEASUREMENTS

Dosimetric measurements were performed to evaluate the pion doses in the beam and the gamma doses around it.

### 4.1. Thermoluminescent dosimeters (TLD)

Thermoluminescent materials have the capability of storing part of the energy absorbed with sufficient stability when exposed to a radiation field. Impurities intentionally added to a host lattice create new energy levels within the band gap between the valence and conduction bands. These new levels can act as traps for electrons and/or holes created during material irradiation, preventing prompt recombination. If after irradiation the material is heated up to an adequately high temperature, the trapped charges will receive sufficient thermal energy to be liberated.

This liberation provokes recombinations that restore the pre-irradiation lattice conditions. The energy liberated upon heating (thermoluminescence measurement or readout) is converted into light proportional to the dose absorbed during irradiation.

The TLDs used in the present experiment are based on lithium fluoride activated by Mg and Ti. They are produced by Harshaw Co. (USA) in solid form (ribbon) with the commercial name TLD-700. They were used to estimate the gamma ray contamination during the pion irradiations. The dimensions of the TLDs are $3 \times 3 \times 0.9$ mm$^3$. They were located in two different positions along both the Y and Z axes, at 10 and 28 cm from the beam direction, as shown in Fig. 3.

### 4.2. Polymer-Alanine Dosimeters (PAD)

In Electron Spin Resonance (ESR) dosimetry, the ionizing radiation leads to the production of paramagnetic centres, which give rise to a characteristic ESR signal. The number of paramagnetic centres, and in turn the amplitude of the corresponding ESR signal, is proportional to the dose. In the present case, standard polymer-alanine dosimeters (PAD, 4.8 mm in diameter and 30 mm long) are cut from the Elcugray cable which uses ethylene-propylene rubber as a binder. The PADs were positioned on the back of the irradiation box to measure the pion dose. After irradiation they were read out by the ESR technique on a Varian E-3 spectrometer.

## 5. RESULTS

Because the pion beam size varied strongly along the beam direction (Fig. 2), several Al foils were used to measure the fluence along the irradiation box. During the irradiation runs, the Al foils were located at the relevant positions in front of each group of silicon detectors. The fluence obtained from these foils can therefore be used directly as a measure of the fluence received by the silicon detectors. To get more accurate measurements, the foils to be counted were sandwiched between two foils of the same material so that recoils leaving the foil are replaced by recoils from the cover foils. It must be noted that the duration of an irradiation is calculated from the start and stop times and does not take into account periods when the beam was off. In fact, the beam-off periods were always very short compared with the half-life of $^{24}$Na (15 hours), so that no correction to the flux calculations was necessary. Figure 4 shows the flux normalized to the cyclotron intensity as a function of the position along the beam line for various $\pi^+$ momenta. The maximum flux was obtained in the region of 300–350 MeV/$c$. The momentum of 350 MeV/$c$ was selected for the high fluence accumulation runs. This momentum is close to the energy of the $\Delta$ resonance, which could enhance the damage induced by pions in silicon [4, 5].

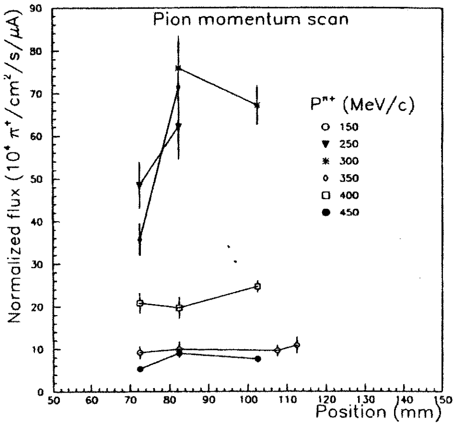

Figure 4. Normalized flux as a function of the irradiation positions along the beam line at different pion momenta

### 5.1. $\pi^+$ beam profile at 350 MeV/c

Figure 5 shows the average flux as measured with Al foils for the 350 MeV beam as a function of various positions along the irradiation box. The flux strongly decreases from the front to the back of the box. The beam density obtained from the XY profile chamber (see section 2) is shown in the same figure. Both measurements are in very good agreement.

### 5.2. Pion fluence calibration during irradiation runs

The pion accumulation runs were performed at a momentum of 350 MeV/$c$, up to fluences of $\sim 10^{14}$ cm$^{-2}$ for $\pi^+$ and $10^{13}$ cm$^{-2}$ for $\pi^-$.

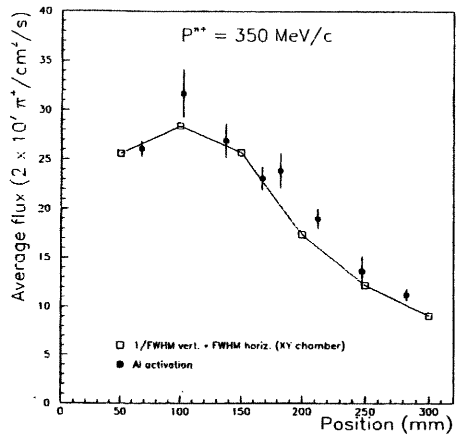

Figure 5. Comparison of the longitudinal beam profile at a momentum of 350 MeV/c as obtained by the X–Y chamber and by the Al activation

It would not have been possible to have an aluminium foil in front of each irradiated silicon detector due to the amount of time needed for activity measurements. Therefore, four aluminium runs were performed during the $\pi^+$ accumulation period. For each run, Al foils of the same area were located in front of each group of silicon detectors. The Al-runs were then used to calibrate the ionization chamber (see Chapter 2). Figure 6 shows an example of the fluence measured with the Al foils as a function of the ionization chamber counts for two different positions in the irradiation box. The points were fitted and a calibration factor **k** was obtained at a given position in the irradiation box. The calibration factors can then be used to calculate the fluence, Φ, received by any silicon detector irradiated during the accumulation runs using the equation

$$k_j = \Phi_j / N_{ic} \;, \tag{9}$$

where j denotes the longitudinal positions of the detectors, $\Phi_j$ is the fluence at the position j received by each detector, and $N_{ic}$ is the number of counts from the ionization chamber.

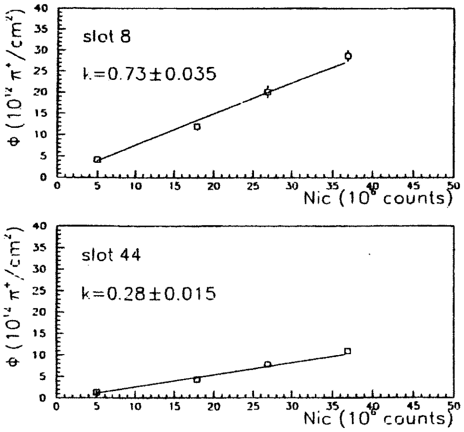

Figure 6. Examples of calibration factors deduced from Al fluence measurements versus ionization chamber counts

Figure 7 shows the flux as a function of the Si detector irradiation position in the box, for the four succesive runs.

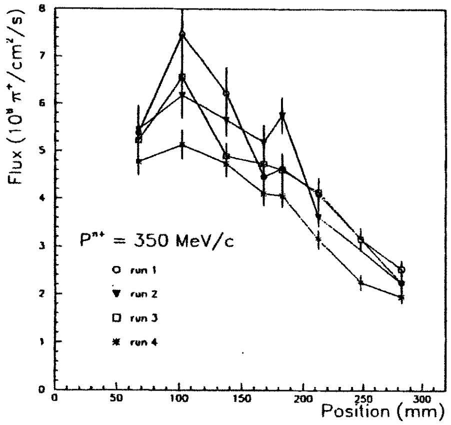

Figure 7. Positive $\pi$ flux as a function of Si-detector irradiation positions for succesive runs

A similar calibration of the ionization chamber was performed for the negative pion accumulation run.

### 5.3. Results from Indium activation

The activation of $^{115}$In allowed the neutron contamination around the positive pion beam line to be measured. The activation of $^{115}$In produces two isotopes (see Table 1). Considering the neutron energy at which the two nuclear reactions can be produced and using the corresponding cross-sections, the thermal and fast neutron contaminations around the $\pi^+$ beam were estimated.

At 5 cm from the beam, the thermal and fast neutron contaminations varied respectively from 0.3 to 0.8% and from 0.2 to 0.5% of the positive pion flux.

### 5.4. Results from the dosimetry

The 350 MeV/$c$ $\pi^+$ dose rate measured by the Alanine dosimeters (PAD) located in the beam was 337 ± 72 Gy/h. The thermoluminescent dosimeters (TLD), measured the $\gamma$ dose. At 10 cm from the beam axis a dose rate of $5.0 \pm 0.8$ Gy/h was obtained. At 28 cm the dose rate fell to $0.70 \pm 0.03$ Gy/h.

## 6. CONCLUSIONS

The Aluminium activation technique permitted the $\pi^\pm$ fluences to be measured to within 5%. As a result, the ionization chamber was calibrated to measure fluence as a function of the beam intensity. The Al activation fluence measurements were extensively used by the SIRAD collaboration at PSI. The use of different types of radiation detection materials, such as Indium, thermoluminescent and alanine dosimeters, was very useful to determine the n and $\gamma$ contamination during the pion irradiation runs. With the Indium, a maximum neutron contamination of 0.8% was estimated; the thermoluminescent detectors (TLD) gave a $\gamma$ dose rate of 5 Gy/h at 10 cm and 0.7 Gy/h at 28 cm from the beam axis. Finally, the combined use of various kinds of dosimeters proved to be necessary to properly characterize the beam and its environment.

## ACKNOWLEDGEMENTS

The authors wish to thank PSI for providing beam time (R. Horisberger), beam set-up (R. Frosch), beam diagnostic instrumentation and installation (K. Gabathuler) and gamma spectrometry (A. Janett).

## REFERENCES

1. A. Van Ginneken, Tech. Rep. FN-522, Fermi Nat. Acc. Lab. (1989).
2. Landolt-Bornstein, Production of Radionuclides at Intermediate Energies, Gr. I, Vol. 13, Subvol. D, E (1994).
3. V. McLane, C.L. Dunford, P.F. Rose, Neutron Cross Sections, Vol. 2 (1987) N.Y., Academic Press, Inc.
4. M. Huhtinen and P. Aarnio, Nucl. Instrum. Methods **A335** (1993) 580.
5. Review of Particle Properties, Phys. Rev. **D45** Part II (1992), S1.

# Appendix F

# IEEE Transactions on Nuclear Science, IEEE Catalog Number 95TH8147, p.101–107, 1995.

# Particle Contamination Measurements around Hadron Beams used for Irradiation of Silicon Detectors for the LHC.

Elena León-Florián and Claude Leroy
University of Montreal, Montreal (Quebec) H3C 3J7, Canada

## *Abstract*

While LHC silicon detector prototypes were irradiated with pions and protons for radiation damage studies at Villigen-**PSI** and CERN-**PS**, the nearby beam contaminations by neutrons, protons and photons was measured by means of various activation foils and dosimeters. The estimated fluxes due to neutron and proton contamination are a few percents of the pion and proton fluxes given to the silicon detectors. In all cases, the low energy neutron component is found to be dominant.

## I. INTRODUCTION

Detectors and associated electronic components used in high-level radiation environment are subject to radiation damage. An example of such an environment is provided by the Large Hadron Collider (LHC), where head-on collisions of 7 TeV protons at a peak luminosity of $1.0 \times 10^{34}\,\mathrm{cm}^{-2}\,\mathrm{s}^{-1}$ will produce high fluences of particles. Irradiation tests will be performed at dedicated facilities to evaluate the damage to be expected at LHC. The measurement of the particle fluences and absorbed doses available at these facilities is necessary to establish a correlation between the nature of damage inflected to a given material and the type and level of irradiation it has been exposed to.

Two charged beams were used to study the radiation damage effects in silicon detectors: a high intensity beam of pions ($\pi$E1) at the Paul Scherrer Institute (**PSI**-Villigen) with a particle momentum of 350 MeV/c and a beam of protons at the Proton Synchrotron (**PS**) at CERN with a particle momentum of 24 GeV/c.

The unavoidable contamination of these sources by other types of particles, generated by the interaction of the pion and proton beams with the Si samples and surrounding materials, yields a situation of mixed fields that contributes additional damage to the silicon samples under study.

For the first time, a direct confirmation of this contribution is obtained with a simultaneous irradiation of Si detectors and characterization of the radiation field. The particle fluxes and absorbed doses near the beam were measured with alanine, LiF dosimeters and activation of metal foils (via nuclear activation reaction in In, Co and Ni). The pion and proton fluxes on the beam axis were measured by activation of Al and C foils.

## II. FACILITIES

### *A. PSI*

The $\pi$E1 beam line at **PSI** [1] supplies high intensity pion and muon beams. Pions are produced in the collision of the intense proton beam (maximum current of 800 $\mu$A) with a graphite target. They come out with momenta ranging from 100 to 450 MeV/c and are guided via a beam line down to the irradiation casemate. After the graphite target, the presence of a large number of protons is eliminated by means of graphite plate absorbers.

At the irradiation position, the pion beam is polluted by muons and electrons. Damage in silicon by leptons can be neglected, being one order of magnitude lower compared with damage inflicted by hadrons [2].

### *B. PS*

The **PS** is at the heart of the complex of the CERN accelerators. It provides dedicated beams to test detectors in a variety of conditions, such as the T7, T9, T10 and T11 test beams available in the **PS** East Hall. The **PS** measurements reported in this article were performed using the T7 beam line. It offers a primary beam with a momentum of 24 GeV/c with from one to two spills of protons delivered to the irradiation zone per supercycle. A spill consists of a burst of protons for typically 400 ns. Two consecutive spills are separated by at least 2.4 s during a 14.4 s supercycle. The maximum proton intensity is $2\times10^{11}$ protons per spill. No beam pollution was expected since the beam is coming directly from the synchrotron.

0-7803-3093-5/96$5.00©1996

## III. FLUX AND DOSE

### A. *Set-Up of the Experiments*

At **PSI**, the irradiation position was located 1 m downstream of the last quadrupole magnet. The pion momentum was 350 MeV/c. At **PS**, the irradiation position was about 3 m downstream of the vacuum pipe and the proton momentum was 24 GeV/c.

An ionization chamber, a X-Y chamber and a luminescent screen were used to monitor both the $\pi^+$ beam at the **PSI** and the $p$ beam at **PS**. The Si samples were mounted inside square cardboard frames. These frames were stacked, normal to the beam direction, in a box volume of $5 \times 5 \times 25$ cm$^3$. At the same time, aluminium foils cut to the same shape as the Si samples were interleaved with the tested material. The box was mounted on a table, mobile along the three space axes ($x$,$y$,$z$) in order to optimize its position in the beam.

#### 1) *Neutron Flux Measurements:*

Indium (In), Cobalt (Co) and Nickel (Ni) activation foils [3] were placed at different positions along both transverse axes for measuring the neutron contamination near the $\pi^+$ and $p$ beams. The positions are shown in Fig. 1 and Fig. 2. Indium activation foils were chosen because of their very large cross sections for neutrons of thermal energies up to a few MeV that allows to quantify this particular component of the contamination responsible for a large part of damage to Si. To complete the understanding of the neutron spectrum of the contamination, Ni and Co foils were used with their dominant activation cross section at neutron energies of a few MeV and a few tens of MeV, respectively.

#### 2) *Proton Flux Measurements:*

Ni and Co foils were used to quantify the proton contribution at **PSI** and at **PS**, since they present some reactions that are exclusively proton reactions. The positions of the foils are shown in Fig. 1 and Fig. 2.

#### 3) *Photon and Hadron Dose Measurements:*

LiF:Mg,Ti (TLD-700) dosimeters were used to measure the photon absorbed doses near the $\pi^+$ beam, as shown in Fig. 1. TLD-700 was selected, with its main component of $^7$Li of high photon sensitivity and negligible neutron sensitivity. Polymer alanine dosimeters (PAD) were placed at the rear of the box in order to measure the pion and proton absorbed doses in alanine in the beam line. They are the sole dosimeters which provide linearity in a very large dose range (up to 30 kGy) [4].

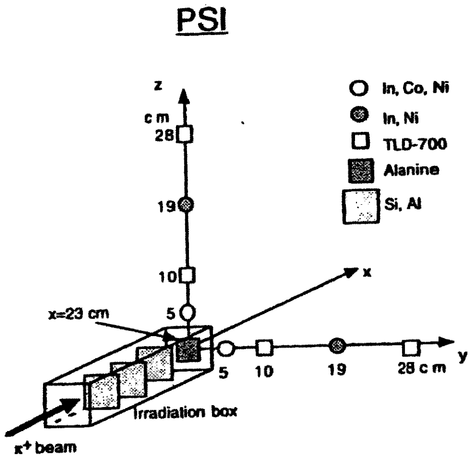

Figure 1: Set-up of the experiment at **PSI**

## IV. RESULTS

The activation of aluminium foils by $^{27}$Al($\pi^+$,xN)$^{24}$Na and $^{27}$Al($p$,3$pn$)$^{24}$Na reactions allowed the measurement of the pion and proton fluences. Graphite foils, activated by $^{12}$C($\pi^+$,$\pi$N)$^{11}$C and $^{12}$C($p$,$pn$)$^{11}$C reactions, were used to provide a cross-check of the pion and proton fluences given by the Al foils. The cross sections for these nuclear reactions in Al and C were taken from [5, 6] for pions and from [7] for protons. The results obtained with Al and C foils were in agreement within 5 %.

The pion fluxes measured at **PSI** by means of Al foils along the irradiation box are shown in Fig. 3, the calculated pion dose–rate in silicon at the maximum pion flux is (691.1 ± 52.3) Gy/h.

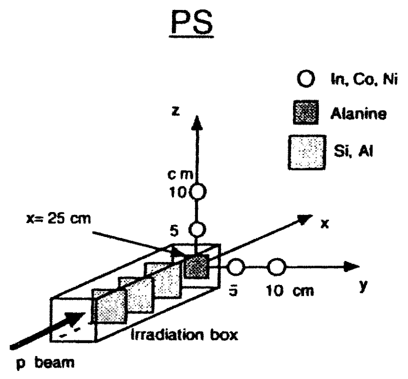

Figure 2: Set-up of the experiment at **PS**

The proton fluence-rate measured at **PS**, by Al foils was equivalent to (2.7 ± 0.15) × $10^9$ $p$ cm$^{-2}$ s$^{-1}$ and the proton dose-rate in silicon was (3.0 ± 0.16) kGy/h. The calculated value uses the concept of minimum ionizing energy loss [8].

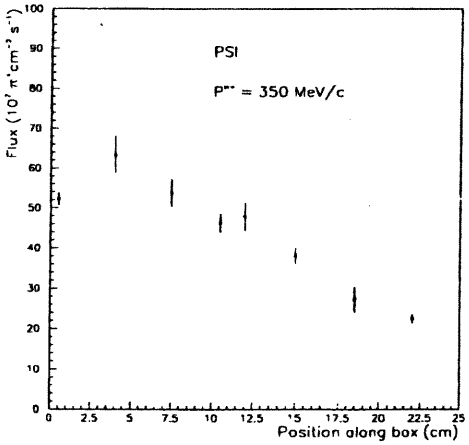

Figure 3: Pion fluxes at **PSI**

## *A. Neutron Flux Measurements*

The irradiations of the activation foils at both facilities were performed simultaneously with a group of Si samples. The irradiation time at **PSI** was 28920 s while at **PS** it was 7440 s.

After irradiation, the activation foils were removed and the induced activities were measured with a high purity Ge(p)-$\gamma$ spectrometer. The gamma spectra were analyzed by using the INTERGAMMA code [9] permitting the identification of a variety of created nuclei.

A total of four radionuclei coming from neutrons, were identified at **PSI**: two nuclei from In ($^{116}$In$^m$, $^{115}$In$^m$), one nucleus from Ni ($^{57}$Ni), and one nucleus from Co ($^{57}$Co). A total of seven radionuclei coming from neutrons, were identified at **PS**: two nuclei from In ($^{116}$In$^m$, $^{115}$In$^m$), three nuclei from Co ($^{57}$Co, $^{58}$Co, $^{56}$Mn), and two nuclei from Ni ($^{57}$Ni, $^{58}$Co).

The neutron fluxes were estimated by considering the cross sections associated to the most probable neutron energy at which the nuclear reaction can be produced. The estimated neutron fluxes are shown in Fig. 4 for **PSI**, and in Fig. 5 for **PS**. The cross sections were taken from [10].

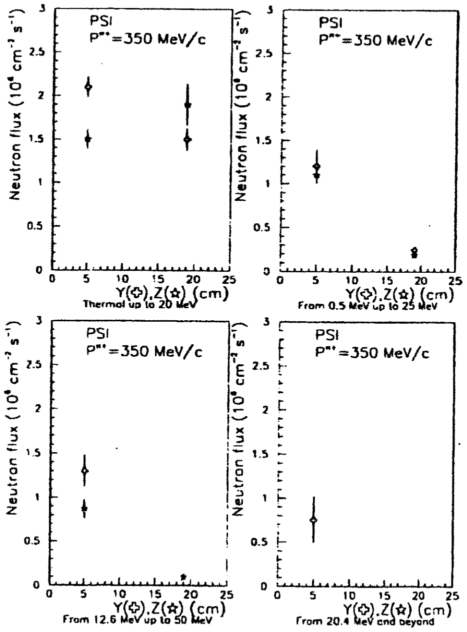

Figure 4: Estimated neutron fluxes near pion beam at **PSI**

1) *Results at* **PSI**:

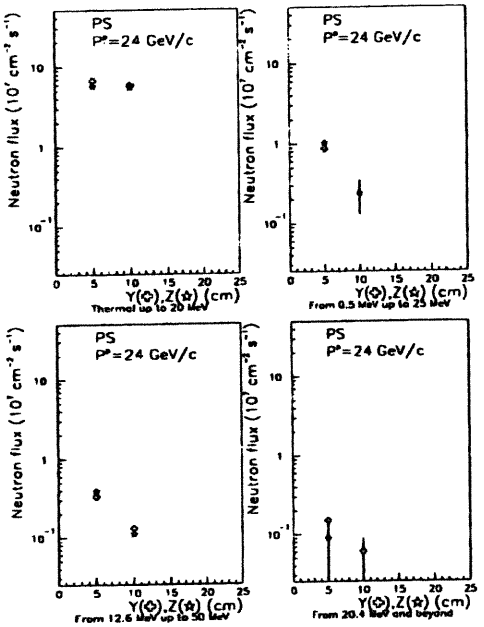

Figure 5: Estimated neutron fluxes near proton beam at **PS**

As shown in Fig. 4, the estimated neutron fluxes are decreasing with the distance from the pion beam axis and are generally decreasing with increasing threshold neutron energies. The low energy neutron component appears to be almost independent of the distance from the pion beam. The statistical fluctuations of these fluxes at the same distance from the beam are varying between 6% to 27% at 5cm and between 16% to 19% at 19 cm.

2) *Results at* **PS***:*

Fig. 5 shows the estimated neutron fluxes of four of the seven nuclear reactions found at **PS**. The low energy neutron component is almost independent of the distance from the proton beam and, in general, the estimated neutron fluxes are decreasing from a distance of 5 to 10 cm from the proton beam.

The statistical fluctuations of these fluxes at the same distance from the beam are varying between 11% and 35% (depending on the energy) at 5cm, and between 5% and 12% at 10 cm.

The errors associated to the estimated neutron fluxes at **PSI** and **PS** were calculated by taking into account the errors associated to the activities and weights of the foils. The error on the activity is the dominant error.

Fig. 6 and Fig. 7 show the estimated number of neutrons per incident pion at **PSI** and the estimated number of neutrons per incident proton at **PS** as a function of the neutron mean energy of the nuclear reaction. The number of neutrons created per incident hadron is observed to decrease exponentially with the neutron energy at 5 cm from the hadron beam. At 19 cm and 10 cm, the number of neutrons created per incident hadron is following the inverse of the neutron energy. The figure also shows that the main component of the neutron spectra is made of neutrons of low energy at both irradiation facilities.

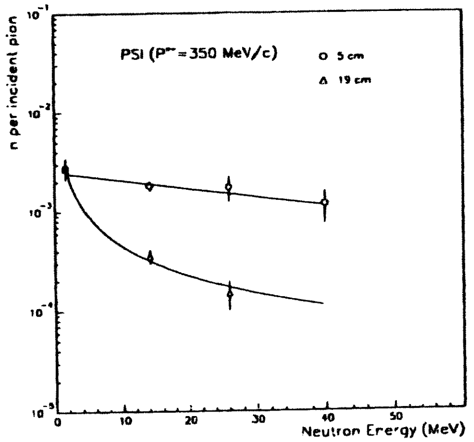

Figure 6: Estimated n per $\pi^+$ at **PSI**

## *B. Proton Flux Measurements*

A total of three radionuclei, coming from protons, were identified at **PSI**: one nucleus from Co ($^{52}$Mn), and two nuclei from Ni ($^{55}$Co, $^{52}$Mn), while at **PS** four radionuclei were identified: two nuclei from Co ($^{52}$Mn, $^{48}$V), and two nuclei from Ni ($^{55}$Co, $^{52}$Mn).

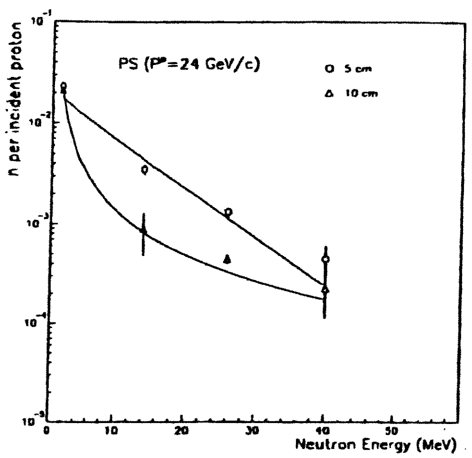

Figure 7: Estimated n per $p$ at PS

The proton fluxes were estimated by considering the cross sections associated to the most probable proton energy at which the nuclear reaction can be produced. The cross sections were taken from [7].

1) ***Results at*** **PSI***:*

No radionucleus was found at 19 cm from the pion beam. The results are obtained only from the radionuclei produced in the sample positionned at 5 cm from the beam. This is possibly due because protons have a smaller mean free path in air. At this distance from the pion beam, the estimated proton fluxes are decreasing with the proton threshold energy.

The ratios of the observed proton fluxes to the maximum pion flux given to the Si samples, at 5 cm are: (0.00861 ± 0.00325) proton per incident pion ($p/\pi_{inc}$) above 7.8 MeV up to 164.0 MeV, and (0.00158 ± 0.00089) $p/\pi_{inc}$ above 40.0 MeV up to 370.0 MeV.

2) ***Results at*** **PS***:*

The estimated proton fluxes at PS are decreasing with the proton threshold energy, but the more important proton component is above 70 MeV.

The ratios of the observed proton fluxes to the main proton flux given to the Si samples, at 5 cm are: (0.01080 ± 0.00023) proton per incident proton ($p/p_{inc}$) above 7.8 MeV up to 164.0 MeV, (0.00612 ± 0.00131) $p/p_{inc}$ above 40.0 MeV up to 370.0 MeV, and (0.01370 ± 0.00212) $p/p_{inc}$ above 70.0 MeV up to 370.0 MeV. As it was the case for the estimated neutron fluxes, the errors associated to the proton fluxes estimated at **PSI** and at **PS** were calculated by taking into account the errors associated to the activities and weights of the foils. The error on the activity is again the dominant error. The activation nuclear reactions used for these measurements are exclusively proton reactions.

## *C. Photon and Hadron Dose Measurements*

LiF dosimeters, read by a standard TLD reader, were giving the photon contamination at **PSI**. The average photon absorbed doses in LiF are: (5.0 ± 0.8) Gy/h at 10 cm, and (0.74 ± 0.03) Gy/h at 28 cm from the pion beam. It is observed that the photon dose fell by a factor 6 from the first to the second position.

The photon dose in Si were not determined, but by assuming that Si would replace LiF in the same field, the doses would not change very much. If the photons have a mean energy of less than 150 keV, the photon dose measured in LiF will be increased by a factor of (1.6 ± 0.4) for Si. Above 150 keV and up to 8 MeV, the dose in Si will be slightly decreased by a factor of (0.96 ± 0.04) compared with LiF. At energies above 8 MeV, this dose will be moderately increased by a factor (1.2 ± 0.05). These factors (1.6, 0.96, and 1.2) were calculated by taking into account the electromagnetic energy per unit of exposure (roentgen) absorbed by the Si material [11].

The alanine dosimeters were measured through Electron Spin Resonance technique, giving the pion and proton dose-rates in alanine. At **PSI**, the measured pion dose–rate is equivalent to (337.0 ± 7.2) Gy/h in alanine and the corresponding calculated value that uses the concept of minimum ionizing energy loss is equal to (262.0 ± 13.6) Gy/h. At **PS**, the measured proton dose–rate is (3.4 ± 0.08) kGy/h in alanine and the corresponding calculated value is equal to (3.2 ± 0.18) kGy/h.

The fact that the measured pion and proton dose-rates in alanine are larger that those calculated can be explained by the presence of other type of particles (neutrons, electrons and photons ) that contribute to the dose-rate.

# V. CONCLUSIONS

At **PSI**, the additional fluxes due to the contamination from neutrons and protons are a few percents of the main pion flux. The neutron contamination does not depend strongly on the energy at 5 cm from the pion beam and follows an exponential shape. At 19 cm, it is strongly dependent on energy following the inverse of the neutron energy ($1/E$) and the low energy component dominates. Proton contamination was found only at 5 cm from the pion beam and the fluxes are decreasing as a function of the proton energy. The average photon doses measured are (5.0 ± 0.8) Gy/h and (0.74 ± 0.03) Gy/h at 10 cm and 28 cm from the pion beam, respectively.

At **PS**, the contamination of neutrons and proton are also a few percents of the main proton flux. In this case, the neutron contamination at 5 cm from the proton beam is decreasing exponentially with neutron energy and, at 10 cm, the neutron spectra behave as $1/E^{1.5}$ (where $E$ is the neutron energy). The low energy component dominates. Proton contamination was found only at 5 cm from the proton beam and the dominant proton energy is above 70 MeV.

This first measurements of contamination around the irradiation beams gives a quantitative understanding with regards to the type and level of radiation damage of silicon detectors investigated simultaneously.

The radiation damage results for these Si samples can be found elsewhere [12].

# VI. REFERENCES

[1] Paul Scherrer Institute (PSI), *Users' Guide Accelerator Facilities*, 1994.

[2] A. Van Ginneken. Technical Report FN-522, Fermi National Accelerator Laboratory, 1989.

[3] E. León Florián, C. Leroy and C. Furetta. "Particle Fluence Measurements by Activation Technique for Radiation Damage Studies," CERN-ECP 95-15, August 1995.

[4] E. León Florián, H. Schönbacher and M. Tavlet. "Data Compilation of Dosimetry Methods and Radiation Sources for Material Testing," CERN/TIS/CFM/IR/93-03, March 1993.

[5] B.J. Dropesky, G.W. Butler, G.C. Giesler, C.J. Orth and R.A. Williams, "Excitation functions for the production of $^{18}$F and $^{24}$Na from Al and Si with fast pions," *Physical Review C*, Vol. 32, No 4, 1985.

[6] B.J. Dropesky, G.W. Butler, C.J. Orth, R.A. Williams and M.A. Yates-Williams, "Absolute cross sections for the $^{12}C(\pi^{\pm},\pi N)^{11}C$ reactions between 40 and 600 MeV," *Physical Review C*, Vol. 20, No 5, 1979.

[7] Landolt-Börstein ed.; Schopper H. editor, "Numerical Data and Functional Relationships in Science and Technology," Vol. 13 *Nuclear and Particle Physics, Production of Radionucleides at Intermediate Energies*, Springer-Verlag, Berlin ISBN-3-540-57540-5, 1994.

[8] A.H. Sullivan, *A Guide to Radiation and Radioactivity Levels near High Energy Particle Accelerators.* Nuclear Technology Publishing, ISBN 1 870965 18 3, 1992.

[9] "INTERGAMMA manual," software package, Version 5.10N, Intertechnique.

[10] V. McLane, C.L. Dunford, and P. Rose, *Neutron Cross Sections curves for Z=1-100.* Vol. 2 National Nuclear Data Center-Brookhaven National Laboratory, Academic Press, Inc., ISBN 0-12-484-220-8, 1988.

[11] M.H. Van de Voorde, "Effects of radiation on materials and components," CERN 69-12, 1969.

[12] S. Bates et al, "Proton irradiation of various resistivity silicon detectors", to be presented at RADECS 95.

## Acknowledgements

The authors are grateful to F. Lemeilleur and co-workers for giving us the opportunity to make these experiments. Our gratitude also goes to M. Tavlet and G. Roubaud from CERN-TIS Division, for providing the dosimeters and activation foils for these experiments.

The authors wish to thank R. Horisberger, K. Gabathuler, R. Frosch and A. Janett of the **PSI** for their help in providing the beam time, the beam diagnostic instrumentation, the gamma spectrometer and helping with the beam set-up.

The authors thank also the staff of the **PS** for their help and support in setting up the beam and providing smooth operation conditions.